**Title**

# Advancements in Microwave Optics for Measuring Polarization Anisotropies in the Cosmic Microwave Background

**Author**

Beckman, Shawn

**Publication Date**

2023

# Advancements in Microwave Optics for Measuring Polarization Anisotropies in the Cosmic Microwave Background

by

Shawn M. Beckman

A dissertation submitted in partial satisfaction of the

requirements for the degree of

Doctor of Philosophy

in

Physics

in the

Graduate Division

of the

University of California, Berkeley

Committee in charge:

Professor Adrian Lee, Chair
Professor William Holtzapfel
Professor Daniel Kasen

Fall 2023

# Advancements in Microwave Optics for Measuring Polarization Anisotropies in the Cosmic Microwave Background

# Abstract

Advancements in Microwave Optics for Measuring Polarization Anisotropies in the Cosmic Microwave Background

by

Shawn M. Beckman

Doctor of Philosophy in Physics

University of California, Berkeley

Professor Adrian Lee, Chair

The temperature and polarization anisotropies in the Cosmic Microwave Background (CMB) are direct probes into the physics of the early universe. Increasingly sensitive experiments aim to determine the tensor-to-scalar ratio r through measurement of an impossibly faint B-mode polarized signal shrouded by galactic foregrounds. A direct measurement of primordial B-mode polarization will be a measurement of the energy scale of inflation, unlocking an essential piece of the cosmological puzzle. Next-generation CMB experiments employ a large number of highly sensitive detectors in an attempt to find r and further constrain the cosmological parameters. Such a measurement requires not just high sensitivity to the CMB polarized signal, but large experimental bandwidth to characterize the polarized galactic dust and synchrotron radiation foreground signals.

For experiments using lenslet-coupled planar antenna detector array designs, reflection off the surface of the lenslet must be minimized over a given bandwidth to maximize the measured CMB signal. To this end, antireflection (AR) coatings for lenslets were developed for 30/40 GHz Simons Observatory low-frequency detectors, along with next-generation prototype coatings for 90/150 and 220/270 GHz arrays. The JAXA-led space-based mission LiteBIRD will utilize lenslet-coupled sinuous antenna arrays and TES bolometers for frequencies ranging from 40-195 GHz, necessitating broadband lenslet AR coatings that are robust to launch vibrations and differential thermal contraction. To meet these requirements, a metamaterial AR surface has been proposed. A metamaterial coating designed for the LiteBIRD LF-3 band has been laser etched onto a flat surface, achieving 98% in-band transmission. A six-axis positioning system is used to etch the metamaterial pattern onto a sphere, and a completed prototype LF-3 lenslet is expected to be etched in late 2023. Details of the metamaterial design and the etch process are discussed. Cosmic rays at the Lagrange point L2 pose a threat to LiteBIRD's sensitivity, as they produce a white noise component that cannot be fully deconstructed in analysis. To mitigate this cosmic ray white noise component, on-chip mitigations have been developed for the purpose of minimizing thermal diffusion from the silicon detector wafer to the TES bolometer detectors. Lastly, the mechanical design and fabrication of a continuously rotating warm half-wave plate for the POLARBEAR-2a experiment, used to minimize noise in large-angular-scale measurements from atmospheric fluctuations, are discussed.

# Contents

# List of Figures

# Acknowledgments

This dissertation would not be possible without a great deal of help from many people over the years I have spent at Berkeley, and a lot of support from family and friends since I decided to study physics back in 2010.

First, I would like to thank my advisor Adrian Lee. Adrian took me on as a graduate student the summer before classes began my first year at Berkeley. With such a wide variety of projects for several field-leading experiments, I was spoiled for choice as a researcher from the first year I was working in his lab. He served as an example of the efficiency needed to work on multiple research projects simultaneously, which certainly expanded my research capacity. Adrian has created a diverse research group at Berkeley, which has made substantial progress in CMB instrumentation, due to the academic freedom he gives and the confidence he has in his researchers.

The people with whom I have been able to work and spend time with throughout my graduate career have enriched both my experience and the quality of my research. The ability to bounce ideas off the talented people around me while having fun doing it defined my grad school experience. Thanks in particular to Ben Westbrook, Charlie Hill, Ari Cukierman, Darcy Baron, Neil Goeckner-Wald, Oliver Jeong, Kevin Crowly, Nick Huang, Jessica Avva, and all of the other graduate students and postdocs that I have had the pleasure of working with for not only being valuable knowledge resources, but good friends as well. There have been many people over the years that fall into this category, including fellow grad students and staff outside of the group. I apologize if I have missed any names, but you know who you are.

A large majority of my research during graduate school would not have been possible without the exceptional talent and expert advice from the machinists in the UC Berkeley Physics machine shop. Their abilities give me the confidence to design parts more freely and creatively, never ceasing to amaze me when I see them come to life in the shop. I am convinced that I will never meet a more talented machinist than Gordon Long - whether it be machining a plastic mold to within five microns of spec, creating a small nozzle with extremely intricate features on a five-axis CNC, or micro-drilling 50 micron holes through invar, I know that whatever idea I can come up with, he will be up for the challenge. Gordon has taught me a great deal over the years and I very much appreciate my time spent working and chatting with him in the shop. Even when Gordon is not the machinist working on my project, I can be confident that the other machinists will accomplish whatever crazy features or tolerances I throw at them. In addition to often helping me through my design process and consistently returning quality parts, Tommy Gutierrez has become a role model and friend. I always look forward to a ten minute break from work to talk to Tommy about projects, life, and anything else. There isn't a single project of mine that hasn't benefited from work or input from these machinists, and for that I owe them a large part of this PhD.

I think I certainly surprised my family when I announced that I was going to pursue a career as a physicist, having previously had a clearly defined career path as a photographer/videographer. Since then, they have been nothing but supportive and excited to see where this path takes me. Thanks to my mom for never doubting me and giving me support and love when I needed it, and to my dad for always keeping his confidence in me. My sister Grace has been my best friend and pillar of support throughout undergrad and grad school. So much has changed in our lives in the last 12 years, but Grace has always been there for me to laugh with and be a shoulder to lean on. My shared experiences with my sister Krista have led us down two very different career paths, but her motivation, hard work, and success has been a model for me to follow my goals in science that led to this PhD. My cousin Maggie gave me a home when I moved to Oregon at seventeen. When I told her I was going to study physics and get a PhD when I was eighteen, she bought me a Fisher space pen with "Shawn Beckman PhD" engraved on it. She was there with me from the very beginning of my physics career and gave me the confidence to pursue it. Watching Maggie run a successful business as a talented photographer showed me that I could do whatever I wanted to do with my life if I was smart about it and put in the effort. She continues to be a role model for me and I can't wait to make her call me Dr. Shawn for the rest of our lives.

I also owe thanks to all of the friends I have made throughout my physics career. From overnighters in Gamow tower to daily prelim study groups, many PhDs have been earned, research done, and careers made during our friendships. The path there would not have felt as sure or as fun without you.

# Chapter 1

# Science Motivation

Perhaps the most compelling subject of research in Astrophysics and Cosmology that one can study is the origin of the universe. Starting with Edwin Hubble's discovery of an expanding universe in the 1920s [1], evidence gathered throughout the 20th and 21st centuries points to a big bang event, during which the universe rapidly expanded in a short period of time, cooling and expanding into the universe we see today. The fingerprint left behind by this rapid expansion is the cosmic microwave background (CMB), and it is studied to constrain various cosmological parameters, painting a picture of the very early universe. This chapter introduces big bang cosmology and overviews how measurements of the CMB can be used to constrain cosmological parameters, along with some of the inherent challenges in making these measurements.

## 1.1 Big bang cosmology

In 1922, Alexander Friedmann presented a solution to Einstein's field equations that described an expanding universe [2]. The field equations are used to define the distribution of mass and energy in the universe with respect to the geometry of spacetime, where the Einstein tensor is

$$G_{\mu\nu} = R_{\mu\nu} - \frac{1}{2}Rg_{\mu\nu} = 8\pi G T_{\mu\nu} - \Lambda g_{\mu\nu} \tag{1.1}$$

describing the curvature of the universe in terms of the gravitational constant G, the stress-energy tensor $T_{\mu\nu}$, the metric tensor $g_{\mu\nu}$, and a cosmological constant $\Lambda$. $G_{\mu\nu}$ is defined using the Ricci curvature tensor $R_{\mu\nu}$, the Ricci scalar R and the metric tensor. The term $\Lambda g_{\mu\nu}$ was originally introduced by Einstein in order to allow for the solution of a static universe, but was removed after Hubble presented observational data for an expanding universe in 1929. Modern cosmology, however, reintroduces this term to express the energy density of space that results in the accelerated expansion of the universe.

Hubble's discovery of an expanding universe supported the idea of homogeneity and isotropy on large scales in the universe. To better describe the observed expansion, the Robertson–Walker (RW) metric was developed as a solution to Einstein's field equations, describing the geometry of a homogeneous and isotropic universe. Using the convention c = 1, the metric is defined as

$$ds^2 = dt^2 + R^2(t)[d\chi^2 + S_k^2(\chi)d\Omega^2], \tag{1.2}$$

where the geometry is a function of time t and the radial coordinate of a hypersphere $\chi$ with solid angle $\Omega$. R(t) represents a scale factor, often defined as $a(t) = R(t)/R(t_0)$, where the '0' subscript conventionally denotes the present time. With discrete values of k = (+1, 0, -1) and $S_k^2(r) = (sin(\chi), \chi, sinh(\chi))$, respectively, the RW metric describes spatially closed, open, or flat geometries.

In this metric, Einstein's field equations become

$$\begin{aligned} H^2 \equiv \left(\frac{\dot{a}}{a}\right)^2 &= \frac{8\pi G\rho}{3} - \frac{k}{a^2} + \frac{\Lambda}{3} \\ \frac{\ddot{a}}{a} &= \frac{\Lambda}{3} - \frac{4\pi G}{3}(\rho + 3p). \end{aligned} \tag{1.3}$$

These are known as the Friedmann equations. Here, $H(t)$ is the Hubble parameter, $\rho$ is the energy density, and p is the isotropic pressure. Note that in the case of $\Lambda = 0$, an expanding or contracting universe is implied. The Friedmann equations describe the ultimate fate of an expanding universe, whether it continues to expand indefinitely (k = 0, -1), or collapses on itself (k = +1). A useful way to think about the energy density is to compare it with the energy density at present day assuming a flat universe with $\Lambda = 0$. This parameter is defined as the critical energy density

$$\rho(t = 0, k = 0, \Lambda = 0) = \rho_c \equiv \frac{3}{8\pi G} H_0^2, \tag{1.4}$$

where the energy density relative to the critical energy density is defined as the cosmological density parameter

$$\Omega_{tot} \equiv \frac{\rho}{\rho_c}. \tag{1.5}$$

At present day, the first Friedmann equation can be rewritten as

$$\Omega_{tot} = 1 + \frac{k}{H_0^2}. \tag{1.6}$$

where $\Omega > 1$ corresponds to a closed universe, $\Omega = 0$ corresponds to a flat universe, and

$\Omega < 1$ corresponds to an open universe.

Current experimental data and theory informed the development of the standard cosmological model known as ΛCDM cosmology. This model describes a universe composed of dark energy that causes accelerated expansion of the universe (Λ), cold dark matter (CDM), and ordinary matter consisting of standard model particles. Using ΛCDM, the total energy density can be separated into contributions from radiation, matter, curvature, and dark energy. An equation of state can be defined as $w \equiv p/\rho$, comparing the pressure relative to the energy density for a given contribution. With this definition, w = (1/3, 0, -1/3, -1) for ultra-relativistic radiation, non-relativistic matter (including CDM), curvature, and dark energy, respectively. Plugging these into the Friedmann equations, the Hubble parameter can be written in terms of relevant density parameters as

$$H^2 = H_0^2 \left( \frac{\Omega_r}{a^4} + \frac{\Omega_m}{a^3} + \frac{\Omega_k}{a^2} + \Omega_\Lambda \right). \tag{1.7}$$

At present day where a = 1, Equation 1.7 becomes

$$\Omega_r + \Omega_m + \Omega_k + \Omega_\Lambda = 1. \tag{1.8}$$

## 1.2 Inflation

Inflation describes a period of rapid expansion in the early universe, expanding by a factor of $10^{26}$ between $10^{-35}$ and $10^{-32}$ seconds from its outset and decreasing in temperature from $10^{27}$ K to $10^{22}$ K. Although the ΛCDM cosmological model is supported by a considerable amount of experimental evidence, it fails to explain a number of observations, which are detailed below. An inflationary model can be used to remedy these discrepancies, painting a more complete picture of our universe.

### The flatness problem

Current measurements indicate that we live in a very flat universe, where $\Omega_k = 0.001 \pm 0.002$ [3]. Equation 1.7 shows that any small deviation from an initial flatness will scale as the universe evolves in time. A particularly strict initial flatness condition is a potential explanation for this; however, a more likely explanation is that curvature was allowed in the early universe during the inflationary epoch. Any small curvature during inflation would eventually be undetectable due to the immense expansion of space following.

### The horizon problem

From ∼10 s after the beginning of the universe, photons Thomson scatter throughout a primordial plasma [4] until the universe had expanded and cooled enough for the photons to decouple from the primordial plasma at a redshift of $z \simeq 1100$ [5], at which point they were allowed to free-stream, creating the CMB. This event is commonly referred to as recombination. Redshift is used to quantify the shift in a photon's wavelength due to either the relative motion of radiating sources, or in this case, a distance in which a photon's wavelength has shifted over caused the expansion of space time, where

$$a(t) = \frac{1}{1+z} = \frac{\lambda_{emit}}{\lambda_{obs}}. \tag{1.9}$$

A redshift of z = 1100 corresponds to $\sim 380,000$ years after the big bang, meaning that two photons in causal contact at the start of the big bang could have traveled a comoving distance of 380,000 light years. The horizon problem stems from the fact that the temperature of the CMB is extremely uniform across the sky, meaning that photons that theoretically could not have been in causal contact between the big bang and the calculated time of recombination were somehow able to reach thermal equilibrium. Figure 1.1 shows a depiction of an observer's light cone relative to the light cones of two CMB photons a distance of 380,000 light years away at z = 1100.

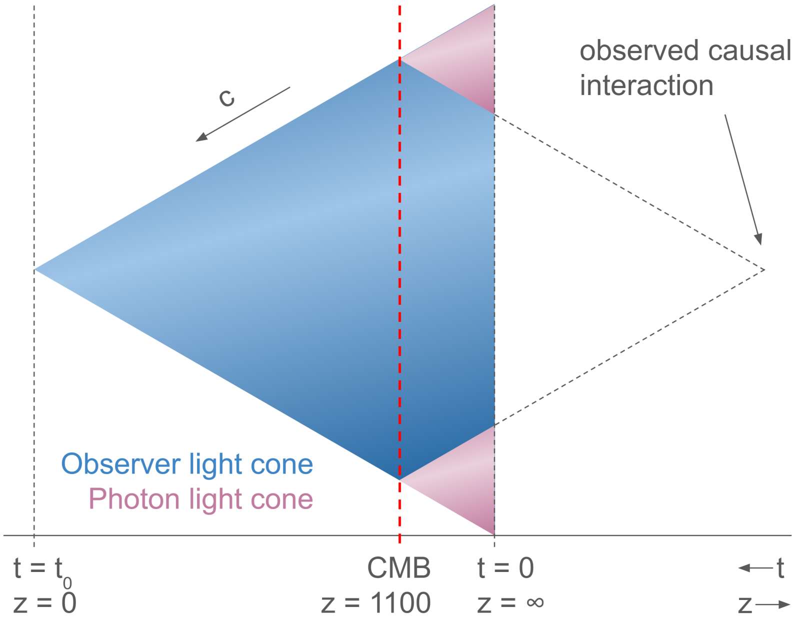

Figure 1.1: Depiction of past light cones for a present day observer and CMB photons, showing the photons could only be in causal contact before the big bang.

One explanation for this could be that the speed of light in the early universe was faster before recombination, and therefore the photons were able to travel further than where we would observe their causal contact to have happened today. Inflation, however, provides a more tenable explanation in which a rapid expansion of space, faster than the speed of light, occurred to bring the two points into causal contact at some point after the big bang.

### The magnetic monopole problem

The standard model of particle physics predicts the existence of magnetic monopoles, yet no monopoles have been found. ΛCDM cosmology doesn't explain the existence of magnetic monopoles, but inflationary theory provides a high enough energy density to generate a finite number of them. As the universe expands and becomes more flat, the number of monopoles would become diluted, providing an explanation for the lack of observational evidence.

### Seeding of density perturbations

Large scale structure observed in the CMB can be attributed to density perturbations in the early universe using ΛCDM cosmology; however, it does not describe the origin of the density perturbations. Inflationary theory predicts that quantum fluctuations in energy density seed the density perturbations used to describe the origin of large-scale structure.

## 1.2.1 Slow roll inflation

To modify the RW metric to accommodate inflation, a scalar field $\phi$ with a field-dependant potential $V(\phi)$ can be introduced, modifying the energy-momentum tensor $T_{\mu\nu}$ (assuming the matter content of the universe is a perfect fluid), as

$$\begin{aligned} T_{\mu\nu} &= -pg_{\mu\nu} + (p+\rho)u_\mu u_\nu \\ \rightarrow T_{\mu\nu} &= \delta_\mu\phi\delta_\nu\phi - \frac{1}{2}g_{\mu\nu}\delta_\rho\phi\delta^\rho\phi - g_{\mu\nu}V(\phi), \end{aligned} \tag{1.10}$$

corresponding to a fluid with energy density and pressure

$$\begin{aligned} \rho &= \frac{1}{2}\dot{\phi}^2 + V(\phi) \\ p &= \frac{1}{2}\dot{\phi}^2 - V(\phi), \end{aligned} \tag{1.11}$$

in a homogeneous background. This modifies the first Friedmann equation to be

$$H^2 = \frac{8\pi G}{3}\left(\frac{1}{2}\dot{\phi}^2 + V\right) - \frac{k}{a^2}. \tag{1.12}$$

Assuming energy conservation in the scalar field, $T_{\mu\nu} = 0$, the Friedmann equations can be reduced to define the Klein-Gordon equation of motion

$$\ddot{\phi} = -3H\dot{\phi} - \frac{dV}{d\phi}, \tag{1.13}$$

where $3H\dot{\phi}$ is a damping term, slowing the evolution of the field, and $dV/d\phi = V'$ describes the evolution of the field potential. The slow-roll approximation of this equation of motion assumes a negligible $\ddot{\phi}$, where $dV/d\phi \sim -3H\dot{\phi}$, where the gradient in the field's potential is balanced by the damping of the field. This approximation requires that certain defined slow-roll parameters be sufficiently small, where

$$\begin{aligned} \epsilon &\equiv \frac{M_{pl}^2}{16\pi}\left(\frac{V'(\phi)}{V(\phi)}\right)^2 \ll 1 \\ \eta &\equiv \frac{M_{pl}^2}{8\pi}\left|\frac{V''(\phi)}{V(\phi)}\right| \ll 1. \end{aligned} \tag{1.14}$$

Here, $M_{pl}$ is the Planck mass given by $M_{pl}^2 = G$. This requirement results in a flat scalar field potential that remains constant throughout inflation. The total logarithmic expansion during inflation can be quantified by looking at the number of e-folds $N_e$ that occur in the scale factor from the beginning to the end of inflation, where

$$\begin{aligned} N_e &\equiv \ln\left(\frac{a_{end}}{a_{start}}\right) \\ &= \int_{t_{start}}^{t_{end}} H dt \\ &\approx \int_{t_{start}}^{t_{end}} \frac{1}{M_{pl}}\sqrt{\frac{4\pi}{\epsilon}} d\phi \quad \text{for} \quad \frac{dV}{d\phi} > 0 \\ &\approx \sqrt{\frac{4\pi}{\epsilon}}\frac{\Delta\phi}{M_{pl}} \quad \text{for} \quad \epsilon = Const. \end{aligned} \tag{1.15}$$

In this approximation, with a sufficiently large N, a large enough change in the field explains the causal contact issue in the horizon problem and describes the evolution of a curved universe into a flat universe. In addition, given that the energy scale of inflation approaches the Planck scale, quantum fluctuations can couple with the scalar field, explaining the seeding of large-scale structure. As the scalar field evolves, its potential energy will 'slowly roll' down into a local minimum, and the field's energy density will begin to convert into kinetic energy, creating the various energy density components we see in the universe today. This process is known as reheating.

### 1.2.2 Perturbations to the metric

In order to quantify observed inhomogeneities in the universe, a perturbation term can be introduced in the metric tensor, as

$$g'_{\mu\nu} = g_{\mu\nu} + h_{\mu\nu}, \tag{1.16}$$

where $h_{\mu\nu}$ can be decomposed into a sum of scalar, vector, and tensor components.

### Vector perturbations

Vector perturbations arise from the vortical motions of matter ($\nabla \times \vec{v} \neq 0, \nabla \cdot \vec{v} = 0$). Because there is no associated energy density with vector modes, as they are not enhanced by gravity, they decay away with cosmic expansion.

### Scalar perturbations

Scalar perturbations modes arise from gravitational instability and represent energy density perturbations in the cosmological fluid at recombination.

### Tensor perturbations

Tensor perturbations of the metric are transverse traceless components that represent the quadrupolar stretching of space in the plane of the perturbation. Perturbations that apply quadrupolar stretching to the metric are referred to as gravitational waves.

Assuming Gaussian distributions of scalar and tensor perturbations, it is useful to look at their power spectra $P_\zeta$ for the scalar spectrum and $P_t$ for the tensor spectrum. A given power spectrum has a two-point correlation function defined by co-moving wavevectors $\vec{k}$ and $\vec{k}'$, and can be written as

$$\left\langle \delta(\vec{k})\delta(\vec{k}') \right\rangle \sim \frac{\delta^3(\vec{k}+\vec{k}')}{k^3} P(k), \tag{1.17}$$

Because the potential energy in the inflationary field decreases as the field evolves, the magnitude of k increases, eventually crossing the Hubble length threshold at a given time denoted by '$*$', where $k = a_* H_*$. This is when the modes become frozen in, resulting in different modes exiting their horizon at different times. The power spectra are then given by

$$\begin{aligned} P_\zeta(k) &= A_s \left(\frac{k}{k_*}\right)^{n_s - 1} \sim \frac{H_*^2}{\epsilon_* M_{pl}^2} \\ P_t(k) &= A_t \left(\frac{k}{k_*}\right)^{n_t} \sim \left(\frac{H_*}{M_{pl}}\right)^2, \end{aligned} \tag{1.18}$$

where $n_s$ is the scalar index, which describes the spectral tilt in the scalar spectrum, and the tensor index $n_t$ describes the tilt in the tensor spectrum, where

$$\begin{aligned} n_s &= 1 + \frac{d\,\log P_\zeta}{d\log k} \\ n_t &= \frac{d\,\log P_t}{d\log k}. \end{aligned} \tag{1.19}$$

Using the scalar and tensor power spectra gives us a quantity known as the tensor-to-scalar ratio, r, where

$$r_* \equiv \frac{P_t(k_*)}{P_\zeta(k_*)} \simeq 16\epsilon_* \propto V_*. \tag{1.20}$$

The tensor-to-scalar ratio is a powerful parameter, where for a given $k_*$, the relative amplitudes of the measured tensor and scalar modes will provide the energy scale of inflation. Figure 1.2 shows the measured constraints on the value of r given $k_* = 0.002\ Mpc^{-1}$ for a given $n_s$.

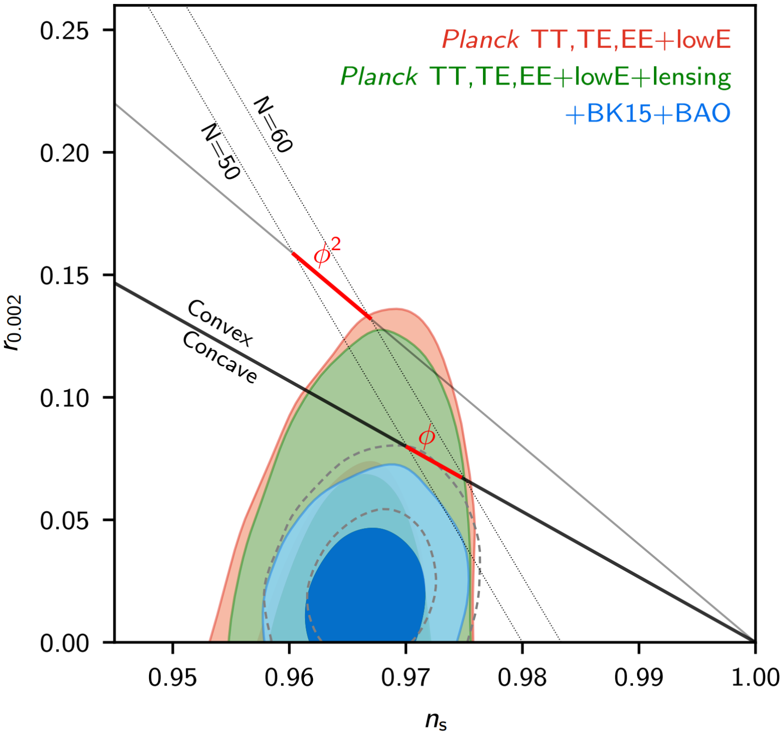

Figure 1.2: Current measured constraints on $r_{0.002}$ as a function of $n_s$ taken from the Planck 2018 release [3].

## 1.3 Cosmic microwave background

Briefly introduced in the previous section, the CMB is perhaps the most powerful tool used to constrain cosmological parameters and better understand the universe. From ∼10 s - 380,000 years after the big bang, photons Thomson scatter within a photon-baryon fluid. After 380,000 years, the universe has begun to cool enough for particles in the photon-baryon fluid to begin to form atoms, allowing the trapped, scattering photons to free-stream. This recombination event is measured at what is referred to as the surface of last scattering at z $\simeq$1100. The light that free-streamed from the surface of last scattering retains the fingerprint of primordial perturbations, seeding large-scale structure and imprinting a polarization that can be measured to estimate the amplitudes of tensor and scalar inflationary fields.

CMB light was first measured by Penzias and Wilson in 1965 as an excess temperature of 3.5 K using a 20-foot horn-reflector antenna [6]. Today, the temperature of the CMB is measured as a blackbody spectrum to be 2.72548 ±0.00057 K [7]. Measurements of temperature anisotropies in the CMB spectrum ($\sim 10^{-5}$ level) were first seen by the Cosmic Background Explorer (COBE) satellite in 1992 [8]. Since the COBE experiment, measurements have been continually improved by both ground-based telescopes and satellite experiments, resulting in observation evidence that strongly agrees with $\Lambda$ CDM cosmology. With CMB temperature anisotropies having been measured to such high precision, CMB experiments have begun to focus on polarization anisotropy measurements ($\sim 10^{-6}$ level) to provide better constraints on cosmological parameters.

This section overviews CMB temperature and polarization anisotropies and how they are used to probe the early universe.

### 1.3.1 Temperature anisotropies

Measurements from the Planck satellite currently provide the most detailed full-sky map of anisotropies, shown in Figure 1.3 from the Planck 2015 release [9].

Decomposing CMB temperature measurements into spherical harmonics $Y_{\ell m}(\hat{n})$ provides a useful way to interpret the data, where $\hat{n}$ defines the sky position in terms of $\ell$ and $m$

$$\Delta T(\hat{n}) = \sum_{\ell=0}^{\infty} \sum_{m=-\ell}^{\ell} a_{\ell m} Y_{\ell m}(\hat{n}). \tag{1.21}$$

Here, the amplitudes of each mode are given by $a_{\ell m}$. Because these anisotropies are isotropic over the whole sky and because they are largely Gaussian, a two-point correlation function with the power spectrum $C_\ell$ can be defined as

$$\langle \Delta T(\hat{n}), \Delta T(\hat{n}') \rangle = \frac{1}{4\pi} \sum_{\ell=0}^{\infty} (2\ell+1) C_\ell P_\ell(\hat{n} \cdot \hat{n}'), \tag{1.22}$$

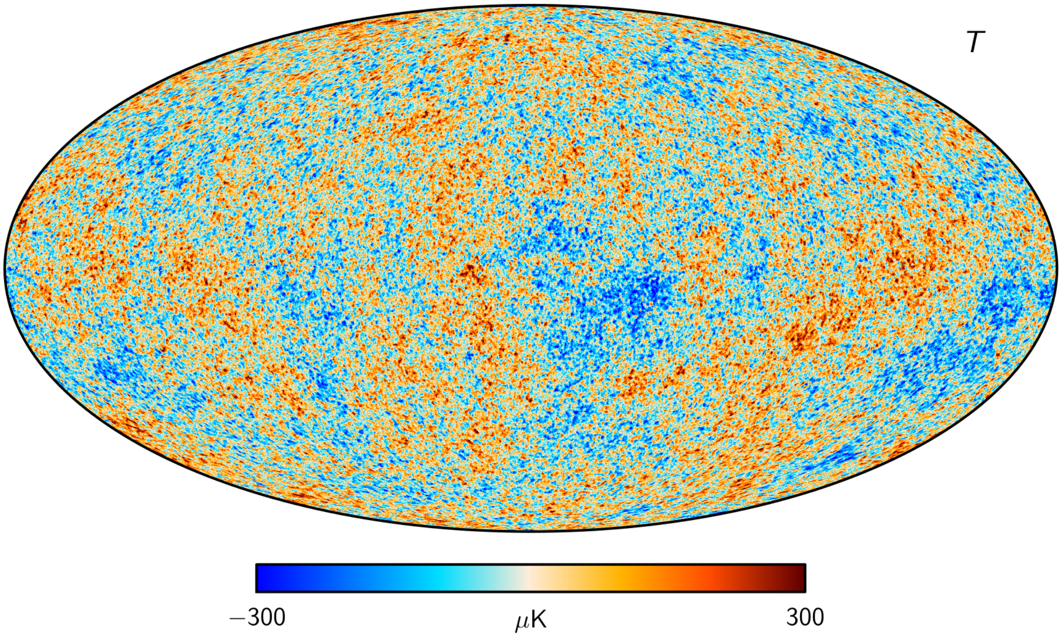

Figure 1.3: Full sky CMB temperature map taken from Planck using an equal-area map projection, taken from the Planck 2015 release [9].

with Legendre polynomials $P_\ell(cos(\theta))$. $C_\ell$ can be written in terms of the mode variances as

$$\langle a_{\ell m}, a^*_{\ell' m'} \rangle = \delta_{\ell m} \delta_{\ell' m'} C_\ell. \tag{1.23}$$

The sample variance of each $C_\ell$ is given by both the fraction of the sky that is measured and the fact that for each $\ell$ mode, there are $(2\ell + 1)$ m modes. This is known as the cosmic variance limit, where

$$\Delta C_{ell} = \sqrt{\frac{2}{(2\ell + 1) f_{sky}}} C_\ell. \tag{1.24}$$

Given that at large angular scales corresponding to low $\ell$s, are prone to becoming cosmic variance limited, a larger measured sky fraction $f_{sky}$ will provide more precise measurements of $C_\ell$ in these regimes, motivating space-based missions to probe large angular scales.

### 1.3.2 Polarization anisotropies

In the photon-baryon plasma, quadrupole variations in temperature, caused by scalar and tensor perturbations to the inflationary field, create linear polarization components in Thomson scattered light (shown in Figure 1.4. At the surface of last scattering, these polarizations are locked into CMB light and can be measured. These polarization components are decomposed into what is known as E-mode and B-mode radiation [10], caused by scalar and tensor quadrupolar variations, respectively. In order to better understand E and B-mode decomposition, it is useful to first define what are known as the Stokes parameters, where

$$\begin{aligned} Q &\equiv \left\langle |E_x|^2 \right\rangle - \left\langle |E_y|^2 \right\rangle \\ U &\equiv \left\langle |E_a|^2 \right\rangle - \left\langle |E_b|^2 \right\rangle \\ V &\equiv \left\langle |E_r|^2 \right\rangle - \left\langle |E_l|^2 \right\rangle \\ I &\equiv \left\langle |E_{x,a,r}|^2 \right\rangle + \left\langle |E_{y,b,l}|^2 \right\rangle . \end{aligned} \tag{1.25}$$

These parameters are represented by statistical averages of the intensities of linear or circular polarizations, where $E_x$, $E_y$ are linear polarizations orthogonal to one another, $E_a$, $E_b$ are also orthogonal linear polarizations, rotated 45 degrees from $E_x$ and $E_y$, and $E_r$ and $E_l$ represent circular polarizations, where $\hat{r} = (\hat{x} - i\hat{y})/\sqrt{2}$ and $\hat{l} = (\hat{x} + i\hat{y})/\sqrt{2}$.

E and B-modes can be defined in terms of the Stokes parameters as

$$\begin{aligned} E(\vec{\ell}) &= Q(\vec{\ell})cos(2\phi_{\vec{\ell}}) + U(\vec{\ell})sin(2\phi_{\vec{\ell}}) \\ B(\vec{\ell}) &= U(\vec{\ell})cos(2\phi_{\vec{\ell}}) - Q(\vec{\ell})sin(2\phi_{\vec{\ell}}), \end{aligned} \tag{1.26}$$

where $\vec{\ell}$ is a two-dimensional vector at angle $\phi_{\vec{\ell}}$ in a flat-sky approximated Fourier-space. A graphic representation of these polarizations is shown in Figure 1.4.

An observation of this E and B-mode linear polarization decomposition is that E-modes are ‘curl free’ and parity even, while B-modes are ‘divergence free’ and parity odd. It is important to note that E-mode polarization can result only from density fluctuations given by scalar modes of cosmological perturbations. However, B-mode polarization can result from both density fluctuations and gravitational waves caused by the tensor perturbation modes [11]. Because of this, a measurement of B-modes can be used to probe gravitational waves during inflation, a necessary consequence of the inflationary model. Unfortunately for experimental cosmologists, primordial gravitational waves are not the only source of B-mode polarization. E-modes can be gravitationally lensed through large-scale structure to transform into B-modes, requiring ‘delensing’ in analysis. In addition, galactic dust and synchrotron radiation are polarized foregrounds that contaminate measurements of the primordial signal and need to be removed in analysis. These are known as foregrounds and are discussed in further detail in Section 1.4.

### 1.3.3 CMB angular power spectra

Anisotropies appearing at the multipole moment $\ell$ can be quantified using an angular power spectrum $C_\ell$. For intuition, $\ell \sim 180°/\theta$, where in a power spectrum, anisotropies appearing at a multipole moment of $\ell = 10$ are seen at $\sim 18°$. Typically, CMB power spectra are plotted

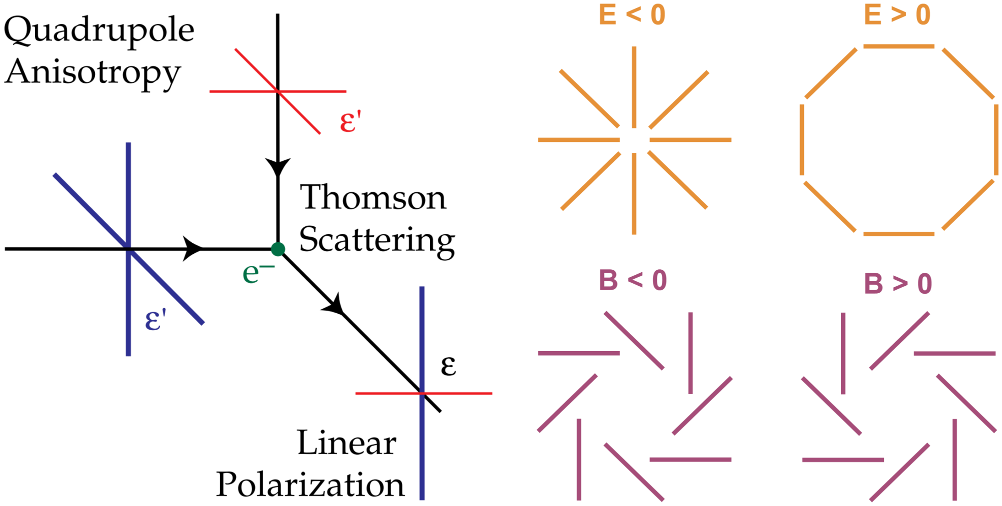

Figure 1.4: (Left) A graphic taken from Wayne Hu and Martin White's polarization primer [10] showing how incident radiation with a quadrupolar anisotropy (blue is hotter, red is colder) can Thomson scatter into linear polarization. (Right) Graphic representations of E and B modes, showing their even and odd parities respectively.

as auto-correlations or cross-correlations in temperature, E-modes, or B-modes, represented by a superscript (TT, EE, BB, TE, TB, or EB). For example, a cross-correlated TE power spectrum will often be plotted as

$$D_\ell^{TE} = \frac{\ell(\ell+1)}{2\pi} C_\ell, \tag{1.27}$$

where the factor of $\ell(\ell+1)/2\pi$ is added by convention.

Figure 1.5 shows the $D_\ell^{TT}$ power spectrum using Planck data taken from [3]. The various features seen in a CMB temperature power spectrum contain information about the early universe.

The horizon scale at the surface of last scattering corresponds to an $\ell \sim 100$. Modes beneath the horizon scale have not evolved since the surface of last scattering, and consequently are a probe into the initial conditions, parameterizing inflation. In the temperature power spectrum, the lower $\ell$ mode anisotropies are dominated by gravitational redshifting, known as the Sachs-Wolfe effect [13]. The flat feature that results is known as the Sachs-Wolfe plateau.

Peaks between $\ell \sim 100$ and $\ell \sim 1000$ are known as the acoustic peaks. These are the result of causal interaction inside the horizon, where the structure of gravity-driven acoustic oscillations known as baryon acoustic oscillations (BAO) has been imprinted in the CMB light at the surface of last scattering [14].

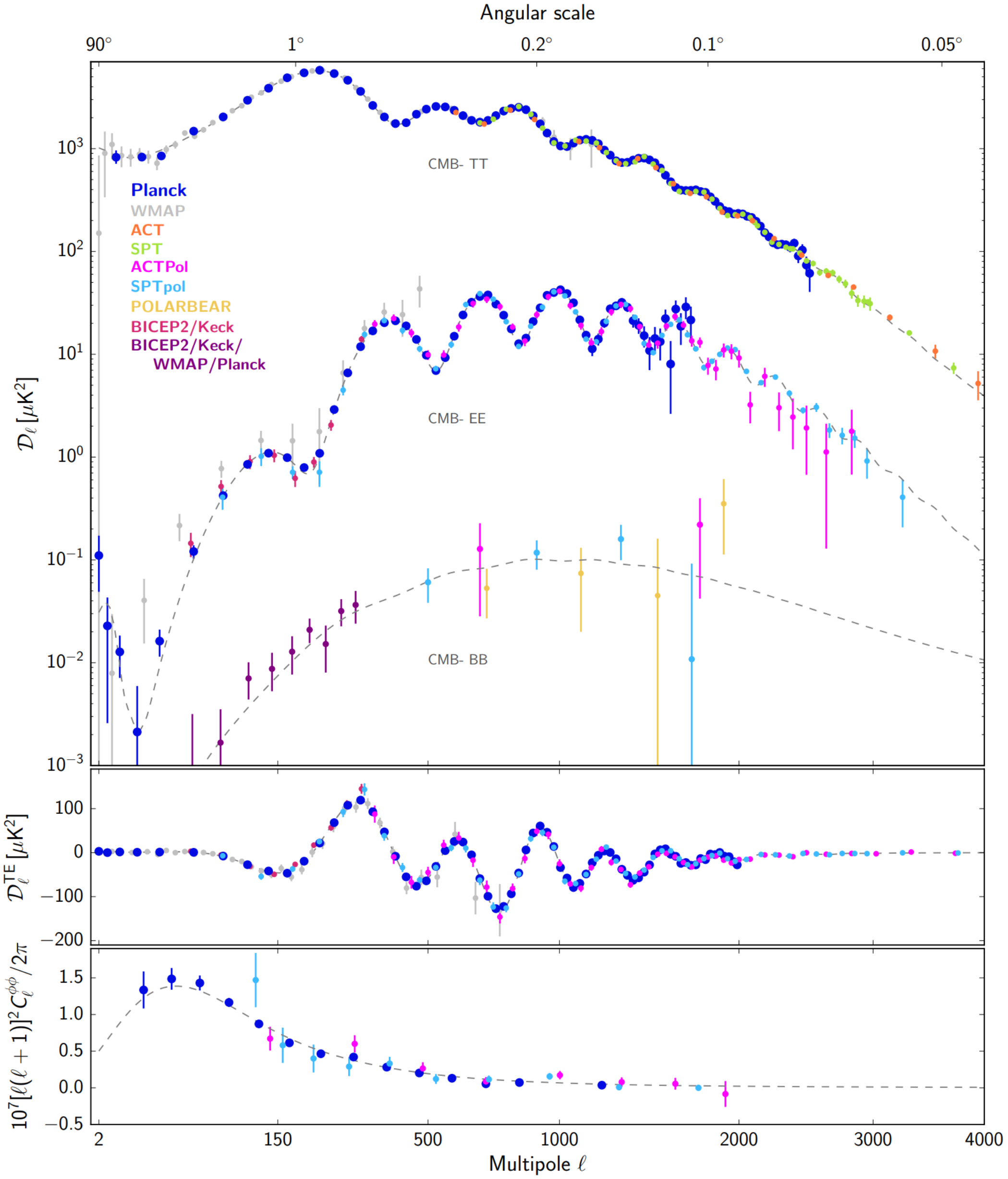

Figure 1.5: Compiled measurements showing the CMB TT, EE, and BB power spectra from Planck 2018 [12] with a fit corresponding to the ΛCDM model. [3]

Above $\ell$ ∼1000 the effect of a non-zero thickness to the surface of last scattering is seen, and the BAO peaks are damped away. This happens because as atoms begin to form, the mean free path of a photon increases. When the mean free path is larger than the scale of an oscillation (happening at higher $\ell$), the effect of the oscillation is ‘damped’ away. This effect is known as Silk damping [15].

BAO and the effects of the damping tail can be seen as a much fainter signal in measurements of the CMB E-mode polarization anisotropies, $D_\ell^{TE}$, as the oscillations create quadrupolar anisotropies that can scatter polarized light. At angular scales less than $\ell$ ~100, the EE power spectrum is relatively flat, with a slope of $\ell(\ell + 1)$. This is because there is no Sachs-Wolfe analogue for polarization, since the polarization of light is not affected by gravitational redshift. At very large angular scales around $\ell < 10$, both the EE and BB signals will be dominated by the reionization peak as a result of scattering during the period of star formation known as reionization.

Regarding the B-mode spectrum, Figure1.6, shows the BB spectrum separated into primordial B-mode and lensing B-mode components for various hypothetical values of r. The peak around $\ell = 1000$ (shown more clearly in Figure 1.5) is dominated by lensing B-modes. The primordial B-mode signal from gravitational waves is theorized to peak around $\ell = 100$, steeply declining after entering the horizon. This is because the tensor inflationary field does not scale with gravity in the photon-baryon fluid as the scalar field does. At larger angular scales beneath the horizon, the amplitude of the B-mode signal dictates the energy scale of inflation. The current constraint on r is given by Planck as $r_{0.002} < 0.06$ [3]. Not only is this an extremely faint signal, making it difficult to measure, but foregrounds mask the primordial signal and need to be carefully subtracted.

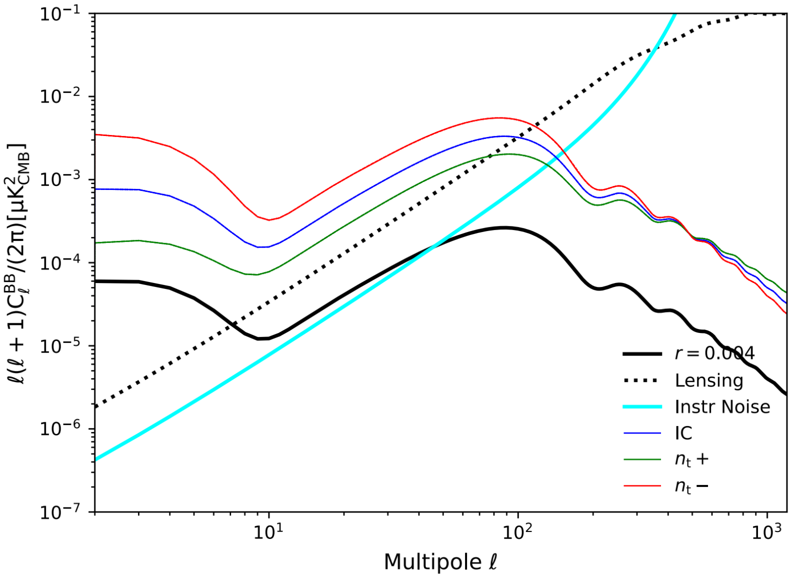

Figure 1.6: A plot of $D_\ell^{BB}$ showing primordial B-mode power spectra in several different solutions compared with the lensing B-mode power spectrum. Instrumental noise shown is the estimated instrumental noise of a next-generation experiment in cyan. The red, blue, and green curves represent fiducial models with a varying tensor spectral index $n_t$ at a fixed $r_{0.05} = 0.05$ [16].

## 1.4 Foregrounds

The primary foreground components that obscure the primordial B-mode signal are galactic dust, synchrotron emission, and gravitational lensing (shown in Figure 1.7). Each of these components needs to be accurately measured in order for a primordial signal to be revealed in analysis.

### Galactic dust

In the plane of our galaxy, galactic dust populates the interstellar medium. This dust absorbs radiation from stars and emits polarized IR radiation with a signal bright enough to contaminate the primordial B-mode signal across the whole sky. The polarized dust signal is typically brightest relative to the CMB signal at higher frequencies, increasing in brightness with frequency, from ~220 GHz to 1000 GHz. The frequency of the polarized galactic dust signal extends past the CMB science bands, allowing for measurement at high frequencies. With a precise characterization at high frequencies, the dust signal can be extrapolated to lower frequencies and subtracted.

### Synchrotron emission

The galaxy's magnetic field accelerates relativistic charged particles, which can then emit synchrotron radiation. The radiation is polarized by the structure of the galactic magnetic field and therefore introduces a polarized foreground into CMB measurements. Synchrotron radiation dominates lower-frequency measurements from ~10 GHz to 50 GHz, decreasing in brightness with frequency. Similarly to dust, by characterizing synchrotron emission at low frequencies, the signal can be extrapolated and subtracted from the CMB measurement.

### Gravitational lensing

E-modes gravitationally lensed by large-scale structure into B-modes dominate the BB power spectrum above $\ell \sim 50$, as discussed in the previous section. The lensing spectrum is typically removed by correlating the B-mode power spectrum with measurements of large-scale structure [17], or with high-resolution CMB measurements.

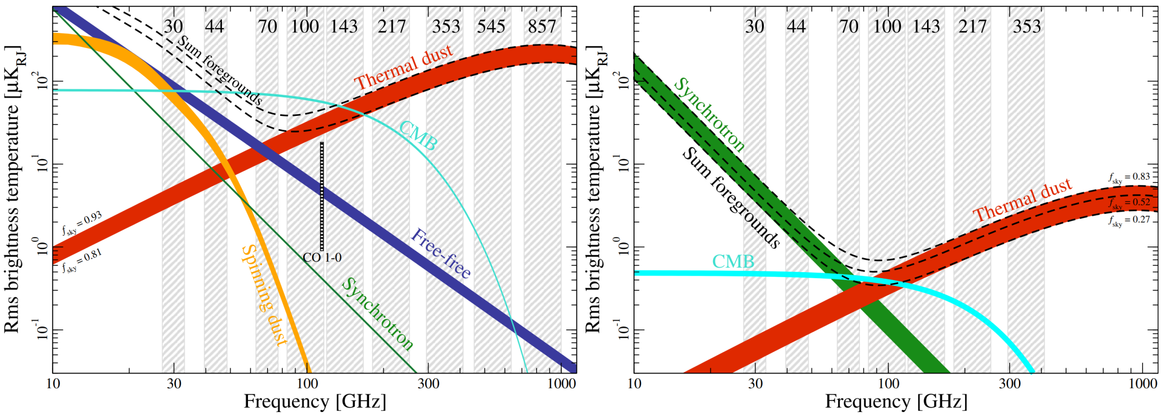

Figure 1.7: Brightness temperature as a function of frequency for temperature (left) and polarization (right) of various foreground components. [12].

# Chapter 2

# CMB Experiments

Anisotropies in the CMB were first detected in 1992 by the COBE experiment [8]. Since then, many ground-based telescopes, balloon experiments, and space-based experiments have continued to characterize anisotropies in the CMB with increasing precision. The current generation of CMB experiments aims to measure CMB polarization to provide further constraints to the cosmological parameters, including the tensor-to-scalar ratio r. Attempting to find the exceptionally faint B-mode signal from primordial gravitational waves requires experiments with unprecedented sensitivity.

Figure 2.1 shows the evolution of CMB experiments using raw sensitivity measured in $\mu K$. Next-generation ground-based CMB telescopes will utilize not only technological progress to increase sensitivity but also the continued trend of increasing detector count. Next-generation space-based experiments will similarly take advantage of more detectors than previous CMB satellites, but with fewer total detectors than ground-based experiments, CMB satellites leverage the lack of an atmosphere to achieve higher overall sensitivity, as well as a larger measured sky fraction to improve sample variance in the power spectrum.

This chapter outlines several current and next-generation experiments that the Berkeley CMB group is involved in.

## 2.1 POLARBEAR-2

The Simons Array consists of two actively observing telescopes, POLARBEAR-2a (PB-2a) and POLARBEAR-2b (PB-2b). These telescopes are located in the Atacama Desert at an altitude of 5,000 meters. For ground-based CMB telescopes, avoiding as much water and atmosphere as possible is critical, as oxygen and water are bright in the CMB science bands, with troughs in emission centered around 90 and 150 GHz. As such, PB-2a and PB-2b observe using dichroic detectors, measuring with frequency bands centered around 90 and 150 GHz.

PB-2a and PB-2b are identical crossed-Dragone-style telescopes, reflecting light from a primary mirror to a secondary mirror and then into the experiment's receiver. Measurement

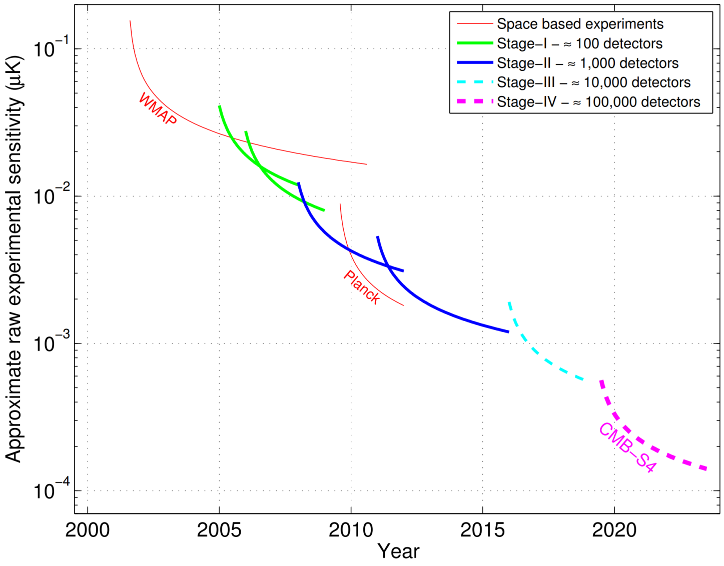

Figure 2.1: Plot of raw experimental sensitivities for various 'stages' of CMB experiments corresponding to detector count. [18]

Figure 2.2: The PB-2a telescope pre-deployment (left) and the PB-2a focal plane (right).

in two frequency bands presents a number of challenges, including developing an achromatic half-wave plate and multilayer antireflection (AR) coatings for dielectric surfaces. New multilayer AR coatings were developed for each dielectric surface in the receivers. In addition, both telescopes utilize continuously rotating half-wave plates in order to mitigate the effect of atmospheric emission as well as various systematic errors, further discussed in 3. While PB-2a utilizes a warm half-wave plate, a cryogenic half-wave plate was developed for PB-2b for lower emission to further increase sensitivity.

All of the Simons Array telescopes use a lenslet-coupled planar antenna design with TES bolometer detectors. While POLARBEAR measured at a single frequency and used a double-slot dipole-style antenna, PB-2a and PB-2b both use a log-periodic, or fractal, antenna with constant impedance as a function of frequency for sensitivity to larger a larger overall bandwidth, measuring both frequency bands with a single antenna. Further details of lenslet-coupled sinuous technology are discussed in Chapter 4.

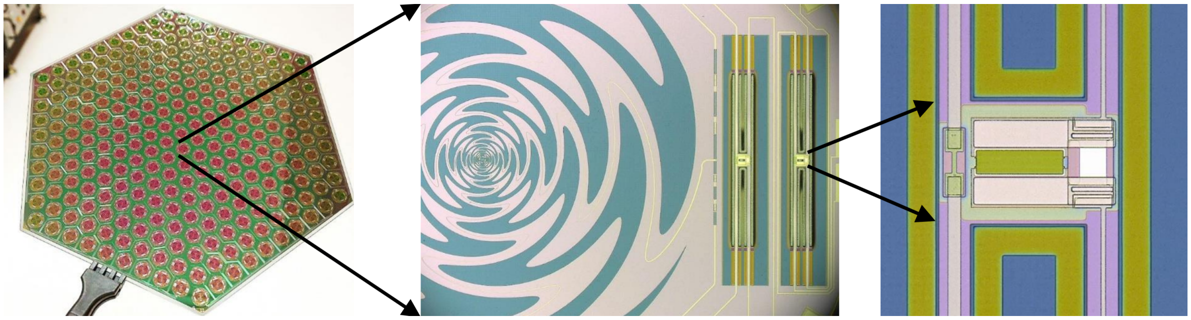

Figure 2.3: A PB-2a detector wafer (left) showing the array's sinuous antenna (center) and TES bolometers (right) sensitive to 90 and 150 GHz bands.

With a total detector count ∼7,600, the PB-2a and PB-2b telescopes approach the threshold for a Stage-III experiment, targeting higher-sensitivity polarization anisotropy measurements at large angular scales.

## 2.2 Simons Observatory

The Simons Observatory (SO) is a next-generation CMB experiment that is a joint collaboration of both Simons Array researchers, and Atacama Cosmology Telescope (ACT) researchers. Deploying ∼60,000 Simons Observatory is sometimes considered a 'stage 3.5' experiment and aims to constrain the tensor-to-scalar ratio r at the level of $\sigma(r) < 0.003$ [19].

SO will field a 6 m crossed Dragone style large aperture telescope receiver (LATR) as well as three 42 cm small aperture telescopes (SAT) [20]. The LATR consists of seven individual optics tubes, each with three lenses and a focal plane of detector arrays, with ≈40% of the sky and a predicted white noise performance of 6 $\mu K$-arcmin in the combined 93 and 145 GHz bands. Each SAT will field seven detector wafers, measuring ≈10% of the sky with predicted white noise levels of 2 $\mu K$-arcmin in the combined 93 and 145 GHz bands [19].

SO will measure frequency bands centered at 27, 39, 93, 145, 225, and 280 GHz to characterize synchrotron radiation and galactic dust foregrounds for removal from the science bands. Bands from 93 - 280 GHz will utilize polarization sensitive horn-coupled ortho-mode

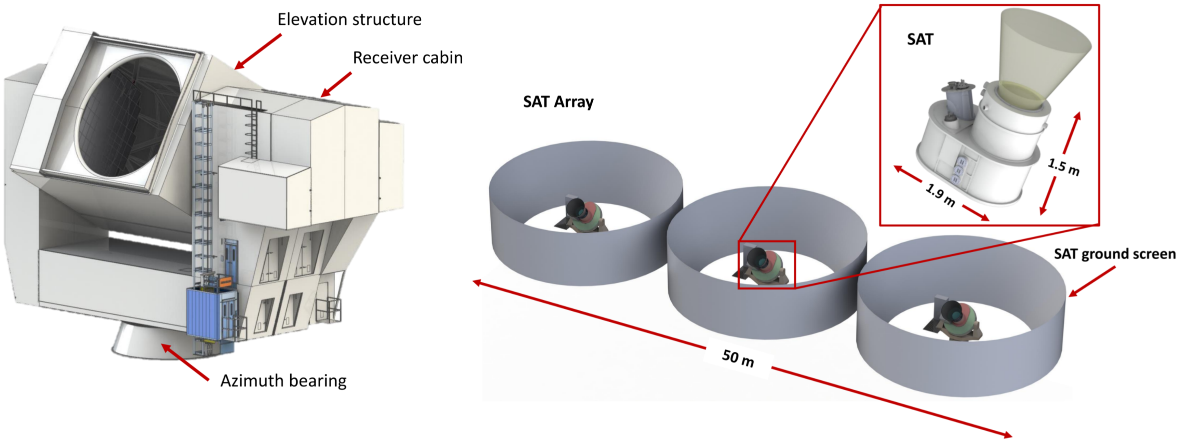

Figure 2.4: Renderings of the SO LATR (left) and SATs (right) telescopes, taken from [20].

transducer arrays, while 27 and 39 GHz bands will utilize lenslet-coupled sinuous antenna arrays, all using TES bolometer detectors.

## 2.3 LiteBIRD

Following the success of the Planck telescope, the JAXA led space mission LiteBIRD aims to characterize B-mode polarization to unprecedented levels. While Planck had in total 52 detectors in its high-frequency instrument [21] and 44 in its low-frequency instrument [22] (96 in total), LiteBIRD will use a total of 4,508 detectors [23]. With a huge leap forward in space-based CMB telescope detector count, LiteBIRD looks to constrain r to the level of $r < 0.001$ with an experimental sensitivity of 2 $\mu K$-arcmin [24]

LiteBIRD will measure the CMB using a low-frequency telescope (LFT) and a mid-high-frequency telescope (MHFT). LFT will consist of eight arrays measuring frequency bands centered at 40, 50, 60, 68, 78, 89, 100, 119, and 140 GHz. These arrays will utilize a lenslet-coupled sinuous antenna design and TES bolometer detectors, at two different pixel sizes [25]. The MHFT is broken down into two individual focal planes, one considered the mid-frequency telescope (MFT) and the other the high-frequency telescope (HFT). The MFT will consist of seven lenslet-coupled sinuous antenna arrays measuring at 100, 119, 140, 166, and 195 GHz, while the HFT will consist of three horn-coupled OMT arrays measuring at frequency bands centered around 195, 235, 280, 337, and 402 GHz [26], all using TES bolometer detectors. A breakdown of each of these focal planes is shown in Figure 2.6.

With a large experimental bandwidth, LiteBIRD will be able to measure the galactic dust and synchrotron signals over multiple frequency bands, allowing for precise characterization and removal. An increased bandwidth requires the development of next-generation metamaterial AR structures for all dielectric materials, achieving high in-band transmission while

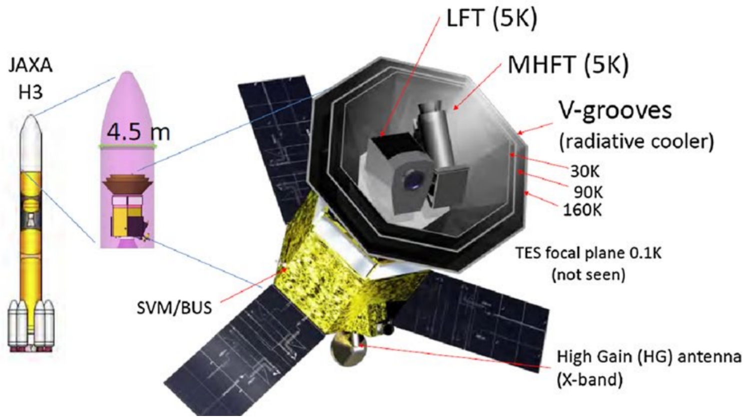

Figure 2.5: Conceptual design of the LiteBIRD labeling various components (left) and a drawing of LiteBIRD's spin and precession design [24].

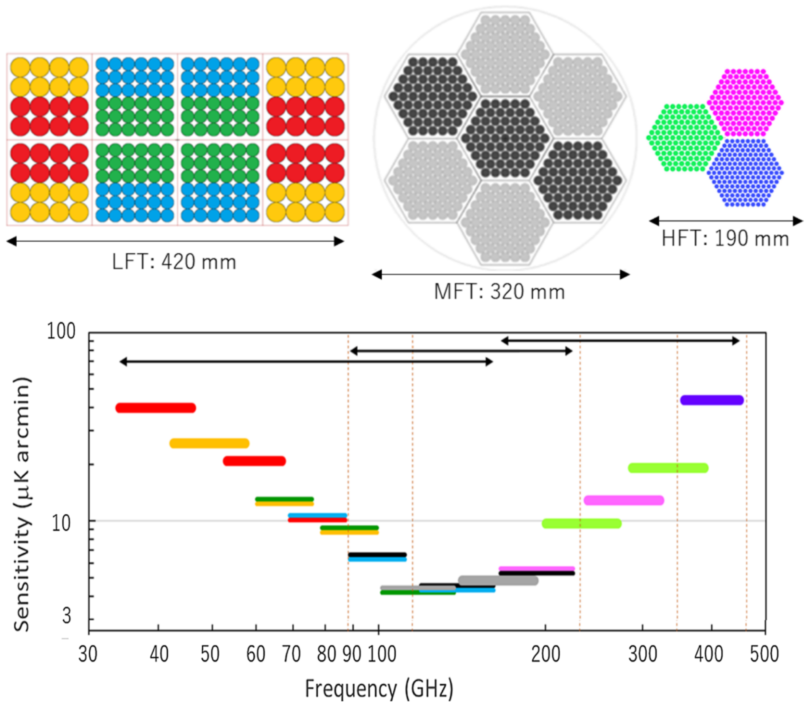

Figure 2.6: Top: Drawings of the LiteBIRD LFT (left), MHFT (center), and HFT (right) focal planes. Bottom: Plot of estimated raw sensitivity as a function of frequency, displaying LiteBIRD bands in colors corresponding to pixel type [24].

mitigating the risk of AR coating delamination. Metamaterial AR coatings are discussed further in Chapter 6.

Currently, LiteBIRD has a projected launch date in the late 2020s, launching on the Japanese H3 rocket.

## 2.4 CMB Stage 4

A notable future experiment that the Berkeley group is involved with is CMB stage 4 (CMB-S4). CMB-S4 will consist of 12 telescopes in both the Atacama Desert and at the South Pole, deploying around 500 horn-coupled ortho-mode transducer detector arrays with a total of 550,000 TES bolometer detectors. With an order of magnitude more detectors than any previous CMB experiment, CMB-S4 aims to put an upper limit on r of $r < 0.001$ at 95% confidence or measure r at a $5\sigma$ level if $r > 0.003$. CMB-S4 looks to achieve first light in the early 2030s. First light for CMB-S4 is planned for the early 2030s.

# Chapter 3

# Warm HWP Technology Development

## 3.1 Introduction to HWPs

One tool used to combat telescope beam systematics as well as to lower atmospheric 1/f noise in CMB experiments is an optical element known as a half-wave plate (HWP). HWP's introduce a phase shift of 90 degrees into polarized light, where the relative phase shift $\Gamma$ is defined by

$$\Gamma = \frac{2\pi \Delta n L}{\lambda_0}. \tag{3.1}$$

Here, L is the thickness of the birefringent material, $\lambda_0$ is the desired wavelength of light, and $\delta n$ is the difference in the index of refraction between the two crystal axes of a birefringent material. A birefringent material is one whose index of refraction varies given the polarization of incident light. For a HWP, $\Gamma$ is fixed at 90 degrees, and the parameters $\Delta n, \lambda_0$, and L are chosen to accommodate sensitivity to a desired wavelength. To achieve a higher linear polarization modulation efficiency ($\epsilon_{mod} = P_{out}/P_0$) over a broader range of frequencies, birefringent materials can be combined with crystal axes rotated relative to each other creating what is called an Pancharatnam achromatic HWP [27].

By rotating a HWP at some frequency, polarized light is rotated 90 degrees four times at the frequency of rotation. This modulated signal can be demodulated in order to extract the polarized light signal that was incident on the HWP.

Polarization modulation has a number of advantages in CMB science. For ground-based experiments, unpolarized large angular scale atmospheric fluctuations, caused by spatial variations in water vapor density, wind, and other atmospheric effects, increase experimental 1/f noise. However, this signal can be excluded by demodulating the modulated polarized signal, suppressing experimental 1/f noise, and increasing polarization sensitivity at large angular scales. For ground-based experiments looking for low-$\ell$ primordial B-mode signals, suppressing the 1/f noise from unpolarized atmospheric emission is critical, as the intensity of the sky signal is many orders of magnitude brighter than the B-mode signal.

Next, ground-based and space-based CMB experiments alike are prone to systematic errors caused by beam distortions via the telescope or focal plane optics, as well as gain calibration mismatches in orthogonal polarimeters. Both of these effects can cause differential signals in orthogonal polarimeters, known as intensity-to-polarization (I-to-P) leakage.

Without the use of a HWP, CMB experiments can reduce 1/f noise by differencing the signals from two orthogonal detectors. This defines the polarization in terms of the Stokes parameters Q and U, as discussed in 1.3.2. Ideally, two orthogonal detectors observing an unpolarized signal can be differenced to remove their equivalent 1/f signals, leaving a purely white noise residual. Although differencing can work well in practice, I-to-P leakage caused by experimental systematic uncertainties can leave a residual intensity signal.

By employing a continuously rotating HWP, the sky polarization signal can be separated from signals via these systematic errors. This relaxes requirements on beam and gain calibration and protects against other effects such as temperature drifts in the optics and readout noise variation. By rotating the polarized signal, a single polarimeter is able to observe two orthogonal linear polarizations, where excluding normalization factors, the signal the detector sees goes as

$$\left\langle |E_x(t)|^2 \right\rangle cos^2(\omega t) + \left\langle |E_y(t)|^2 \right\rangle sin^2(\omega t) \rightarrow I(t) + Q(t)cos(2\omega t), \tag{3.2}$$

where $\omega$ is $2\pi$ times the rotation frequency of the HWP. Here, the Stokes parameter Q(t) is directly proportional to the amplitude of the modulated signal, removing the need for detector differencing. It should be noted that to modulate the polarized signal above the 1/f knee, the HWP rotation frequency must be large relative to the frequency of variation in I(t) for a given scan speed and detector time constant.

## 3.2 PB-2a WHWP design and evaluation

Half-wave plates have been adopted by a number of CMB experiments, including POLARBEAR, POLARBEAR-2, and Simons Observatory, to name a few. Ambient temperature, or, warm HWP (WHWP) designs have been implemented in POLARBEAR and PB-2a, while PB-2b and SO use cold HWP designs, all continuously rotating [28].

A WHWP design is disadvantaged compared to a cryogenic design because of its larger black body emission. A HWP's emissivity adds a noise equivalent temperature (NET) component to the NET of the experiment's detector arrays, where NET is the minimum temperature that can be detected at a signal-to-noise ratio (SNR) of one. A common figure of merit used for CMB experiments is the mapping speed of an experiment.

$$MS = \frac{1}{NET_{arr}^2}. \tag{3.3}$$

For PB-2a, a cryogenic HWP was originally baselined to reduce HWP emission and improve mapping speed, however, it was decided that the development of a cryogenic HWP would not be completed before the deployment date, and thus PB-2a would use an ambient temperature HWP between the telescope's secondary mirror and optics tube.

A WHWP for PB-2a would be exposed to the harsh seasonal temperature changes of the Atacama desert and, as such, a number of considerations needed to be made in order for its optical properties to be maintained along with its ability to consistently rotate for stretches of time over the course of multiple years. All aspects of the HWP needed to take into account longevity and the ability to withstand steep temperature changes. An AR coating that uses vacuum to adhere the AR layers would also need to be included with the ability to passively hold a vacuum for weeks at a time while under rotation. In this section, all these design considerations are discussed in detail.

While former Berkeley graduate student Charlie Hill was responsible for the optical design of the PB-2a HWP, the HWP work done for this dissertation was purely focused on the mechanical design and validation of the PB-2a WHWP, and thus, this section will detail the PB-2a WHWP exclusively with a focus on the mechanical design.

### 3.2.1 POLARBEAR precedent

Preceding the PB-2a WHWP, POLARBEAR's continuously rotating ambient temperature HWP was introduced in 2014 with the aim of measuring lower $\ell$ ranges than previous years of observation (see Figure 3.1). Before deploying a WHWP, POLARBEAR took measurements covering the angular multipole range $500 < \ell < 2100$ [29]. Following the implementation of a WHWP, POLARBEAR was able to reduce its 1/f knee to 32 mHz, corresponding to a multipole $\ell \cong 39$ [30].

With the precedent set by POLARBEAR's retrofitted HWP, polarization modulators were baselined for the Simons Array telescopes.

### 3.2.2 Optical design

An experiment's polarized mapping speed will scale with the square of its polarization efficiency [31], highlighting the importance of maximizing a HWP's polarization efficiency. Given that PB-2a measures both 90 GHz and 150 GHz, an achromatic HWP design is required, increasing the polarization efficiency over a larger bandwidth. The modulation efficiency requirements for PB-2a are $> 95\%$, requiring a three-plate stacked sapphire design with crystal axes rotated at 0, 54, and 0 degrees with respect to each other. Figure 3.2 shows the effectiveness of the three-plate design of PB-2a compared to a single-plate design.

The HWP modulation efficiency was measured by mounting the birefringent stack to a rotational stage and passing polarized light through it using a ceramic heater source with a wire grid. The HWP modulation efficiency of the PB-2a sapphire stack was measured to be $> 98\%$ in both 90 and 150 GHz bands, exceeding the PB-2a requirements.

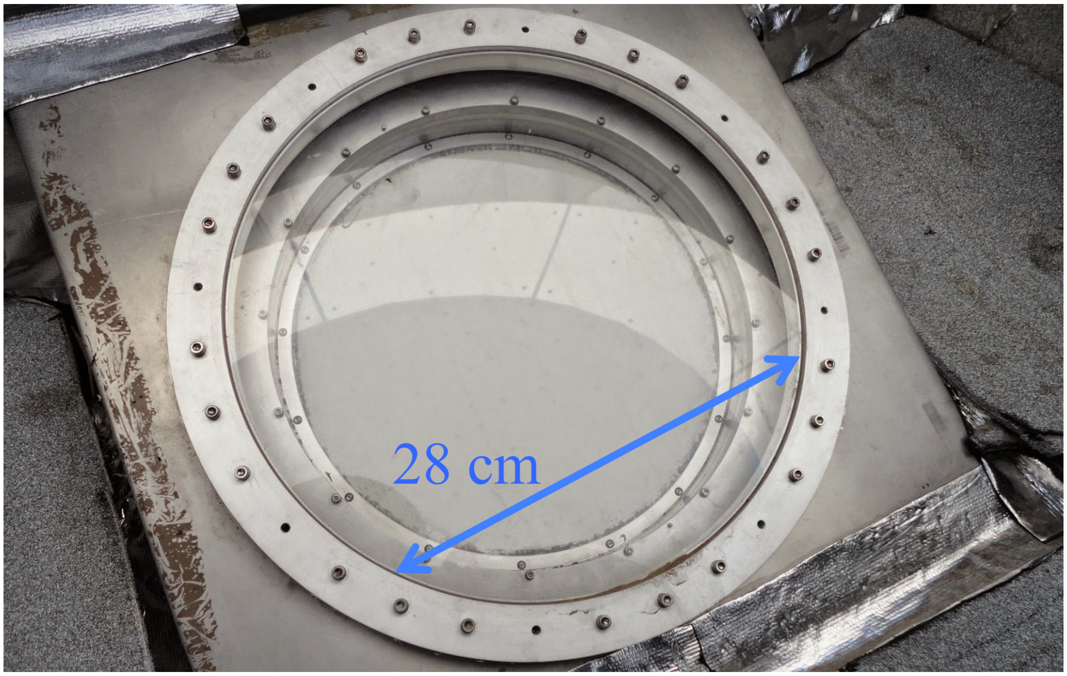

Figure 3.1: A photograph of the POLARBEAR WHWP deployed in 2014. The HWP was placed between the primary and secondary mirrors of the telescope. A 280 mm diameter plate of sapphire, along with a RT/duroid 6002 AR coating and mylar sheet for weatherproofing all comprised the window.

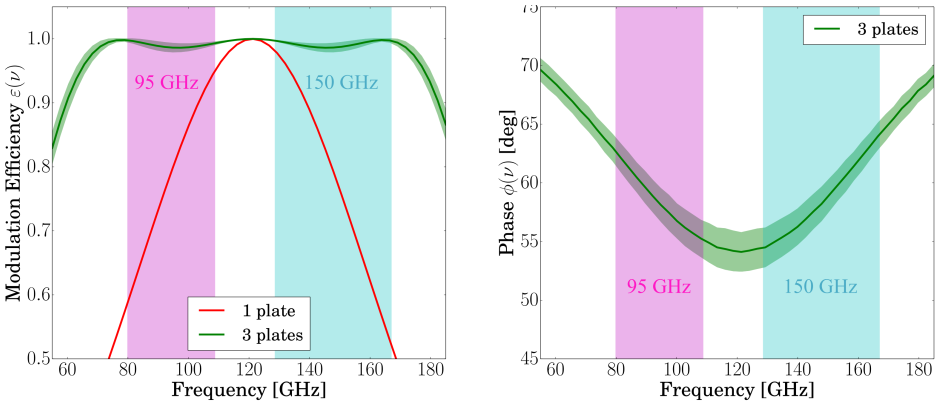

Figure 3.2: The calculated modulation efficiency for a 1 vs. 3 plate achromatic HWP design (left), and the phase offset of the center plate in order to achieve maximum transmission at 120 GHz (right). Plots created by Charlie Hill, image taken from Hill, Beckman et al. [28].

### 3.2.3 AR coating

A number of considerations were made to ensure that transmission was maximized while emissivity was minimized through the HWP. Namely, choosing optimal materials and thick-

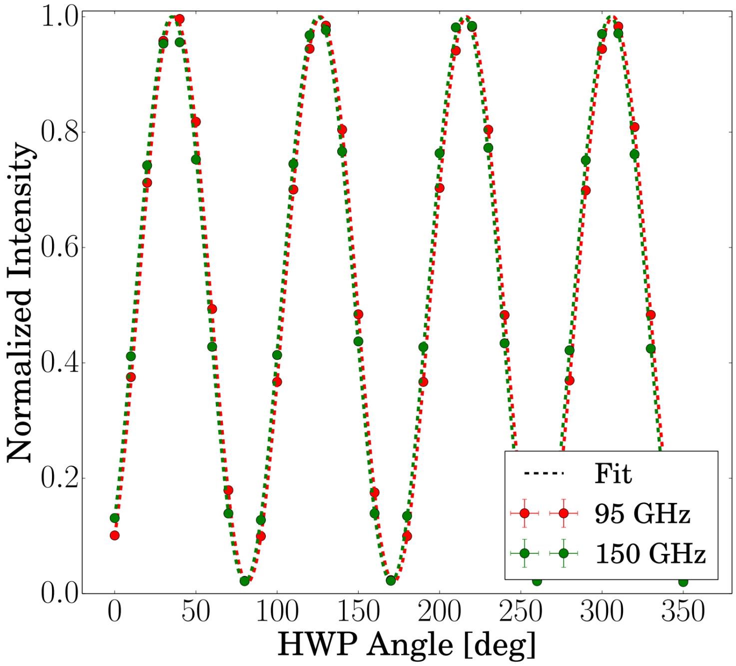

Figure 3.3: The normalized, measured intensity as a function of HWP rotation angle at 95 and 150 GHz. Measurement by Charlie Hill, image taken from Hill, Beckman et al. [28].

nesses for an AR coating as well as low-dielectric loss materials for both the birefringent material and for the AR coating layers. Sapphire was selected for the birefringent material because of its low-loss tangent. For the AR coating, a band-averaged two-layer coating with a 120 GHz center frequency was designed, using a 0.27 mm thick RO3006 duroid sheet, below a 0.38 mm thick layer of HDPE plastic. These materials were chosen for their low loss tangents and optimal indexes of refraction for the two-layer coating design [28]. 5.1 outlines the detailed functionality of various AR coatings, including a two-layer design as used in the PB-2a HWP.

To adhere the AR layers to the sapphire, the idea of using a glue layer was explored. However, the use of a glue layer posed several problems. Primarily, even a 20 $\mu$m thick glue layer would increase the emissivity of the HWP at 90 and 150 GHz by around 20% . Reflections caused by an index-mismatched glue layer of this thickness would be around $<$ 3% at 150 GHz [31]. Another issue was that if the glue was not applied perfectly evenly, the HWP would have differential emission and reflection properties on its surface. This would cause what is called a HWP synchronous signal (HWPSS), and if modulated at the rotation frequency, it can be coupled to $4f$ modes, becoming indistinguishable from the sky signal. For these reasons, a vacuum system was designed utilizing atmospheric pressure to push the layers against the AR coating. The design would require a vacuum hold for $>$ 1 month, with the intention of occasionally pumping the system down when it is installed on the telescope.

A vacuum gauge is mounted to the vacuum system and is monitored via a webcam with PB-2a's live monitoring system to ensure that vacuum is maintained while observing. In testing, a degradation of transmission was observed at a vacuum level of -3 inHg. On the telescope, the system is pumped on well before reaching this threshold.

The vacuum system utilizes the outer HDPE layer to create the vacuum seal for the module. HDPE is glued to an aluminum ring that then clamps against an o-ring positioned in the rotating section of the HWP (shown in Figure 3.4).

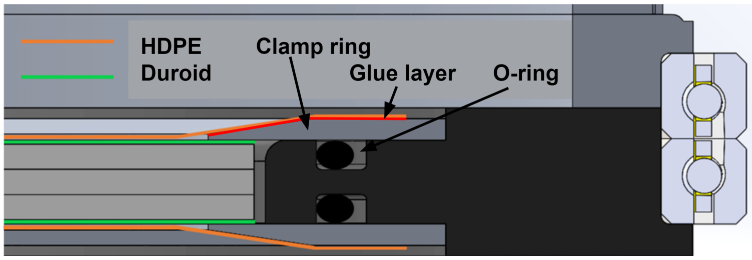

Figure 3.4: Cross-section of the PB-2a WHWP, showing the vacuum AR coating design. An additional volume to extend the vacuum life (not shown) is mounted to the bottom of the rotating section (dark grey).

Two different types of glue were used to adhere the HDPE to the aluminum clamp ring (see Figure 3.5). The glue used to make the vacuum seal was selected for its flexibility when cured, while maintaining the ability to bond unlike materials. The selected glue was Reltek BONDIT 8482-TH, used with Reltek A-3 Primer. The intention of this layer is to maintain a vacuum seal and act as an o-ring of sorts, maximizing the vacuum hold time. The function of the second glue was specifically to create as strong a bond as possible between aluminum and plastic to protect against delamination caused by the strong shear force of the vacuum. Various glues were tested by adhering sheets of HDPE to a prepared aluminum surface and hanging an increasing weight off of the HDPE until it deformed or detached from the aluminum. The clear winner of this test, surprisingly, was a common two-part epoxy called JB-Weld, which can be found in any hardware store.

With this combination of glues, the windows successfully survived vacuum and proved mechanically robust, as they are still spinning on the HWP in PB-2a at the time this dissertation is being written, seven years after they were fabricated. Although mechanically robust, the seal eventually leaked small amounts of vacuum, degrading the hold time of the HWP. These small leaks were fixed at the telescope site in Chile by using a helium leak checker to find the leak location and patching it using the same Reltek epoxy.

In lab testing, a similar leak checker was used to ensure that the system was holding vacuum well. Initial testing showed that even in the most sensitive leak checker setting with no observed leaks, the vacuum hold time was less than one week. This was attributed to the small volume of the system, and a circular tube was added around the aperture (shown in Figure 3.6) to increase the total volume of the system. The tube was then balanced using rotating copper masses. With this addition, at sea level, the vacuum was shown to remain

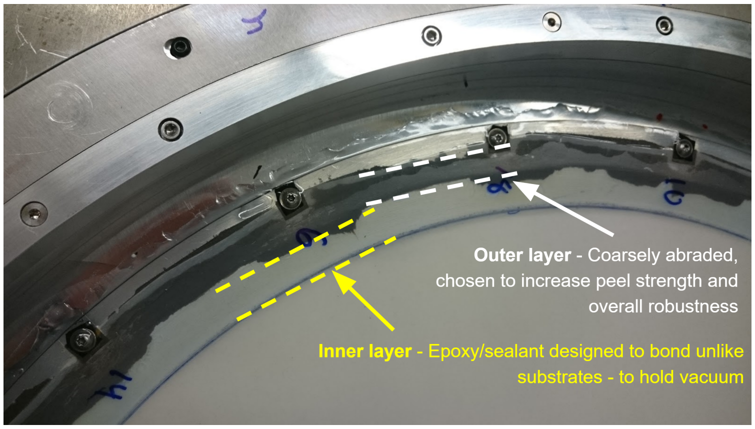

Figure 3.5: Image of the PB-2a WHWP vacuum seal created by glue adhering HDPE to the aluminum clamp rings.

above 10 inHg while rotating at 2.2 Hz for more than one month before being shipped to integrate with the PB-2a receiver in Japan. At the Chile site, where the atmospheric pressure is around half that at sea level, the WHWP can hold vacuum during continuous operation for one month before additional pumping is required.

Figure 3.6: (Left) The volume expansion tube on the sky-side of the HWP and (right) the vacuum plumbing with the gauge used to monitor pressure.

Fully assembled, transmission measurements were taken across the 90 and 150 GHz bands using a Fourier transform spectrometer (discussed in further detail in 4.5.2). The average in-band transmission was measured to be 95.9% in the 90 GHz band and 94.1% in the 150 GHz band [28].

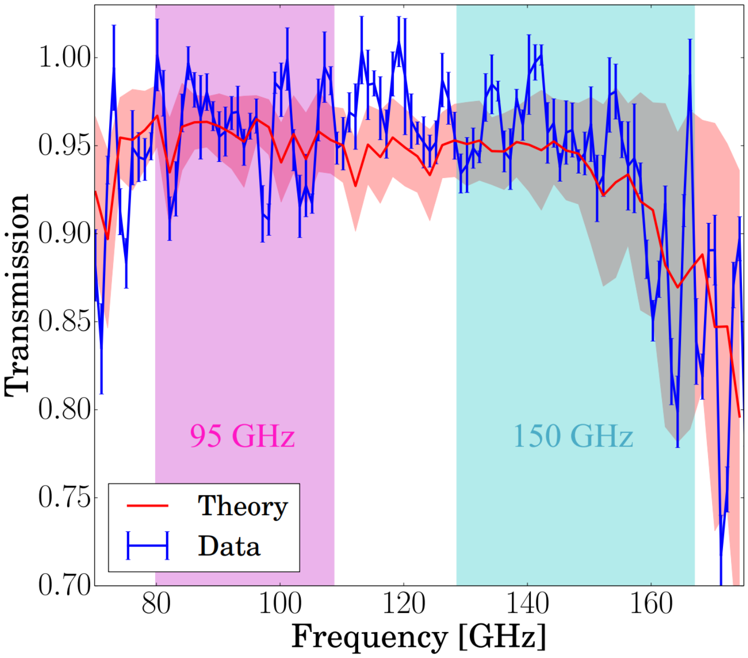

Figure 3.7: FTS transmission measurements across the PB-2a 90 and 150 GHz bands plotted with a simulated transmission curve. Measurement by Charlie Hill, image taken from Hill, Beckman et al. [28].

### 3.2.4 Angular velocity requirement

For large angular scale measurements it is crucial that the HWP frequency is high enough to adequately reduce the 1/f knee. With the telescope scanning at ∼1 degree per second [28], a requirement for a WHWP rotation frequency of $> 2$ Hz was determined to be sufficient to modulate the signal band above the unpolarized atmospheric 1/f frequency seen at the Simons Array site [32].

A drive system was selected to be able to withstand rotation of the HWP mass up to three times the baseline frequency of 2.2 Hz to ensure a high safety factor and reliable long-term rotation. Initially, an air bearing system was considered, but a steel ball bearing was selected not only for faster implementation but also for increased overall reliability and simplicity. A matched pair thin-section bearing, designed to rotate safely under predicted HWP loads, ensures reliable and resistance-free rotation at any orientation. This is important, as the instrument's orientation will change with the telescope, creating time-varying loads in the bearing. The bearing is packed with MOLYKOTE 33 light extreme low-temperature grease, so that it can function properly at cold temperatures in during Chilean winter.

A 400 W AC servo motor is used to rotate the HWP via a belt drive system. A large pulley was machined into the rotating section of the HWP and a drive pulley mounted to the servo system was selected to ensure that the motor is not stressed at 2.2 Hz rotation. An adjustable belt tensioner is designed in the stationary baseplate to ensure proper belt tension.

The drive system was tested using a dummy rotating mass at up to 7 Hz without issue and was rotated with the full optical stack under vacuum for three months in lab, experiencing no issues before deployment.

### 3.2.5 Angular resolution requirement

A potential source of HWP noise comes from the error in measurement of the HWP angle. This error in the HWP's reconstructed angle couples with Q polarization to induce noise in U polarization. The NET of the HWP scales with the reconstructed angle's error and must be minimized relative to the array's NET. For this, an angle noise requirement for the PB-2a HWP was given to be

$$\sigma_\chi \ll 3\frac{\mu rad}{\sqrt{Hz}}, \tag{3.4}$$

[31] where $\sigma_\chi$ is the RMS of an angle error $\Delta\chi$, which requires a time resolution of less than 10 ms.

To keep track of the HWP's position accurately, an optical encoder from RSF Elektronik is used. This steel tape encoder has 10,000 reflective lines around a 636 mm diameter aluminum ring mounted to the rotating section measured with an infrared readhead mounted to the baseplate. With 4x interpolation, the encoder system achieves a resolution of 6.5 arcseconds. An Arduino Leonardo ETH microcontroller is used to read out the encoder signal, sampling at 15 kHz, and the resulting angle resolution is given by

$$\sigma_\chi = \frac{6.5\, arcsec}{\sqrt{12}}\sqrt{\frac{1}{1.6\times 10^4 Hz}} = 0.015\frac{arcsec}{\sqrt{Hz}} = 0.073\frac{\mu rad}{\sqrt{Hz}}. \tag{3.5}$$

where the factor of $1/\sqrt{12}$ is the standard deviation of a uniform distribution. This accounts for the random sampling of the Arduino signals between the encoder signals. This angular resolution is $\ll 3\,\mu rad/\sqrt{Hz}$ and is considered to contribute negligible noise to the demodulated data. The data from the arduino is time stamped via the telescopes universal clock and is paired with corresponding data for analysis.

### 3.2.6 Mounting the HWP

Unlike the POLARBEAR WHWP that was placed at the telescope's prime focus, the PB-2a WHWP is placed after the telescope's secondary mirror, in-between the mirror and the optics tube. Placing the HWP at the optics tube, after the secondary mirror, provides a number of optical benefits, but requires the birefringent aperture to be larger than when placed at prime focus as in POLARBEAR (between the primary and secondary mirrors). Placement further away from the optics tube at prime focus increases parasitic optical power on the

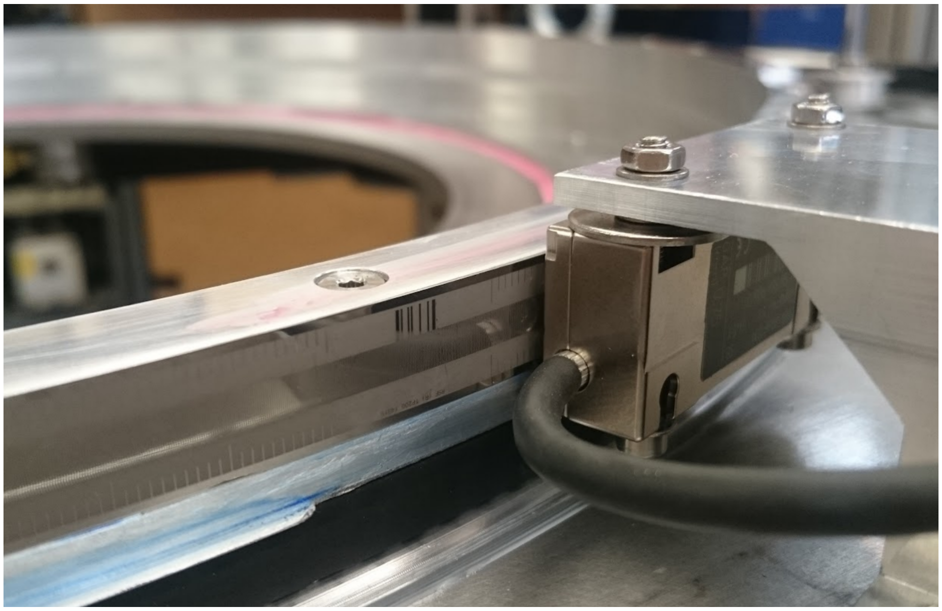

Figure 3.8: The WHWP's encoder tape and encoder readhead, mounted on the rotating section and baseplate respectively.

detectors due to stray light, a bulk of which can come from ground pickup or the reflection of thermal radiation off of various telescope surfaces. Another unfavorable effect of placement at prime focus is the increased susceptibility to HWPSSs. Because the light is most tightly collimated here, a given pixel will illuminate a more localized region of the HWP relative to a less tightly collimated position, such as in front of the receiver. This makes it more susceptible to interaction with a given nonuniformity in the sapphire or AR coating on the HWP itself, amplifying the effect of HWPSSs. These, amongst other benefits, motivated the choice to place the PB-2a HWP after the secondary mirror, as close to the optics tube as possible. In this configuration, an exceptionally large 500 mm birefringent aperture was required.

The HWP uses a five-axis positioning 80/20 structure designed with to be able to translate in three dimensions and rotate in two. This allows for precise positioning using photogrammetry once installed in the telescope. Vibration isolating mounts are also used to mount the baseplate to the 80/20 structure. These isolate three dimensions of vibration, mitigating potential microphonic pickup in the detectors.

### 3.2.7 Deployment

The PB-2a WHWP was deployed in November 2018. After minor repairs to the vacuum system, the HWP has remained operational since. Using the WHWP, I-to-P leakage was shown to be $< 1\%$. In April 2023 the WHWP was used in an axion-like particle search and

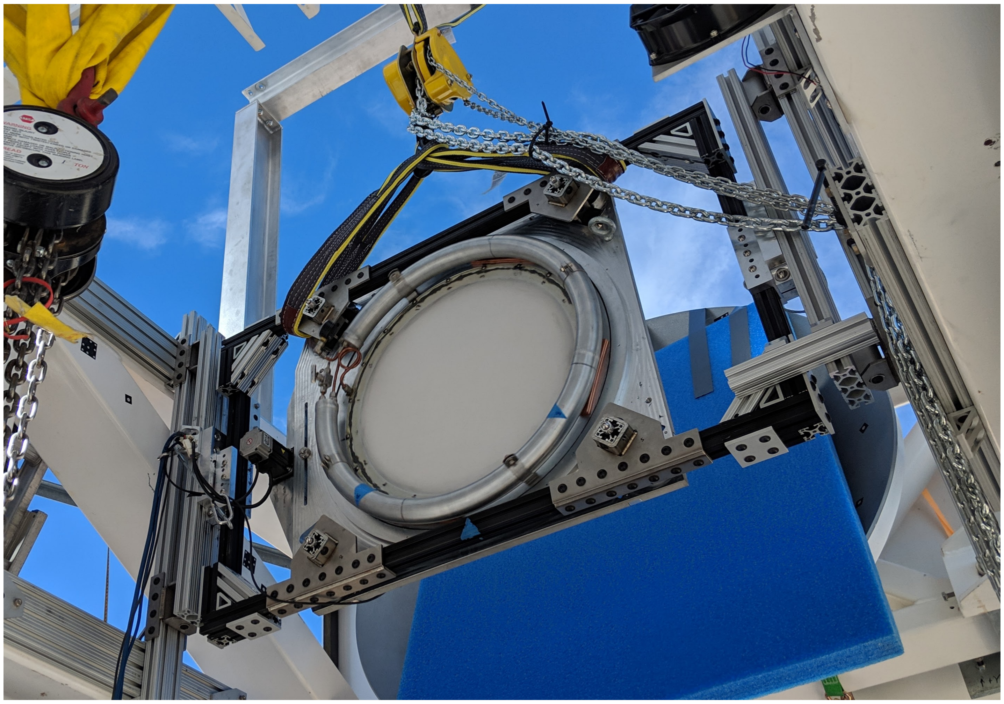

Figure 3.9: A picture of the WHWP installed in the PB-2a telescope in November of 2018.

observed continuously until July 2023. Observing again in August 2023, the HWP has been continuously operated through the time that this dissertation was written.

# Chapter 4

# Focal Plane Modules and Detector Arrays

At the heart of a CMB telescope is its focal plane, specifically, its detector arrays. Detector arrays are responsible for coupling light onto the antenna and converting light into an electrical signal that can be analyzed. Securely mounting these arrays to the focal plane is critical, as in order to perform their function in the first place, they must be held securely while they cool to their sub-kelvin base temperatures and through the duration of their deployment. This section details the focal plane module designs for experiments relevant to this dissertation, along with the antenna and detector technologies they utilize.

## 4.1 Introduction to focal plane modules

There are many parts of a focal plane module, all which serve a critical purpose to the functionality the detector wafers.

For the Simons Array, Simons Observatory LF, and LiteBIRD LF and MF telescopes, a lenslet-coupled planar antenna design is used. This means that light illuminating the focal plane is focused onto a planar antenna (a sinuous antenna in this case) via a hemispherical lens and silicon extension piece, together approximating an elliptical lens.

The light produces an electrical response in the antennas that is then carried through band-defining filters and detected by a transition edge sensor (TES) bolometer, and then it is amplified and read out. The back lobe of the antenna must be carefully controlled as well, in order to mitigate crosstalk between pixels. Typically a back-short or back-absorber is placed behind the antenna to either reflect the back lobe back towards the antenna or absorb the light, respectively, reducing reflection.

The lenslets, silicon extension, detector wafer, and detector backshort/absorber must all be contained in a module that interfaces with both the focal plane itself and the readout electronics assembly. Because these experiments operate at sub-Kelvin temperatures, differential thermal contraction between dissimilar materials must be taken into account.

Once a focal plan module has been designed, components must be tested in lab both together and individually. Various mechanical, cryo-mechanical, and optical tests are performed to ensure optimal performance before being integrated into the telescope.

## 4.2 Lenslet-coupled sinuous antenna

### 4.2.1 Lenslet introduction

A 'hemispherical substrate lens' was first used by Rutledge *et al.* in 1982 [33] in order to increase the sensitivity of early millimeter and far infrared imaging systems. Simply put, this is a dielectric hemisphere placed onto one side of a planar antenna. With this lens design, light can be focused from the receiver's optics onto individual antennas in an array, each with their own substrate lens focusing light, increasing forward gain.

Figure 4.1: Close up of an SO-LF lenslet array. Here, silicon lenslets with a single-layer glass AR coating are used. The full array can be seen in the reflections on each lenslet.

Another advantage that comes from placing a dielectric lens on one side of a planar antenna is that the antenna emission will be preferentially directed towards the dielectric. This approximates an infinite dielectric half-space for the antenna, where the antenna will radiate preferentially towards the higher dielectric constant. With this effect, the higher the dielectric constant of the lens, the more pronounced the effect. Because of this, high-dielectric substrates are typically chosen for lenslets, usually alumina ($\epsilon = 9.6$) or silicon ($\epsilon = 11.7$). Without using a lenslet, the forward radiation of a double-slot dipole antenna or a sinuous antenna can decrease by as much as 40% given a silicon substrate lenslet [34]. An advantage of alumina lenslets is that they are mechanically more resistant to cracking due to coefficients of thermal expansion (CTE) mismatches between the substrate and its AR coatings; however, due to a higher dielectric constant, a silicon lenslet provides slightly more forward gain via this infinite dielectric half-space effect.

One parameter that is used to better couple the lenslet's beam to beam from a telescope's receiver optics is the L/R ratio of the hemisphere. Here, some thickness L of a dielectric serves as an extension to help focus the lenslet's beam. L is typically the length of a silicon or alumina extension piece plus the silicon detector wafer, and R is the radius of the lenslet. Given a fixed lenslet radius (typically defined by the pixel pitch of the experiment and the required thickness of an AR coating), one can vary the extension length to change the optical properties of the approximated ellipse and maximize forward gain.

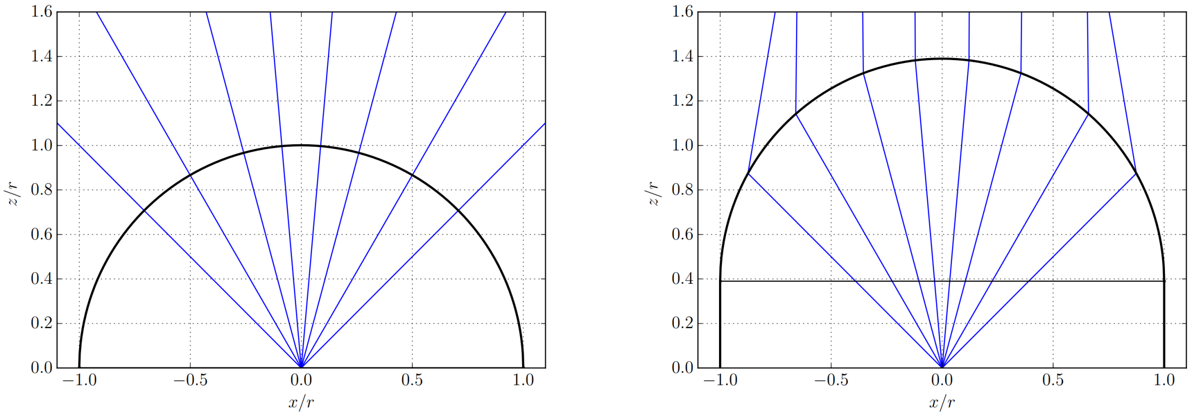

Figure 4.2: (Left) an example of a silicon lenslet with zero extension length, resulting in no refractive power. (Right) A silicon lenslet with an optimized extension length for its radius, focusing parallel rays. Plots via Ariel Cukierman.

For Simons Observatory low-frequency lenslets, integrated forward gain was simulated over an L/R sweep to determine an optimal L/R ratio. This is shown for a simulated L/R sweep in a SO-LF 40 GHz pixel in Figure 4.3.

Another important design aspect for a hemispherical lenslet is its anti-reflection coating. The AR coating must be designed to maximize transmission in a given band while remaining robust to differential thermal contraction at the substrate-AR interface. Various types of lenslet AR coating designs are discussed in more detail in Chapters 5 and 6.

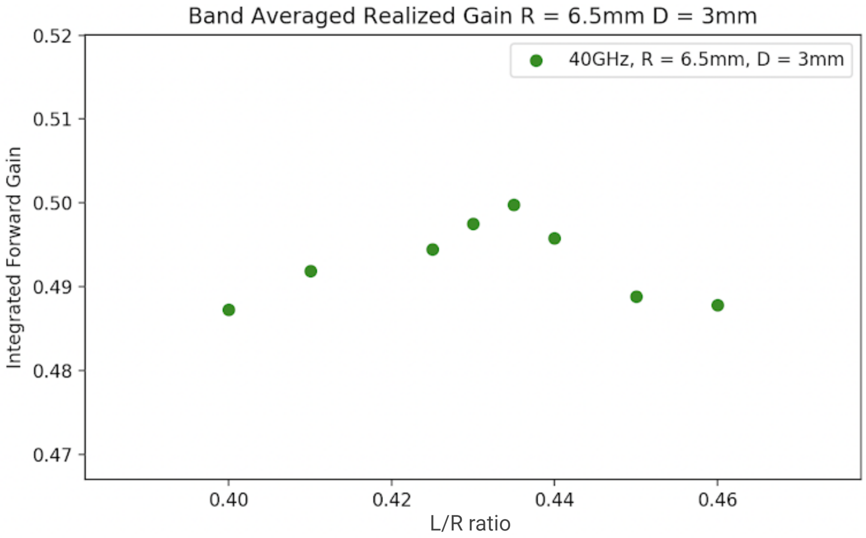

Figure 4.3: This plot shows the results of an HFSS simulation, simulating the integrated forward gain vs. L/R ratio for a 6.5 mm lenslet at 40 GHz for SO-LF. The results show an optimal L/R ratio of ≈0.43. Simulation done by Aashrita Mangu.

### 4.2.2 Sinuous antenna

A sinuous antenna is an example of a log-periodic antenna that employs a self-repeating design to achieve sensitivity to a wide range of frequencies. For CMB experiments, the type of sinuous antenna used is a two-dimensional, dual-polarization design. Its fractal nature gives the antenna a constant impedance as a function of frequency, which results in a bandwidth that is theoretically limited only by the overall size of the antenna. In practice, however, even though the lowest frequency will only physically be limited by the size of the antenna, the highest frequency to which an antenna is sensitive is limited by the lithography resolution during fabrication, and the overall bandwidth is limited by the AR coating of the lenslets and telescope optics.

The sinuous design can be described in polar coordinates r and $\phi$ by the following equation

$$\phi = \alpha \sin\left[\pi \frac{\log(r/R_1)}{\log(\tau)}\right] \pm \delta, \tag{4.1}$$

where each rescaling of $\tau^2$ sweeps through an angle of $\pm\alpha$.

An undesirable property of the sinuous antenna that is a result of the curvature in the arms of the sinuous defined by $\tau$ is something called polarization wobble. This curvature results in a response to the polarization angle that varies as a function of frequency, allowing polarization power to leak into orthogonal channels. To combat this, orthogonal channels can be differenced to remove the wobble, but at the expense of a small amount of optical

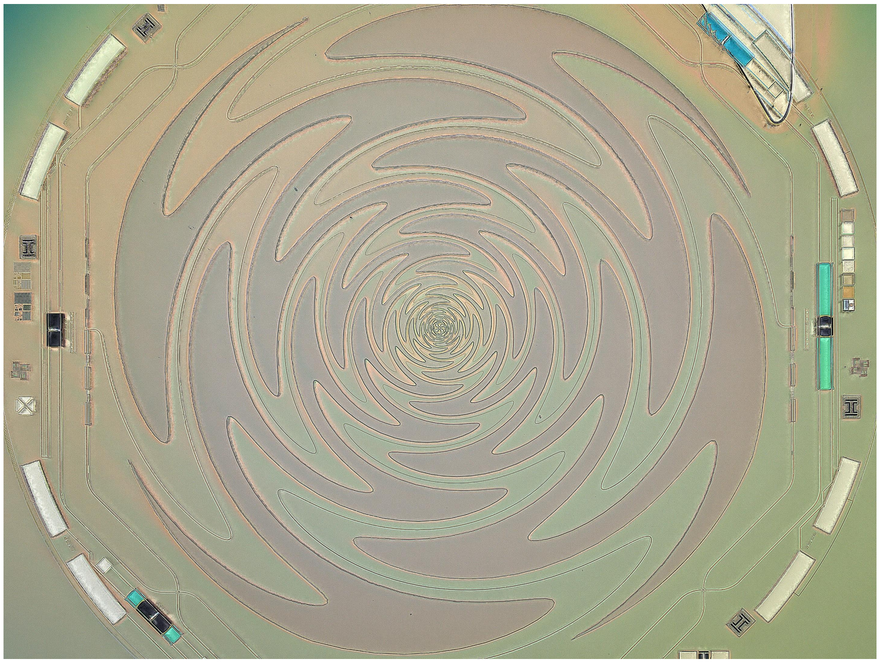

Figure 4.4: Example of sinuous antenna. This particular antenna is an SO-LF pixel.

efficiency [35].

## 4.3 Detectors

When the antenna couples to incident radiation, it is fed by a transmission line known as a micro-strip line, made of a superconducting metal. This microstrip line utilizes on-chip microwave bandpass filters to define a frequency band before the signal is terminated at a resistive element on the detector called the absorber.

The detectors used to measure the electrical response of the sinuous antenna are TES bolometers. A TES bolometer consists of an absorber that terminates the antenna's transmission line, a thermistor (the TES), and the bolometer's legs to define the thermal link to the wafer temperature, or bath.

The absorber is a resistive element that is designed to match the impedance of the antenna's microstrip lines and filters to avoid signal loss due to reflections. This element is typically made out of a thin titanium film. In this case, it is also called a titanium load resistor. This load resistor absorbs the in-band optical power and is thermally linked to the TES. The TES is designed as a thermistor, whose resistance will change as a function of temperature. A TES is made from a thin-film superconductor, aluminum manganese, for example [36]. During operation, the total power on the bolometer island will be exactly such

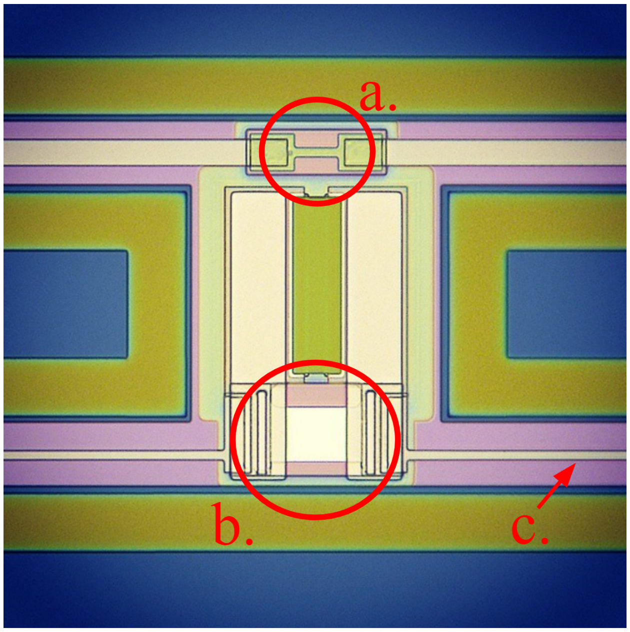

Figure 4.5: Image of a TES bolometer. a. the absorber, connected to the sinuous antenna's transmission line, b. the transition edge sensor, c. the legs of the TES bolometer.

that the TES remains in superconducting transition. In a steady state, the total power that is conducted to the bath is then

$$P = P_{opt} + P_{elec}, \tag{4.2}$$

where $P_{opt}$ is the incident optical power seen by the TES through the load resistor, and $P_{elec}$ is the electrical power across the TES provided by a small voltage bias, $V_{bias}$, where $P_{elec} = V_{bias}^2/R$, and R is the operating resistance of the TES. This constant voltage bias then is what allows the total power across the bolometer island to be such that its held in its superconducting transition, where a small change in temperature at the TES via the load resistor will correspond to a sharp change in resistance. This means that when $P_{opt}$ increases, the temperature of the load resistor and therefore the TES will increase, increase R, and decrease $P_{elec}$. The opposite happens when there is a drop in optical power, as the bolometer temperature decreases, R will decrease, increasing $P_{elec}$. This electrothermal feedback loop is shown in Figure 4.6.

The amount of power that is conducted to the bath is determined by the thermal conductance of the bolometer, $G(T)$. This value is determined by the temperature of the system and the exact bolometer leg geometry and composition that together define the weak thermal link.

To describe the thermal behavior of the bolometer based on this information, we can

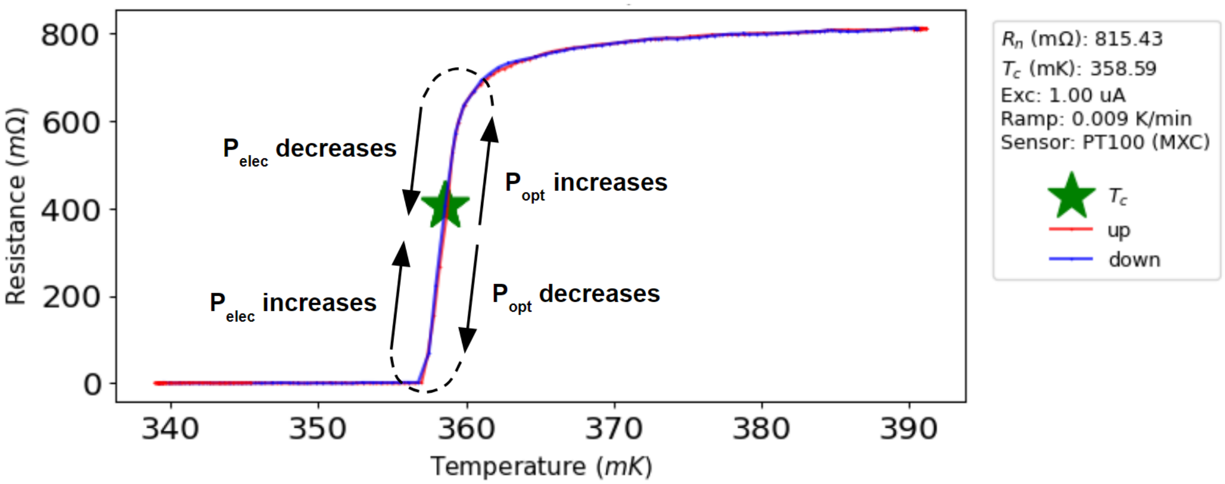

Figure 4.6: Plot of a bolometer's superconducting transition with Tc ≈360 mK, and electrothermal feedback mechanism overlaid.

refer to the thermal differential equation 4.3 provided by K.D. Irwin and G.C. Hilton in [37]

$$C\frac{dT}{dt} + P_{bath} = P_{opt} + P_{elec}, \tag{4.3}$$

where C is the heat capacity of the TES and absorber, and T is our evolving state variable, the temperature of the TES. Here, $P_{bath}$ is the power conducted from the TES to the bath and can be rewritten in equation 4.3 as a function of the thermal conductance of the bolometer.

$$C\frac{dT}{dt} + \int_{T_{bath}}^{T_{bolo}} G(T)dT = P_{opt} + P_{elec}, \tag{4.4}$$

where now the total power power conducted out of the bolometer to the bath is

$$P = P_{opt} + P_{elec} - \int_{T_{bath}}^{T_{bolo}} G(T)dT = C\frac{dT}{dt}, \tag{4.5}$$

and $C\frac{dT}{dt}$ describes the energy stored in the bolometer as a function of time.

In the absence of electrothermal feedback, the equation 4.4 can be rewritten as

$$C\frac{dT}{dt} = -\int_{T_{bath}}^{T_{bolo}} G(T)dT, \tag{4.6}$$

and a natural thermal time constant can be defined

$$\tau \equiv \frac{C}{G}, \tag{4.7}$$

where $\tau$ describes the time it takes for the bolometer to dissipate its heat energy to the bath.

### 4.3.1 I-V curves and saturation power

A useful measurement to determine certain properties of a bolometer is an I-V curve. In this measurement, the bias power is varied across a TES, starting with a high enough bias voltage to ensure the TES is normal and decreasing the voltage through the superconducting transition until the TES is superconducting (see Figure 4.7). The current across the TES is then measured, and from this, the resistance as a function of bias voltage can be calculated.

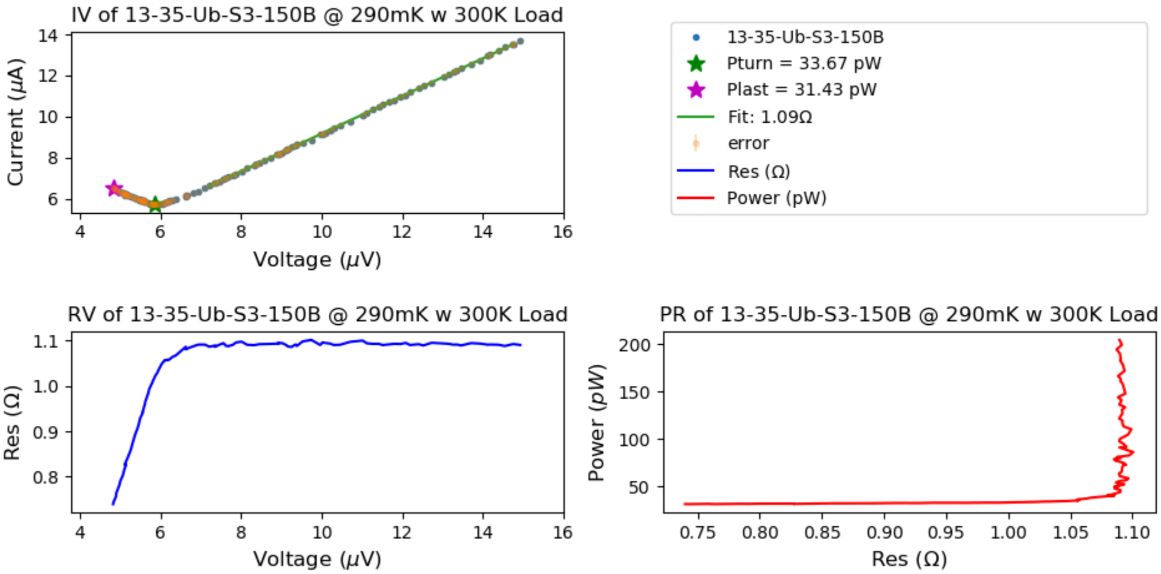

Figure 4.7: A measurement made from a 150 GHz bolometer by sweeping the bias voltage, starting with a high enough voltage to hold the TES normal, and lowering it through its superconducting transition. The upper left plot shows the output current of the bolometer as a function of bias voltage. The lower left plot shows the change in bolometer resistance as a function of bias voltage. The lower right plot shows the total power on the bolometer as a function of its resistance as the bias voltage was swept. The constant power regime shows the saturation power of this particular detector, which is ≈31 pW

Using the known bias voltage and current, a useful quantity called saturation power ($P_{sat}$) can be determined. This is the power that is maintained on the bolometer via electrothermal feedback while the bolometer is in transition. A bolometer's saturation power can be adjusted via its weak link to the thermal bath. The higher the heat flow to the bath, the lower its saturation power will be, as it will not be able to store as much heat in a given period of time. In practice, the saturation power can be adjusted by changing the leg length of the bolometer, modifying its thermal conductance properties. Using this method, we can write

$$P_{sat} \propto \frac{1}{L_{leg}}, \tag{4.8}$$

where $L_{leg}$ is the bolometer's leg length.

## 4.4 Focal plane modules

The complete assembly of lenslets and detectors that go into an experiment can be called a focal plane module. These modules must be designed to accommodate differential thermal contraction while providing a thermal and mechanical interface to the detector arrays. This section will discuss all of the constituent components of a focal-plane module up to the readout.

### 4.4.1 The silicon stack

The silicon detector array and silicon lenslet array must be interfaced in a way such that they are aligned to each other to within some specification - i.e. the lenslet must be concentric to its antenna to with this specification. If the lenslet and the antenna are not concentric, the quality of the beam will start to degrade, becoming asymmetric and non-Gaussian, and the optical efficiency of the lenslet will start to degrade. To ensure adequate centering of the antenna to the lenslet, the experiments POLARBEAR-1, Simons Array, and SPT-3G use alignment markings on both the lenslet array and onto the detector wafer. These two wafers are then manually aligned under and infrared microscopes while being clamped into their invar detector holder. The degree of freedom for the silicon to move in the plane of wafers is what allows for their alignment; however, it means that the alignment accuracy relies on the person assembling the stack. Although this can be done consistently, it also allows for human error and increases the handling time of the detector wafers.

For smaller-scale tests at Berkeley using single pixels, similarly, the lenslet and detector chips previously had to be aligned by eye under a microscope with an x-y micrometer stage. Unlike the method of using markings and an infrared microscope, the center coordinate of the lenslet had to be defined relative to the edges of the lenslet extension piece using an optical microscope and x-y micrometer stage. After this, the lenslet and extension piece were flipped and the center was found again relative to the edges of the extension piece. Once the center was found, the detector chip was placed on the backside of the lenslet extension piece, and the center of the sinuous antenna was aligned with the center coordinate found. This was a long and tedious process that could take up to four hours, depending on the sample.

To improve both the alignment of full-sized detector wafers to their lenslet arrays, as well as sample pixels to their single lenslet, a new fabrication process was created. The lenslet array's extension wafer or, seating wafer, is typically etched on a single side to create pockets for each lenslet. These pockets are typically oversized by $+10\ \mu m$ in diameter over the diameter of the lenslet to ensure proper fit. At Berkeley, this etch is done using an STS-2 deep reactive ion etching machine in the Marvell Nanofabrication Laboratory. To improve the antenna-to-lenslet alignment process, a new process was developed that involves etching both sides of this extension wafer. On one side, the lenslet pockets are etched, and on the other side, a pocket is etched to retain either the full-sized detector wafer or the single-pixel test chip. Using this method, a detector-side pocket that is oversized by $+10\,\mu m$ edge to edge from the detector wafer has been shown to work well. Both etches contribute a potential $5\ \mu m$ error on antenna alignment, resulting in a total $+10\ \mu m$ potential alignment error.

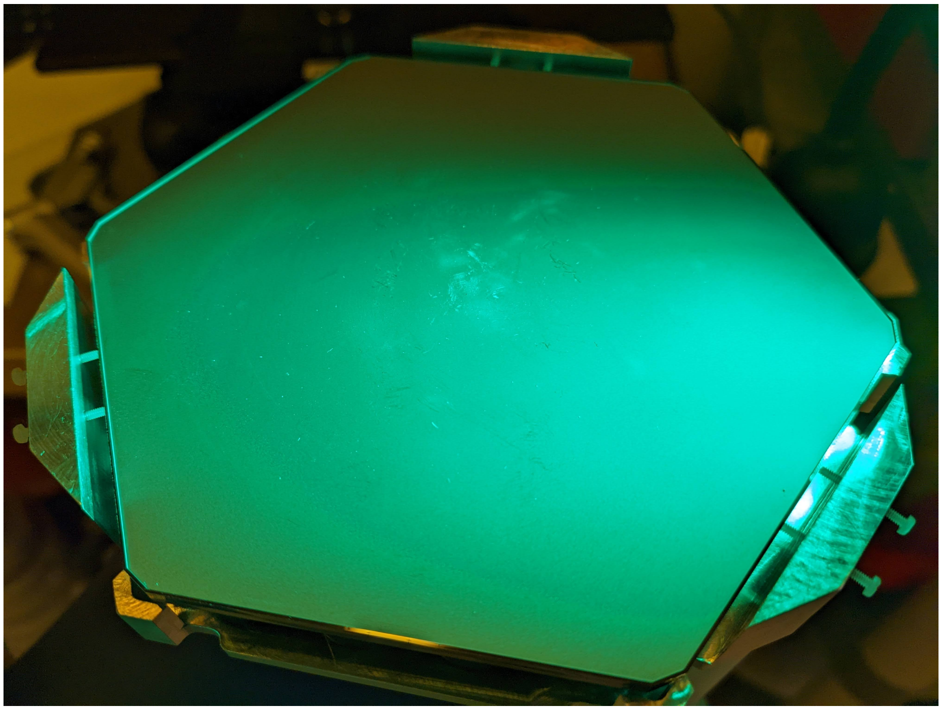

Figure 4.8: The etched detector wafer side of an SO-LF extension array.

At 150 GHz, a beam offset tolerance of 1 degree was given, informed by ray-tracing simulations and a beam tilt's affect on an experiments mapping speed. Figure 4.9, simulated by Aritoki Suzuki, shows the result of HFSS simulations that include offsets in both the lenslet and the lenslet's AR coating. It was found that a $10\ \mu m$ shift of the lenslet and its AR coating together correspond to a 0.53 degree tilt in the beam and is within spec.

For the Simons Observatory low-frequency arrays, this two-sided etch method was implemented. Using an edge thickness of $500\ \mu m$ on the detector side etch results in adequate mechanical robustness, and is used without chipping silicon at the sidewall of the extension wafer.

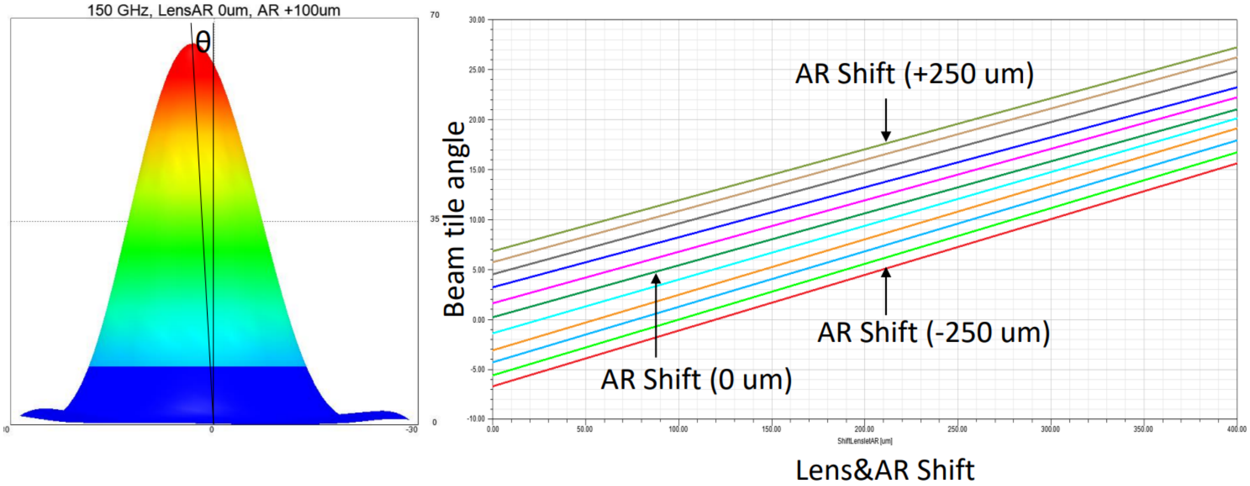

Figure 4.9: Simulation results provided by Aritoki Suzuki of the beam tilt given from a 100 micron lenslet-antenna misalignment (left), and the beam tilt angle vs. lens and AR shift for various AR coating offsets (right).

### 4.4.2 Invar detector holders

The interfaces for the lenslet array-detector wafer stack are an invar frame and clamps that pin the silicon stack to the invar frame. This can be seen in Figure 4.10

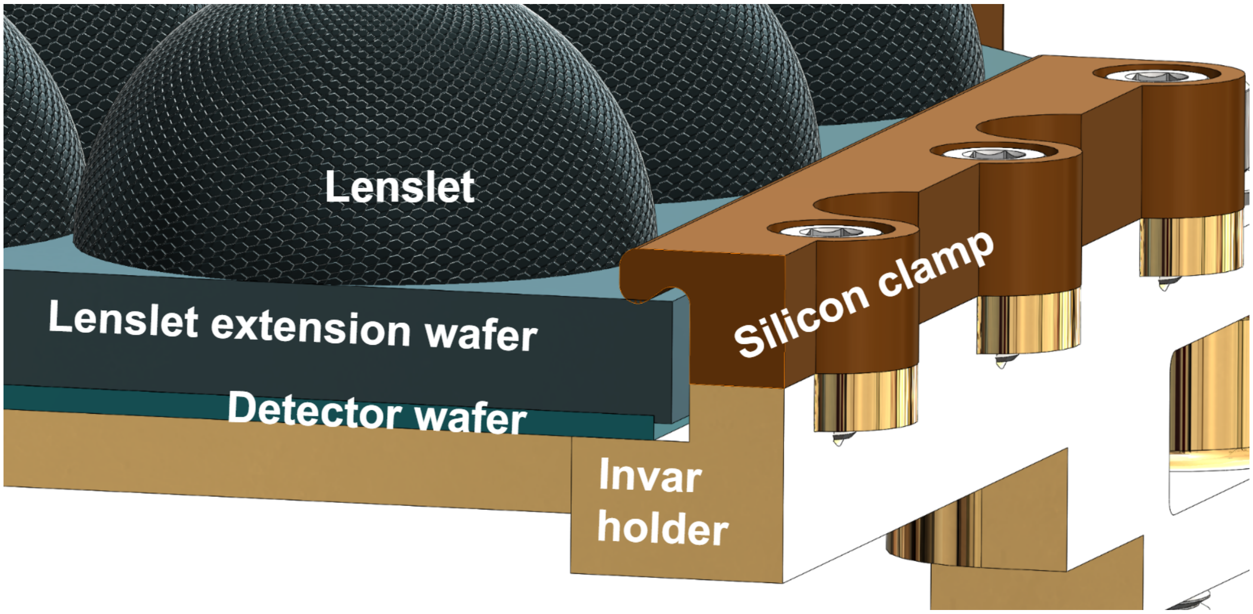

Figure 4.10: A cross-section of a prototype LiteBIRD LF detector module.

Invar, a nickel-iron alloy, exhibits very low levels of thermal expansion compared to other metals. Because of this, it is typically used at any silicon-metal interface. Invar has a thermal expansion coefficient between ~2 - 5$\times10^{-6}K^{-1}$, while copper has a CTE of ~17.0$\times10^{-6}K^{-1}$. Looking at silicon's CTE, it is much more closely matched to invar's, at ~2.5$\times10^{-6}K^{-1}$. The length of a linear contraction given a change in temperature is given by

$$\Delta L = \alpha L_0 \Delta T, \tag{4.9}$$

where $\alpha$ is the CTE of the material. Taking the example of a prototype LiteBIRD LF detector wafer with an edge-to-edge distance of 101 mm, cooling from 300 to 0 K sees a $\Delta L$ of ≈30 $\mu m$, while copper at that length would see a contraction of $\Delta L$ of ≈515 $\mu m$. This means that the gap at the edge of the silicon between the silicon and the copper would need to be at least ≈238 $\mu m$ on each side of the detector wafer. For certain experiments, such as LiteBIRD, an extra 475 $\mu m$ width per module can account for a significant fraction of the focal plane's dimensional margin. In practice, thermal contraction of a part containing complex features is determined more accurately by simulation in a program such as Solidworks Simulation, rather than calculated using 4.9. In addition to spatial requirements, the primary reason for using a low-CTE alloy at silicon interfaces is to avoid fracture of the silicon when cooling to mK temperatures.

### Silicon clamps

For the experiments POLARBEAR-1, Simons Array, and SPT-3G, invar was used to clamp the silicon stacks to their invar frames for the reasons outlined above. However, using invar for the clamp has the potential to chip the silicon lenslet array at its edges, as found when disassembling arrays with invar clamps. In addition, depending on the beam size and the height of the clamps, the beam coming from the lenslet has the potential to reflect off of these clamps to degrade the beam quality of edge pixels. For these reasons, a clamp made of the plastic vespel was researched. Vespel is a polyamide plastic that is specifically designed to maintain its mechanical properties under extreme temperature conditions. At cryogenic temperatures, vespel's stress-strain, as well as yield properties are conserved [38]. Despite having a higher CTE than invar, vespel's mechanical and optical properties along with its resistance to fatigue over time make vespel a primary candidate for a new cryogenic clamp.

The validity of vespel has been shown as clamps for silicon at Berkeley in more than 100 cooldowns, being used with both small samples as well as full-sized detector wafers. With this success, vespel was chosen as the clamping material in the SO-LF arrays. The SO-LF clamps have proven to have adequate clamping force for thermal conduction from the invar to the silicon, and to securely hold the arrays over cooldowns of multiple arrays in different cryostats around the country.

The SO-LF clamps are a design similar to the Simons Array and the SPT-3G clamp design, where six clamps are for one hex wafer, one at each of the corners (see Figure 4.11). However, this style of clamp has two properties that are not optimal and need to be corrected for the LiteBIRD detector arrays. Firstly, the clamps being at the corners of the silicon, applying the force at the weakest mechanical point of the silicon. For LiteBIRD, the clamps for the LF and MF wafers will clamp along each of the sides of the silicon wafers, rather than at the corners. The second design flaw of this clamp style shown in Figure 4.11, is that because the clamping face is levered out from where the clamp screw's torque is applied, when fully torqued down, the clamps will be slightly angled and therefore apply the clamp force along the edge of the silicon.

The LiteBIRD wafer clamps shown in Figure 4.10 are designed with a relief cutout above the edge of the silicon, so that they will only come into contact with the top face of the silicon lenslet arrays, rather than with the edges. Furthermore, there is a designed 100 $\mu m$ gap between the clamp and the invar. This gap is tuned to provide adequate clamp force for the silicon while requiring less than the screw's specified torque to compress the clamp across this gap. This was simulated in Solidworks Simulation to ensure adequate clamping force given the tolerances in the clamp height, the invar height, and the silicon stack height, as well as acceptable stress values in the vespel material. The cryogenic properties of vespel given in [38] are used for all simulations.

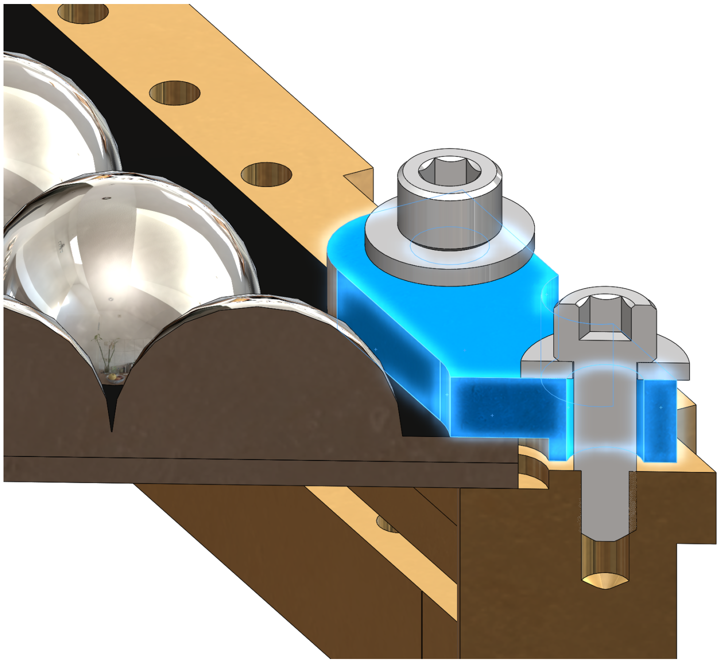

Figure 4.11: The cross-section of a Simons Array detector module with the invar clamp highlighted in blue.

### 4.4.3 Copper backshort design

In theory, it is not a problem for an antenna's backlobe to radiate into free space, but in practice this is not possible, as the backlobe will eventually reflect off of a metal surface, usually one used to mount readout components. This reflection can potentially cause standing waves and crosstalk between pixels when one antenna's backlobe reflects onto a neighboring antenna. Simons Array detector modules use a backtermination design, utilizing an absorbing material to damp potential standing waves. This method of controlling an antenna backlobe requires space for the absorbing material and a plate to mount the absorber. Space requirements for the Simons Observatory LF detector modules is smaller, and necessitates the use of a thinner, copper backshort to handle the termination of the antenna back lobes. To mitigate pixel crosstalk, the backshort is held as closely as possible to the detector wafer, with pockets cut for each individual antenna. In SO-LF detector modules, the distance between the wafer and the closest backshort surfaces is 250 $\mu m$ (see an SO-LF backshort in Figure 4.5). HFSS simulations comparing various depths of the backshort pocket have been shown to yield an efficiency gain of up to 5% when compared with the no backshort case, letting the antenna radiate into free space.

The primary mechanical design features to take into consideration for such backshorts are to compensate for thermal contraction and to maintain a certain flatness across the backshort. The LiteBIRD LF and MF detector modules are baselined to use backshorts as well, although it has not been decided whether copper, invar, or a metalized silicon stack will be used. A metalized silicon stack solves flatness and thermal contraction issues; however, for SO-LF, additional R&D was required that the detector module timeline did not allow. Invar would be another good choice for mitigating thermal contraction stresses, but because SO-LF readout is mounted directly to the backshort, concerns were raised about invar's high magnetic susceptibility impacting readout performance. For these reasons, a copper backshort was baselined for the SO-LF detector modules.

For SO-LF backshorts, If not accounted for, the thermal contraction of the copper will put pressure on the screws that bolt it to the invar frame, putting stress into the frame that could translate to the silicon. To account for this, firstly, all of the mounting holes are oversized. Second, a more subtle effect from the thermal contraction is a 'potato chipping', or deflection of the piece. This can occur if one face of the backshort has a higher volume of material than another, and hence the top and bottom faces differentially contract. For the SO-LF backshorts, features are machined into the detector-side face such that both the sky-side and detector-side faces contract equally, and this deflection is mitigated. This was done by calculating the detector-side surface's fill ratio given the pockets for the antenna back lobes and replicating this ratio on the detector side. The equal contraction on each side was then verified using Solidworks Simulation software. Though the equalized stresses in the copper backshort prevent any deflection towards the detector wafer, there is no guarantee that the copper will slip uniformly in the oversized holes under thermal contraction. However, in practice the invar frame and 3.8 mm thick silicon stack are capable of withstanding any additional stresses from non-uniform slipping without failure.

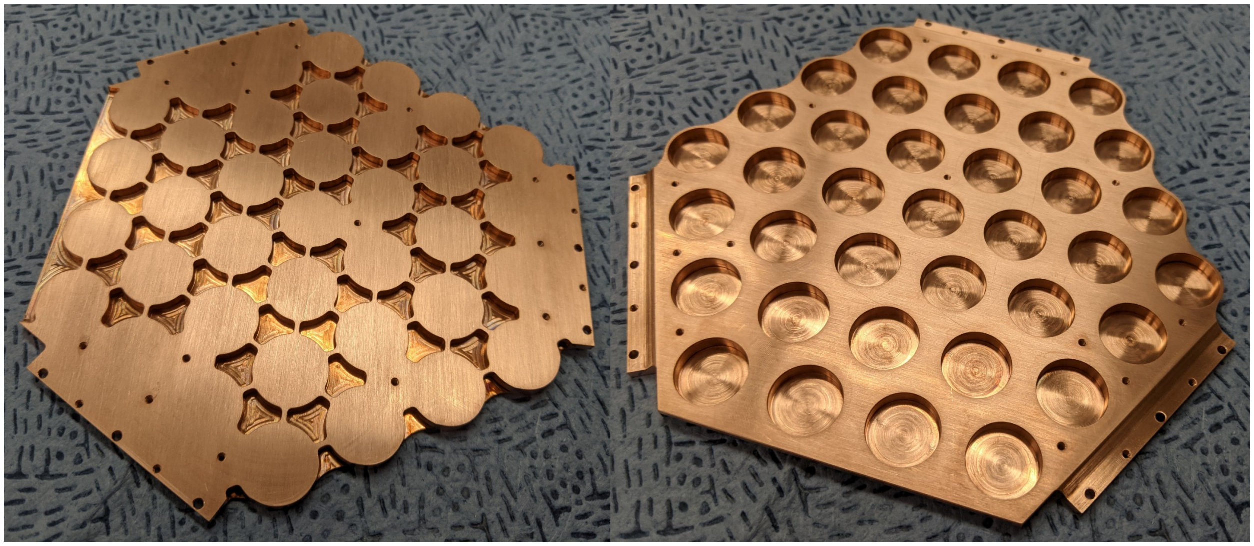

Figure 4.12: On the left is the sky-side face of a SO-LF backshort. The detector-side face is shown on the right.

Lastly, the final step to ensuring that the backshorts do not come into contact with the detector wafer is to machine the backshorts to an extremely small flatness tolerance. The UC Berkeley Physics machine shop is able to achieve a flatness tolerance of ±5 $\mu m$ in all backshorts they have made.

To verify that the backshorts do not come into contact with the device wafers, using a dummy detector wafer, feeler gauges are placed between the copper and the wafer (see Figure 4.5). The feeler gauges are then moved across the wafer surfaces to ensure a gap at every location on the wafer. This test is performed at room temperature and at 77 K in liquid nitrogen. For liquid nitrogen tests, the assembly is submerged in liquid nitrogen and removed once thermal equilibrium is reached. Feeler gauges are then inserted and the test described above is performed.

## 4.5 Lab testing and validation

In order to iterate on lenslet and detector wafer designs, extensive lab testing is required. The ability to consistently measure multiple parameters in a new design produces good quality feedback for iterating and honing in on an effective, deployable design. At Berkeley, a diverse optical test stand is utilized to perform beam mapping, band measurements, optical efficiency, and polarization efficiency measurements. For the majority of measurements at Berkeley, a single pixel is used. As such, multiple single-pixel sample holders have been developed.

Optical testing is performed in a, ‘wet’ dewar called 576 (see Figure 4.14). This dewar

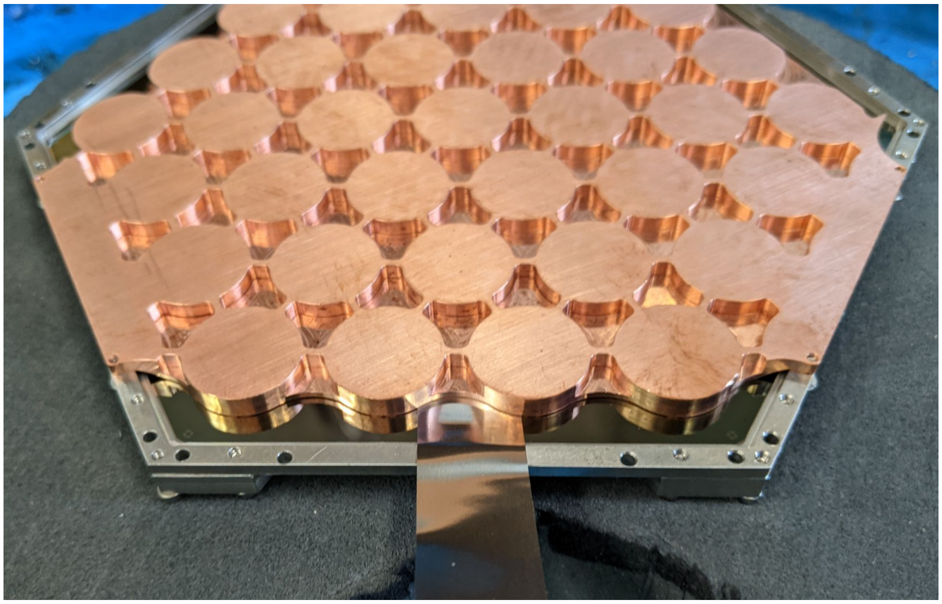

Figure 4.13: A test of an SO-LF backshort after being submerged in liquid nitrogen, with feeler gauges inserted in-between the silicon and the backshort.

utilizes a 77 K liquid nitrogen stage, a 4 K liquid helium stage, and a 250 mK He3 adsorption fridge. The dewar uses multiple metal mesh filters tuned for 90 GHz and 150 GHz testing, as well as a Zotefoam window. A DC SQUID readout system is used to read out the bolometers in each test. It is important to note that the 576 optical test stand is not a perfect reference dewar. The passbands of the filter stack are not perfectly known, and an estimated efficiency of 75% at 90 GHz and 150 GHz is applied to the measurements. Further potential sources of measurement error are discussed in the following sections.

### 4.5.1 Cryo-mechanical testing

Perhaps the simplest of all tests is cryomechanical testing. This must be done for any assembly component that contains an interface of dissimilar materials with mismatched CTEs, including lenslets, invar holders, and backshorts. A couple examples of things that have failed cryomechancial testing and have required iteration are copper wafer holders and epoxy AR coatings on lenslets (discussed further in Chapter 5). For low-risk components, rapid cooling in liquid nitrogen or liquid helium is used. For higher-risk components, such as full-sized lenslet arrays, cryomechanical testing is performed during a cryostat's cooldown, where the rate of temperature change is gradual and allows for a slow cooling of the test piece.

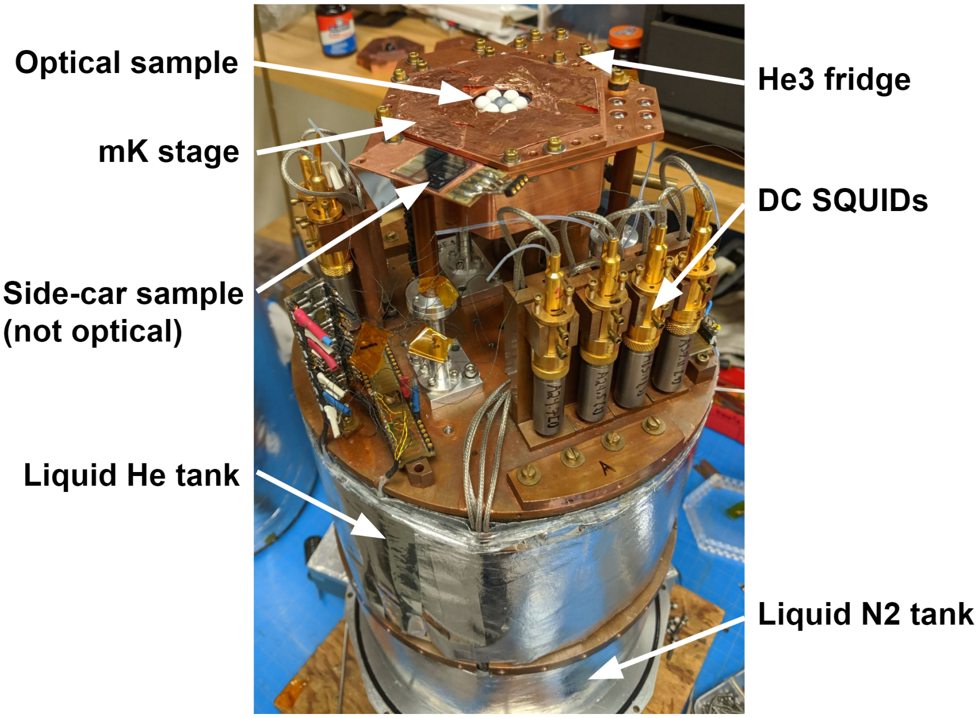

Figure 4.14: The inside of the 576 test dewar

### 4.5.2 Fourier-transform spectroscopy

In a given experiment, the frequency bands to which a telescope or optical cryostat is sensitive are defined by a number of different components. Firstly, the transmission and reflection properties of the window and filters determine the properties of the light that makes it to the focal plane. At Berkeley, optical testing in 576 utilizes four filters designed for use in 90 and 150 GHz, a two-layer teflon filter, and 18, 14, and 12 $cm^{-1}$ metal mesh filters. After the filters, the AR coating on the lenslet and the detector pixel's on-chip microwave filters define the frequencies of light the bolometers will be sensitive to.

To measure the resulting passband, a Fourier transform spectrometer (FTS) is used. Specifically, a Michaelson interferometer with a movable mirror. A basic diagram of this type of FTS is shown in Figure 4.15.

This type of FTS works by passing a signal through a beam splitter, which divides the signal, sending part to the detector and part to a movable mirror. The light coming from the movable mirror again passes through the splitter and makes its way to the detector. This light has temporal coherence with the light coming straight from the source to the detector, which is measured for each step of the mirror. The detector spectral response convolved with the output of the interferometer will give the power spectrum, defined as $S(\tilde{\nu})$ where $\tilde{\nu} = 1/\lambda$ is the wavenumber. The overall intensity seen by the detector $I_{det}(p)$ is a function

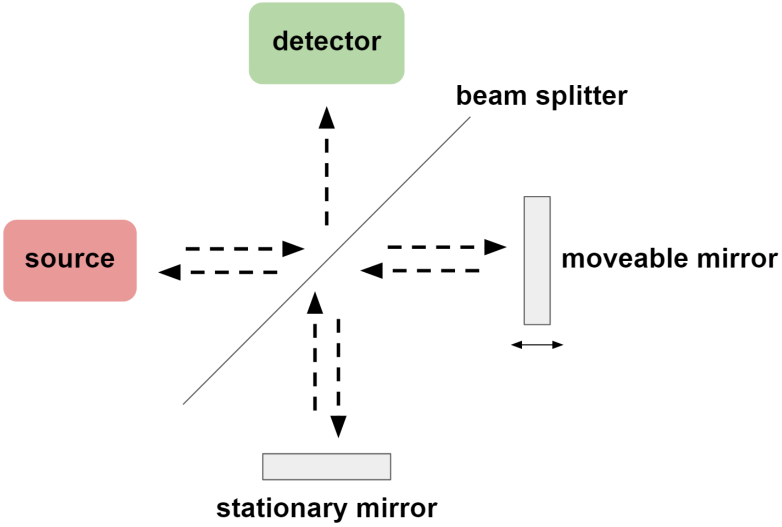

Figure 4.15: Schematic diagram of an FTS utilizing Michaelson interferometer with a moving mirror.

of the path length difference of the moving mirror, p. For a broadband source, this intensity is written as

$$I_{det}(p) = \int_0^\infty S(\tilde{\nu}) \left[1 + cos(2\pi\tilde{\nu}p)\right] d\tilde{\nu}. \tag{4.10}$$

Noting that integrating over $S(\tilde{\nu})$ for all wavenumbers recovers half of the maximum incident intensity (occurring at p = 0). Equation 4.10 can then be rewritten as

$$I_{det}(p) - \frac{1}{2}I_{det}(0) = \int_0^\infty S(\tilde{\nu}) cos(2\pi\tilde{\nu}p) d\tilde{\nu}. \tag{4.11}$$

This integral represents what is called an interferogram, and what is the resultant measurement by the detector from the FTS. To recover the spectrum $S(\tilde{\nu})$, the interferogram is Fourier transformed

$$S(\tilde{\nu}) = \int_0^\infty \left[I_{det}(p) - \frac{1}{2}I_{det}(0)\right] cos(2\pi\tilde{\nu}p) dp. \tag{4.12}$$

An example of a measured interferogram and the resulting spectral response can be seen in Figure 4.16. Experimentally, a higher resolution in p will extend the measurement to higher frequencies, and a larger total range in p will increase frequency resolution in the Fourier transform.

At Berkeley, a ceramic heater is used as a source to create a plane wave which is passed

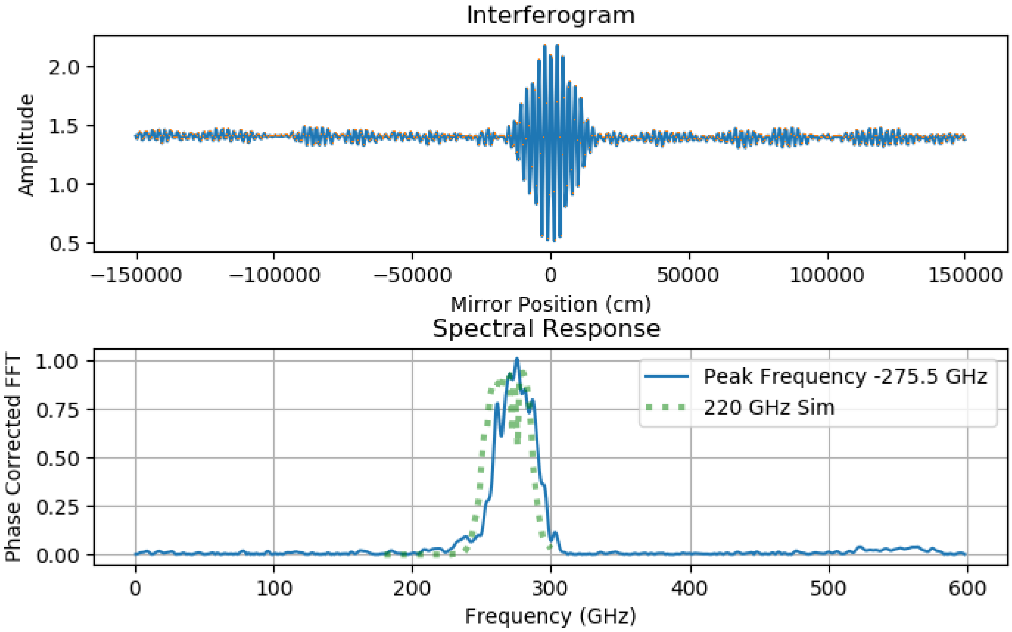

Figure 4.16: Measurement from a prototype 270 GHz pixel with its interferogram (top) and spectral response (bottom). This measurement was performed using the Berkeley FTS.

through a chopper rotating at some frequency that the detector can lock onto via a lock-in amplifier. The chopped signal can then be demodulated. Eccosorb AN-72 is attached to the chopper blades to damp any potential standing waves. The FTS is modeled exactly as shown in 4.15, with the addition of a 45 degree mirror between the chopped source and the beam splitter, and a high-density polyethylene lens between the beam splitter and the dewar.

### 4.5.3 Beam maps

Beam map measurements are made to characterize the response of a pixel as a function of angle. In a reverse-time sense, the beam is the light emitted from an excited antenna that is then lensed through its corresponding lenslet. This is measured by discretely moving an optical source across a grid. In practice, the source is typically a nitrogen source that is ‘chopped’, similar to the FTS source described in the previous section. This allows the detectors to see a signal that is chopped between 77 K and room temperature. Eccosorb is also used on the chopper blades and around the outside of the source to define an aperture and damp potential standing waves. The source is placed on two orthogonal worm-gear drives that define the x-y grid in software. The output signal of the bolometer via the DC SQUID readout is recorded and integrated at each point on the grid. A picture of the Berkeley beam mapper can be seen in 4.17.

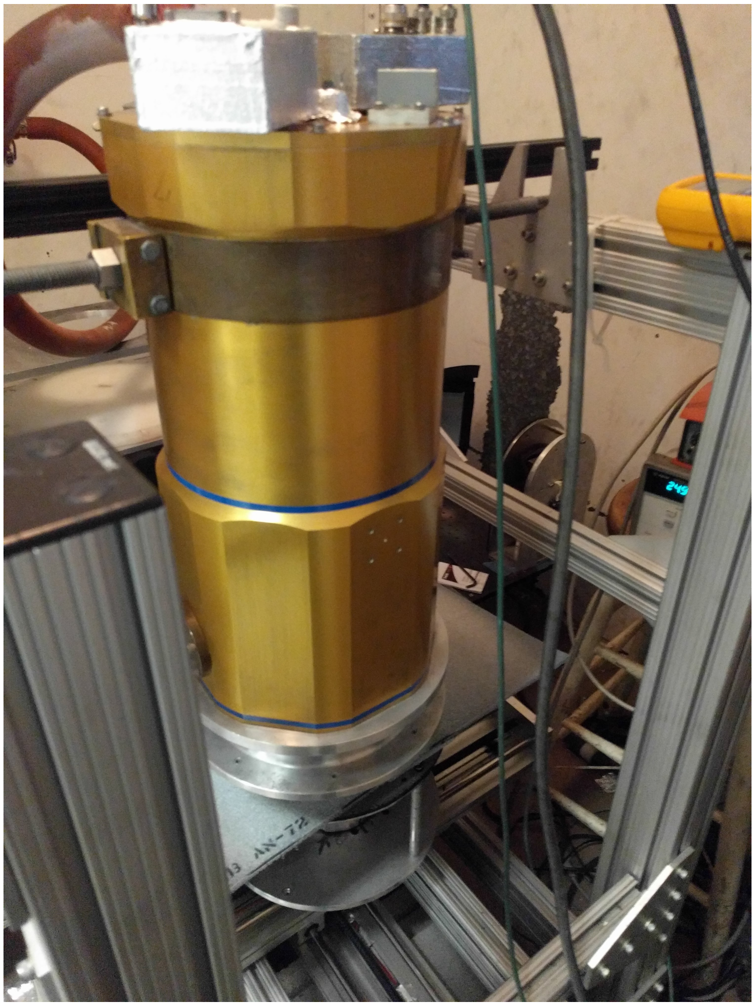

Figure 4.17: A picture of the Berkeley beam mapper designed for use with the 576 dewar.

The resultant beams are typically fit with an elliptical Gaussian function to define the ellipticity of the beam and the location of the beam center; both are used to evaluate the quality of the beam. In practice, beams are not necessarily perfectly Gaussian; however, the center location of the beam can be a quantitative tool to determine the alignment of the AR coating to the lenslet and the alignment of the lenslet to the antenna. Once the beam is fit, looking at its residual by subtracting the fit from the data can be another useful tool to determine any reflections that may be occurring in the system, as well as evaluating non-Gaussianity.

In practice, there are several mechanisms that contribute to potential beam degradation. Assuming that the beam from the antenna is well known, these mechanisms can stem from the lenslets or the test setup itself. Regarding the lenslets, the concentricity of its AR coating

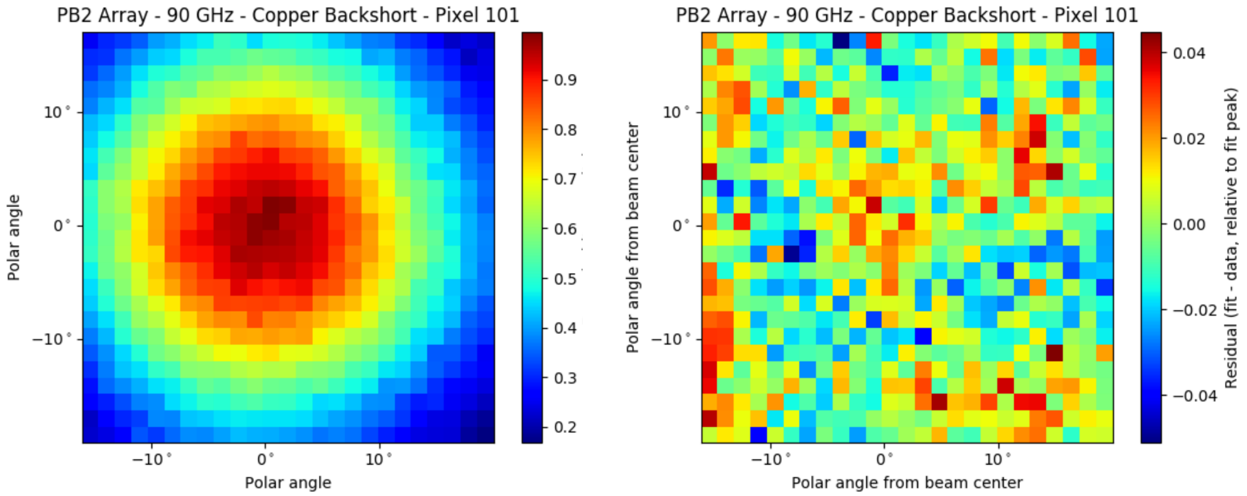

Figure 4.18: A beam map from a 90 GHz pixel taken with the Berkeley beam mapper setup (left) and its residual (fit-data) (right).

and its alignment to the antenna can affect the center of the beam. Taking the whole system into account (from the tip of the lenslet to the source), reflections either off of the inside of the dewar or the outside of the source and x-y stage setup can result in anomalous features appearing as a suppression or enhancement of power in specific locations in the beam maps.

Avoiding reflections from the inside of the cryostat can be done by estimating the divergence angle of the beam and ensuring that there are no reflective surfaces inside of the optical path. This can be done in HFSS, modeling the antenna, frequency, and lenslet. A more basic calculation can be made using the far-field approximation.

$$\theta = \frac{\lambda}{\pi n w_0}, \tag{4.13}$$

where $\lambda$ will be the center frequency of the pixel band, $n$ is the index of refraction of the material through which the beam passes, and $w_0$ is the beam waist. In practice, raising the height of focal plane with respect to the dewar's filters and window has been effective in removing reflections from inside the dewar, typically off of the He3 fridge head and other internal components.

Because the measured beam is a convolution of the pixel's beam and the beam coming from the nitrogen source passing through a defined aperture, reflections in the source's beam will show up in the measured beam as well. These reflections can occur either when the pixel's beam extends outside of the Eccosorb damping surface surrounding the source or when the container holding the nitrogen is exposed and appears in the sources beam. This can happen if either the nitrogen bath is too small and the source beam includes the warm edges of the nitrogen bath, or if too much of the liquid nitrogen boils off, exposing the sides of the nitrogen bath. Many iterations of nitrogen baths were made to converge on a design that was able to hold enough nitrogen reliably throughout the duration of a detailed beam map.

### 4.5.4 Polarization efficiency

A measurement of the polarization efficiency requires a polarized light source for the detectors to look at. This is done by replicating the beam map setup, placing the aperture at the center of the pixel's beam, and placing a wire grid between the nitrogen source's aperture and the dewar. A wire grid is just that, a grid of wires stretched in one direction that are spaced with a pitch smaller than the wavelength of light in question. This wire grid is then attached to a gear that is rotated via a stepper motor. When the detector signal is measured as a function of the angle of the wire grid, ideally the detector will see 100% of light whose polarization is parallel to the corresponding antenna polarization and 0% of the light when the polarization is orthogonal. With a perfectly polarized source and a perfectly polarized detector, the detectors response will go as $cos^2(\phi - \phi_{det})$, where $\phi_{det}$ is the detector polarization angle. This also assumes that no linear polarization is converted into linear or circular polarization via reflection off of components in the test stand, or properties of the lenslet and AR coating.

With these assumptions, the polarization efficiency $\epsilon_{pol}$ can be written as

$$\epsilon_{pol} = 1 - \frac{P_{det}^{\perp}}{P_{det}^{\parallel}}, \tag{4.14}$$

where $P_{det}^{\parallel}$ is the power seen at the detector when the source polarization is parallel to the detector polarization and $P_{det}^{\perp}$ is the power seen at the detector when the source polarization is orthogonal to the detector polarization. Note that $P_{det}^{\perp}/P_{det}^{\parallel}$ is known as the cross-polarization or crosspol. However, the polarization efficiency of the wire grid is not always perfect, and a factor can be included to compensate for a known wire grid polarization efficiency. Additional cross-polarization can occur as a result of polarizing elements in the dewar or lenslet (such as an imperfect substrate or AR coating), as well as from the wobble of the sinuous antenna.

### 4.5.5 Optical efficiency

A detector's optical efficiency is a critical parameter to know when evaluating the efficacy of a given pixel. This value is measured as the efficiency of a system including the cryostat's window, lenses, and filters, the lenslet and lenslet's antireflection coating, and the efficiency of the fabricated components on-chip. The term optical efficiency can be somewhat vague, however, as it can be used to refer to a whole telescope's optical efficiency, or a single pixel's optical efficiency from the tip of the lenslet to the detector, and can include other definitions as well. In this dissertation, optical efficiency will typically be referred to as the total power

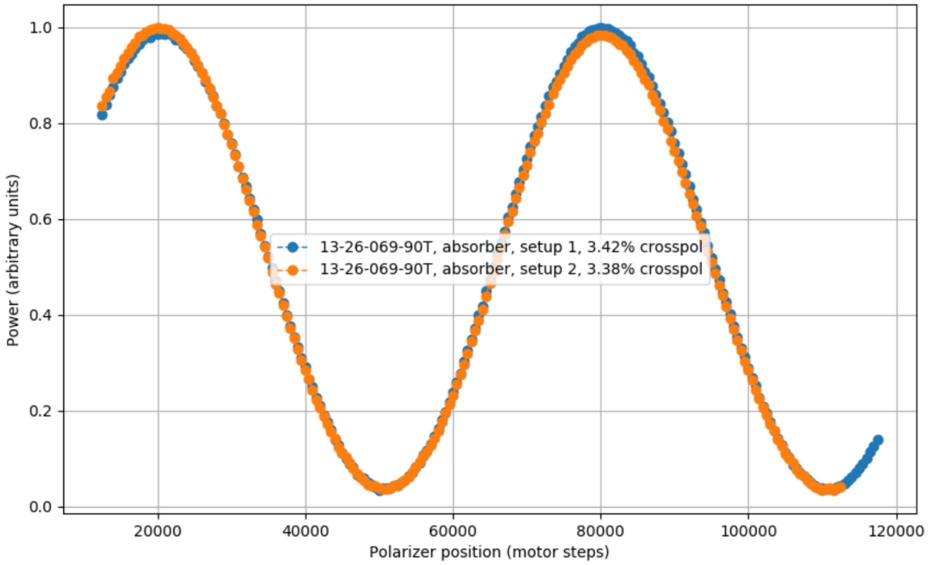

Figure 4.19: A polarization measurement in a 90 GHz detector, showing ≈96.5% polarization efficiency, not including the efficiency of the wire grid. Slightly varying amplitudes can be attributed to non-uniformities in the wire grid.

a detector sees in either a measured band using an FTS or a simulated band from the tip of the lenslet to the detector, relative to the source power. The optical properties of the cryostat are taken into account in the calculations.

The measurement needed to calculate the optical efficiency of a given pixel is a P-R measurement, as shown in the bottom right panel of Figure 4.7. Electrothermal feedback in a TES ensures that its total power dissipated to the bath will always be constant in the transition. Because of this property, one can use 4.2 to see that the optical power measured at the detector will be equal to the electrical power provided by the bias voltage. With a good estimation of the incoming optical power and a measurement of the TES's electrical power over a varied bias voltage, one can calculate an estimated optical efficiency using optical measurements of different blackbody sources. This is done as a differencing measurement, where known-temperature black body beam filling sources are measured at two different temperatures (i.e., liquid nitrogen vs. room temperature), and a difference in electrical power $\Delta P_{elec}$ in the bolometer is also measured for those two temperatures. An example of two P-R curves is shown in Figure 4.20.

Using this $\Delta P$, an integrated measured band, simulated band, or top-hat spectra, optical efficiency can be calculated. Assuming the sources are perfect blackbodies, one can start Planck's radiation formula, writing the average energy in a single mode as

$$\langle E_n \rangle = \frac{h\nu}{e^{h\nu/k_bT} - 1}. \tag{4.15}$$

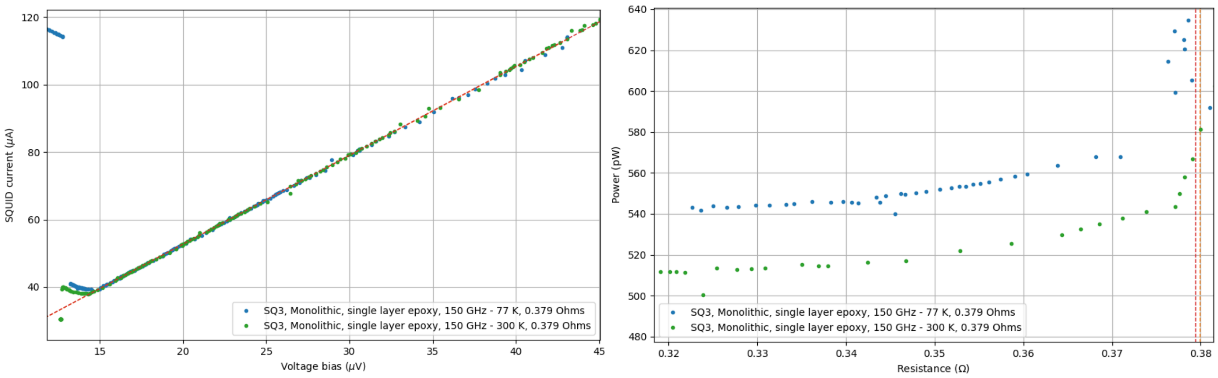

Figure 4.20: IV measurements (left) and corresponding PR curves (right) taken using 77K and 300 K sources with a 150 GHz detector and prototype lenslet.

Then, integrating over frequency, we can write the black body power seen, $P_{bb}$, in a given spectrum $\eta(\nu)$ as

$$P_{bb} = \frac{h\nu}{e^{h\nu/k_bT} - 1}. \tag{4.16}$$

This expression can then be rewritten using the difference in power for a given difference in temperature, and simplified with the assumption that the temperature of both blackbody sources fall within the Rayleigh-Jeans limit

$$\Delta P_{bb} = k_b \Delta T \int_0^\infty \eta(\nu) d\nu. \tag{4.17}$$

The calibrated efficiency in a given band is given by

$$\eta(\nu) = \eta_0 \eta_{meas}(\nu), \tag{4.18}$$

where, $\eta_{meas}(\nu)$ is the measured, uncalibrated spectrum. To write the calibrated efficiency $\eta(\nu)$ in terms of measured values, equation 4.18 can be plugged into equation 4.17 to solve for $\eta_0$. Equation 4.18 is then rewritten as

$$\eta(\nu) = \frac{\Delta P_{bb}}{k_b \Delta T \int_0^\infty \eta_{meas}(\nu) d\nu} \eta_{meas}(\nu). \tag{4.19}$$

Finally, including the dewar's efficiency gives us an expression for optical efficiency,

$$\epsilon_{opt} = \epsilon_{dewar} \eta(\nu) = \epsilon_{dewar} \frac{\Delta P_{bb}}{k_b \Delta T \int_0^\infty \eta_{meas}(\nu) d\nu} \eta_{meas}(\nu). \tag{4.20}$$

Using this equation, the normalized measured spectra can be substituted with simulated or top-hat spectra if desired.

# Chapter 5

# An Overview of Lenslet Technologies

Lenslets have been used in experiments aimed at measuring the polarization of the CMB since the POLARBEAR experiment, which saw first light in January 2012 [39]. A critical component in the optical chain, lenslets help to increase an experiment's optical throughput by providing a high dielectric constant, infinite half-space for a planar antenna to radiate through. To maximize the performance of a lenslet, the correct extension length must be used for a given dielectric and frequency band in question and an effective AR coating must be designed. In addition to achieving sensitivity in a particular bandwidth, the major difficulty of lenslet AR coatings is the differential thermal contraction between the AR coating and the lenslet substrate. Because the dielectric constant of an AR coating is defined to achieve sensitivity in a given frequency band, the materials that can be used are limited.

In this chapter, the functionality of a lenslet's AR coating is discussed, along with different types of AR coatings, including those used in deployed experiments.

## 5.1 Lenslet AR overview

In simple terms, a lenslet's AR coating works to improve the transmission of light over a specified bandwidth, minimizing reflections off of the lenslet surface. This can be achieved using multiple methods, all of which work by modifying the physical or effective dielectric constant at the surface of the lenslet. A single-layer dielectric, multiple-layer dielectrics, or even a metamaterial substrate can be used to create an effective antireflection coating, depending on the application.

An important consideration for a lenslet's AR coating is the thickness of the coating with respect to the lenslet's diameter. Simulations performed by Ariel Cukierman [40] show that for a given pixel diameter, larger silicon lenslets produce larger effective illumination and thinner AR coatings are preferred. In an experiment where the pixel pitch is small, it can sometimes be preferential to use a thinner, single-layer AR coating rather than a thicker, multilayer coating, where the lensing of the beam predominately happens in the high dielectric constant silicon, rather than a lower dielectric constant AR material. This puts a limit on the number of layers that are optimal for a given lenslet's AR coating.

### 5.1.1 Single-layer coatings

The simplest AR coating is a single-frequency single-layer AR coating. This is known as a $\lambda/4$ AR coating. Here, the coating is designed such that its dielectric constant is $\epsilon_{AR} = \sqrt{\epsilon_{lenslet}}$. The thickness of the coating then must be $d_{AR} = \lambda/4$, where $\lambda$ is the desired wavelength inside the AR layer.

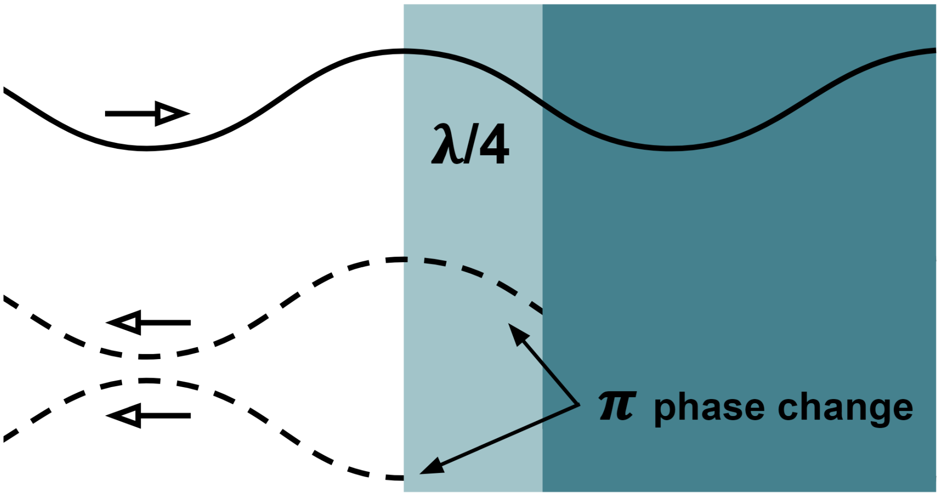

Figure 5.1: Destructive interference between waves reflected off of a substrate surface and a single layer $\lambda/4$ AR coating.

In this configuration, the incident wavefront's reflection off of the AR coating destructively interferes with the wavefront coming off of the lenslet's surface, canceling reflection for a given frequency. Although this type of AR is designed to work for a single frequency, Figure 5.2 shows how it is possible to achieve higher optical throughput for a range of frequencies around the designed center frequency.

### 5.1.2 Multi-layer coatings

Utilized by the Simons Array and SPT-3G telescopes, multilayer coatings on lenslets have been proven to be effective over wide bandwidths [41]. Multilayer coatings are designed to gradually change the index of refraction from free space to the lenslet substrate material to minimize reflection. Typically, with more layers a wider bandwidth can be achieved; however, transmission can be degraded if the AR coating is too thick (see Figure 5.3).

A simple and effective means of designing a multilayer coating is to design multiple stacked $\lambda/4$ AR coatings using indexes of refraction that taper from free space to the lenslet

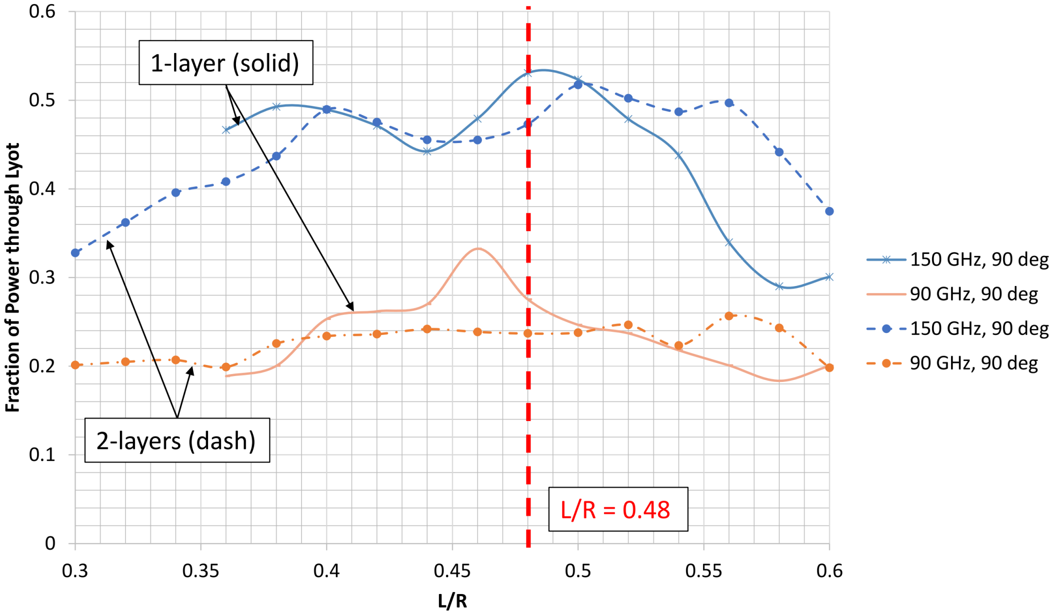

Figure 5.2: An HFSS simulation done by Aritoki Suzuki showing the fraction of power through a telescope's Lyot stop as a function of a lenslets L/R ratio. These simulations were done using double slot dipole antennas at 90 and 150 GHz, comparing single and double layer AR coatings for 5.6 mm diameter silicon lenslets. Though there is some variation, this plot shows how a single layer coatings can achieve higher optical throughput for a relatively small pixel size.

substrate [43]. Typically, the frequency used to design the AR coating is the geometric mean of the center frequencies for two or more bands.

In practice, multilayer coatings can be challenging to implement, since multiple interfaces with multiple different CTE values must be taken into account. Additionally, a thicker AR coating means that the force from thermal contraction at the silicon surface will be greater. A greater force from thermal contractions can lead to delamination of the coating from the lenslet substrate and, in some cases, destruction of the substrate itself. Sourcing materials with exactly the correct indexes required can be difficult as well, potentially limiting the design of the AR coating.

### 5.1.3 Metamaterial AR

Metamaterial, or, sub-wavelength structure (SWS) AR is not actually a coating and is often referred to as a 'structure' or 'surface'. A metamaterial AR surface works by transforming the surface of the substrate to modify its effective index of refraction as a function of depth in the material. This can typically be done by cutting grooves in the substrate surface with dicing saws [44], or by creating what is called a moth-eye or inverse moth-eye coating [45] (see Figure 5.4). Both implementations can use either stepped designs or continuous gradient designs. A stepped design mimics a multilayer coating, where each step represents

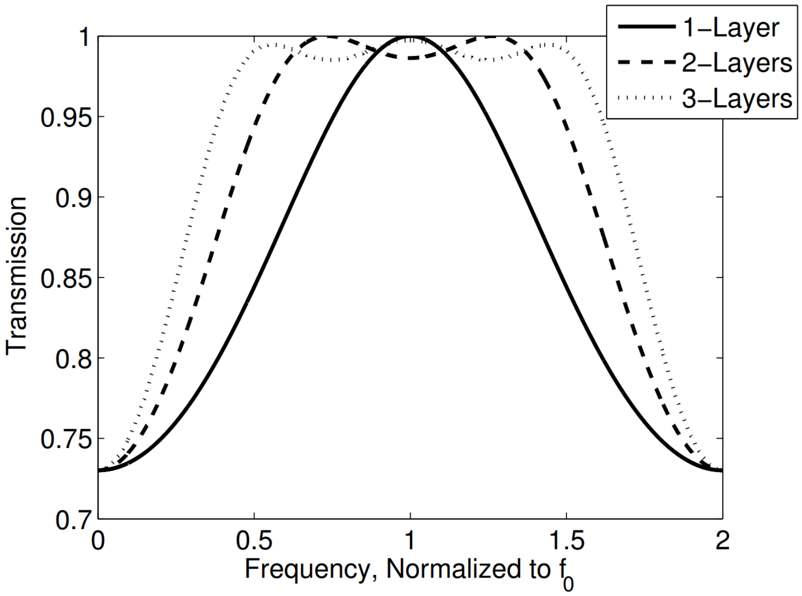

Figure 5.3: Frequency normalized transmission for one, two, and three layer $\lambda/4$ AR coatings on alumina [42].

an individual effective index. This can be seen in Figure 5.4. A gradient design tapers smoothly from the top to the bottom of the structure. Typically, a gradient metamaterial AR is capable of achieving a wider bandwidth and higher sensitivity at oblique angles of incidence [46], however, in practice, adequate bandwidth and transmission characteristics can likely be achieved for a given application in both styles [47, 48], and ultimately the chosen fabrication process will determine whether a metamaterial structure is stepped or tapered. Preliminary simulations of metamaterial AR structures for LiteBIRD lenslets have confirmed this, where a stepped design typically shows ∼99% average in-band transmission, a gradient design with the same band center will achieve ∼98% transmission over a larger bandwidth.

A metamaterial AR structure is most often fabricated by using a dicing saw, laser system, micromachining, or electrical discharge machining (EDM).

Another metamaterial technology that is being developed as a replacement for a traditional hemispherical lenslet is known as a planar phase-engineered metamaterial lenslet. These lenslets utilize multiple thin film layers stacked on top of each other, designed to manipulate an antenna's field, mimicking a lens. This works by applying thin metal films in succession designed to radially decharacterize the phase delay of an incoming plane wave so that the outgoing phase pattern matches the chosen feed [49].

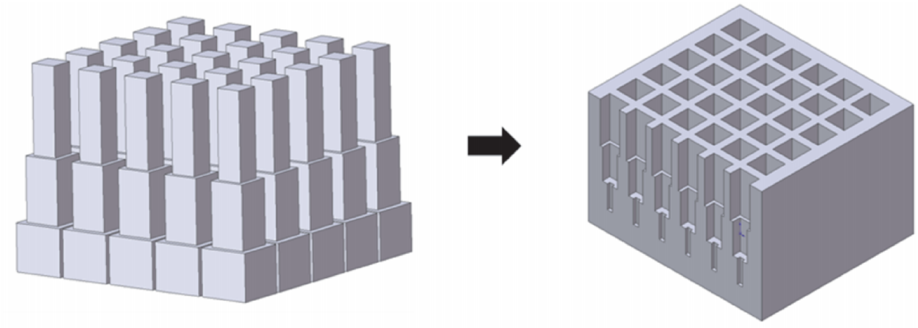

Figure 5.4: An example of a moth-eye structure (left) and an inverse moth-eye structure (right) [45].

## 5.2 Deployed lenslets

Three ground-based CMB experiments have deployed planar antenna-coupled hemispherical lenslets, POLARBEAR, Simons Array (PB-2a and PB-2b), and SPT-3G. This section will outline the technologies used in each of these experiments, including their successes and pitfalls.

### 5.2.1 POLARBEAR lenslets

POLARBEAR used a double-slot dipole antenna designed for 150 GHz measurements. To couple to this antenna, a lenslet size of 6.35 mm was chosen. A single layer of thermoformed PEI plastic was used for an AR coating, which showed high transmittance in the target band, near 100% in a flat sample prepared with an equivalent AR coating [50].

The first prototype lenslet arrays for POLARBEAR used an alumina lenslet substrate on a silicon extension wafer. The advantage of using alumina over silicon is that alumina spheres are more readily commercially available at certain diameters, as they are used as ceramic ball bearings that can then be cut in half to make a lenslet. The experiment eventually switched to silicon hemispheres, which offer slightly higher optical throughput as a result of their higher dielectric constant. These were manufactured by grinding silicon down into a sphere and then cutting the sphere in half. However, the process is much more costly, as they must be custom made in smaller batches than the commercially available alumina spheres.

POLARBEAR deployed a single alumina lenslet array and six silicon lenslet arrays, all with PEI plastic thermoformed AR coatings, manufactured by Welch Fluorocarbon.

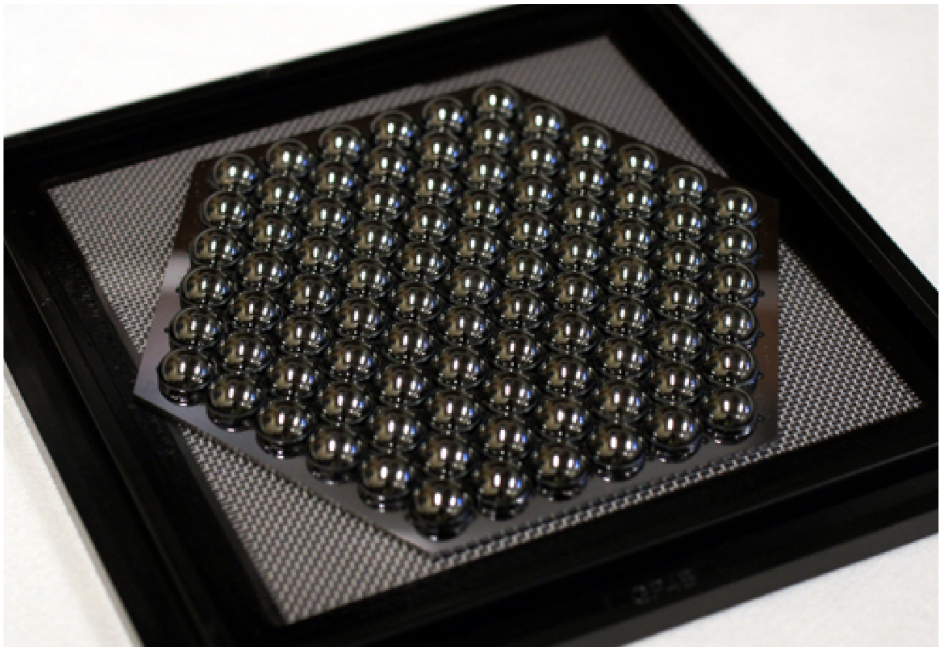

Figure 5.5: Picture of a POLARBEAR silicon lenslet array with PEI plastic AR coating. [50].

### 5.2.2 PB-2a/b lenslets

Building off POLARBEAR's success, Simons Array similarly uses planar antenna-coupled lenslets. However, one of the major advancements for Simons Array was switching from a single-frequency double-slot dipole antenna to a dichroic sinuous antenna, looking at two polarizations of 90 and 150 GHz simultaneously. The dichroic pixel provided a substantial increase in sensitivity, but required a more complex lenslet design with an AR coating effective in both 90 and 150 GHz bands.

POLARBEAR-2a and b telescopes use the same silicon lenslet with a broadband two-layer AR coating. A two-layer AR coating design was chosen for the dichroic pixel to have an adequate balance of transmission and bandwidth properties for PB2's 90 and 150 bands when compared with a single-layer or three-layer design.

Rather than using plastic, PB2-a and b use epoxy-based AR coatings. The epoxies used for the AR coating were Stycast 2850 and Stycast 1090. Developed as circuit board potting epoxies, these epoxies have been adopted in CMB experiments to be used as AR coatings due to their relatively low CTEs and indexes of refraction that are near perfect for $\lambda/4$ AR coatings on high dielectric substrates.

Using a flat alumina sample, near perfect transmittance was achieved with this AR coating [42], as shown in Figure 5.7.

These lenslets were manufactured using an epoxy molding process, where each lenslet was placed in a mold designed for the epoxy thickness required in each layer. The Simons Array

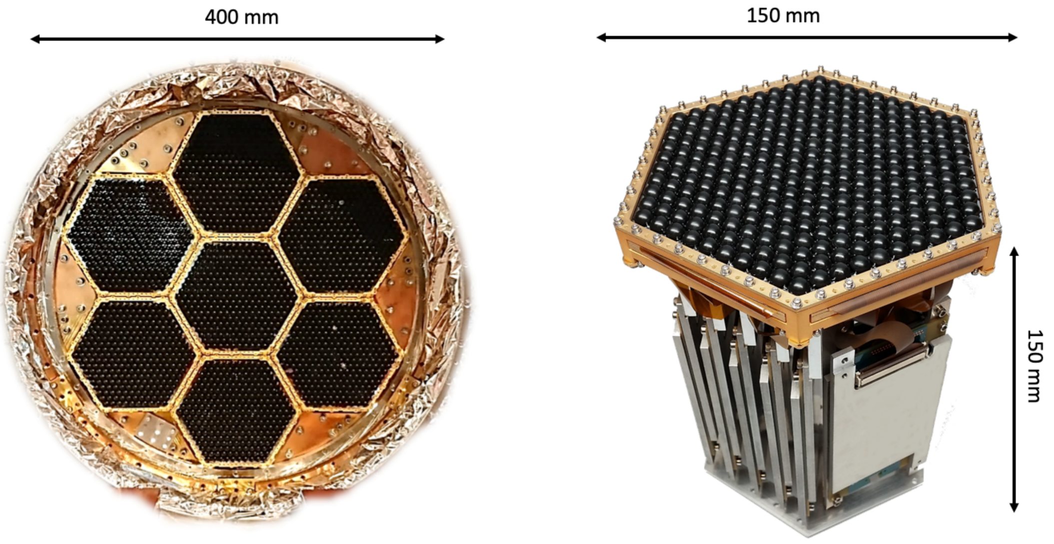

Figure 5.6: The PB-2a focal plane (left) and a PB-2a detector/readout assembly. Note the few light spots on the PB-2a focal plane (left), being delaminated AR coatings from prior cryo-mechanical testing.

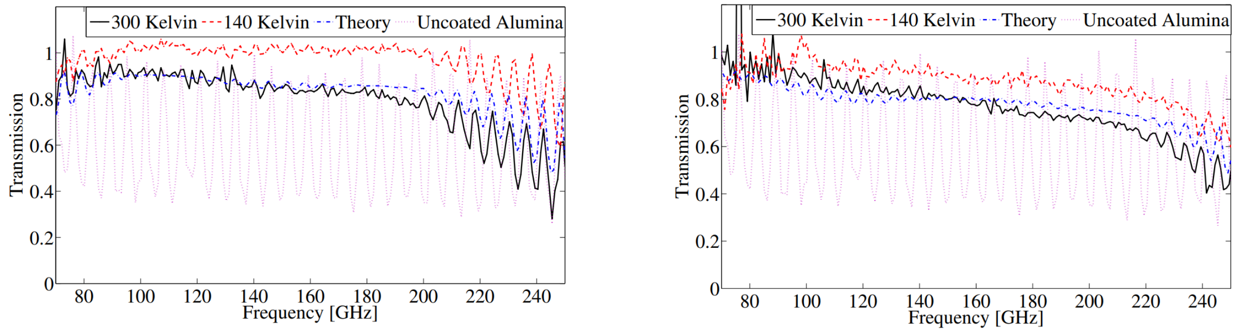

Figure 5.7: Transmission measurements of the PB-2a/b lenslet AR coating on a flat, alumina sample. [42].

telescopes pushed the mass manufacturing capabilities of this technique, as each telescope uses seven arrays, each with 271 individual pixels. This means that ≈3,800 lenslets had to be manufactured in total, each individually molded twice, once for each AR layer. This processes was improved upon during R&D for PB-2c lenslets, as discussed in the next chapter.

Aside from being time-consuming to manufacture in large quantities, another downfall of the multilayer epoxy lenslets is potential delamination. Although the vast majority of lenslets survive, it is typical for anywhere between one and a few AR coatings per array to delaminate while cooling inside of the cryostat (see Figure 5.6. Although this is not a substantial decrease in yield for the Simons Array telescopes, for a space mission such as

LiteBIRD, far fewer pixels will be used and delamination for even a single pixel is considered unacceptable.

### 5.2.3 SPT-3G lenslets

the SPT-3G telescope uses trichroic pixels centered around 95, 150, and 220 GHz. With a third band on each pixel, an AR coating with high transmission over a larger overall bandwidth was desired.

To accomplish this, a three-layer thermoformed plastic AR coating was used on top of 5 mm diameter alumina lenslets. From bottom to top, the plastics used were RO3006, RO3035, and Porex PM-23J [41]. Plastic sheets were thermoformed over fully populated lenslet arrays, and then the plastics were laser diced. The laser dicing step was crucial in this process, as delamination of the coating would affect all lenslets in an array otherwise. These arrays can be seen in figure 5.8.

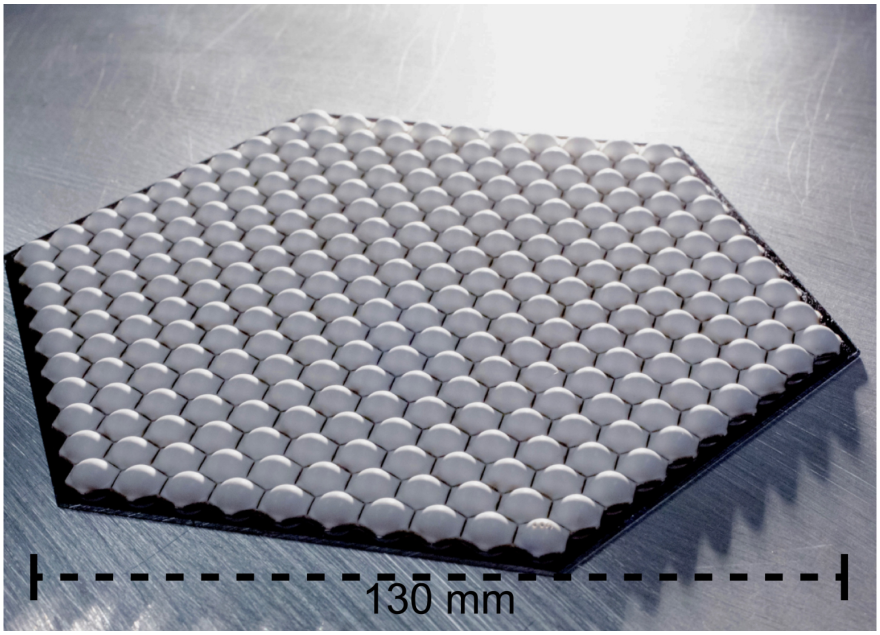

Figure 5.8: A completed SPT lenslet array with three-layer thermoformed plastic AR coating and 5 mm diameter alumina lenslets. [41].

Measured on an alumina puck with the Berkeley FTS, the coatings were shown to achieve transmission nearly identical to the modeled transmission, being near 100% for the 95 and 150 GHz bands and ≈85% in the 220 GHz band. The lenslet and pixel together achieved commendable band-averaged efficiencies of 0.81, 0.83, and 0.73 for the 95, 150, and 220 GHz bands, respectively, over the expected passbands [51].

### 5.2.4 Glass AR lenslets for SO-LF

The Simons Observatory low-frequency lenslets edge themselves into this section. At the time this thesis was published, they have not yet been deployed, but they are set to deploy in the SO LATR in February 2024.

SO-LF arrays are the only lenslet coupled sinuous antenna arrays in Simons Observatory and will observe with bands centered at 30 and 40 GHz, designed for characterizing polarization in galactic synchrotron radiation. A relatively narrow bandwidth requirement means that a single-layer AR coating can be used. Because these pixels will observe at much longer wavelengths than the science bands 90 and 150 GHz, the pixel must be scaled in size to accommodate. Therefore, a larger lenslet and AR coating are required, leading to a number of new challenges that will be discussed in the next chapter.

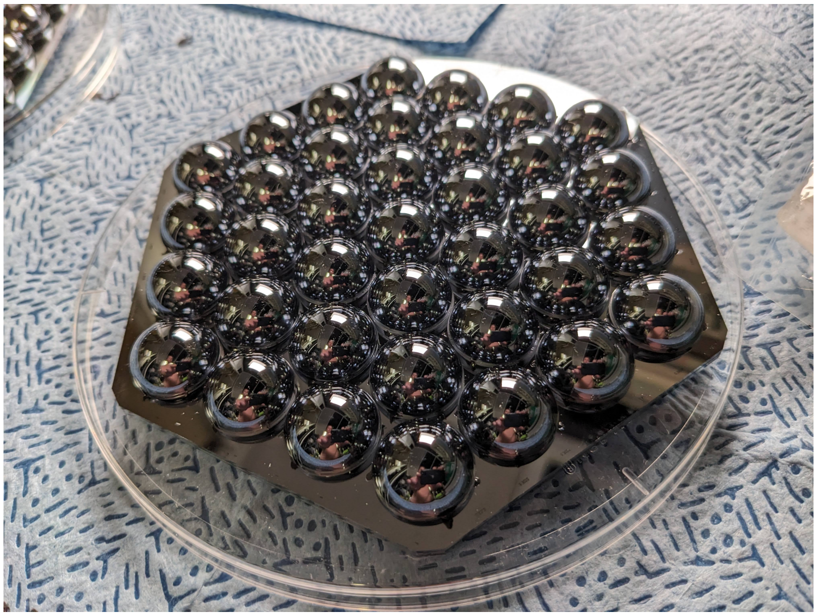

Figure 5.9: A fully populated SO-LF lenslet array.

The fabrication of these lenslets is outsourced to a company called Hyperion Optics. Hyperion Optics is responsible for sourcing the silicon and adhering an AR coating onto them. Borosilicate glass has a nearly perfect index of refraction for a single layer $\lambda/4$ AR coating on silicon. This is advantageous, as borosilicate glass has a CTE of $\sim$3.3 $\times 10^{-6} K^{-1}$, very closely matching the CTE of silicon of $\sim 2.5 \times 10^{-6} K^{-1}$. As a result, the borosilicate AR coating has proven to be robust to cryomechanical testing, despite having to be much thicker than previously deployed AR coatings.

More information on the glass SO LF AR coatings will be discussed in the next chapter.

# Chapter 6

# Lenslet Research & Development at Berkeley

Deployed lenslet technologies, though proven to be functional, are not all perfect and have a number of areas that can be improved upon. With new experiments pushing to deploy more and more detectors to increase their sensitivity to increase the probability of measuring the primordial B-mode signal, the scalability of certain lenslet technologies has become an issue. Not only does an increased pixel count present a fabrication problem, but the overall increased number of experiments means that there are fewer person-hours to dedicate to things like a mass fabrication and epoxy coating of thousands of lenslets. Scalability aside, SO-LF and PB-2c lenslets both required sensitivity to frequencies that had not been observed using lenslets before and required new R&D to prove their efficacy. Being a space-based mission, LiteBIRD presents additional unique requirements. The lenslets and lenslet arrays must be guaranteed to survive bother vibration tests and launch, as well as multiple thermal cycles.

This chapter will overview the R&D pursued at Berkeley with regard to new lenslet technologies and fabrication techniques. A significant fraction of the work done for this dissertation involved new lenslet R&D for upcoming experiments, most of which were successful, some of which were not, and some of which are still in progress. Details of all the accomplishments and issues encountered are given in the following sections.

## 6.1 Molded epoxy lenslets

Following the deployment of PB-2a and PB-2b, the PB-2c telescope was originally designated to characterize cosmic dust polarization with measurements at 220 and 270 GHz. Although the 220 and 270 GHz program was canceled in 2020, PB-2c high-frequency lenslet R&D proved to be a successful improvement for epoxy-molded lenslet technology.

For future CMB experiments with substantially higher pixel counts, the PB-2a and PB-2b methods of single-pixel molding present scalability issues. If epoxy AR technology were to move forward for the next generation of CMB telescopes, a more efficient fabrication process would need to be developed. The research program for the PB-2c lenslets was focused on solving this issue, molding entire arrays at once, rather than individual pixels. These lenslets would be 6.35 mm in diameter and would utilize an alumina substrate with a single-layer Stycast 1266 AR coating centered around 245 GHz.

### 6.1.1 Mechanical implementation

Whole-array molding presented a number of new engineering challenges to overcome. Primarily, the mold would need to achieve a total offset of less than 10 microns between the coating and the lenslet (given from the simulations shown in Figure 4.9), across an entire array of pixels. Another big challenge was releasing the array from the molds. A large surface area of epoxy would touch the mold, and a thin, 675 $\mu m$ thick silicon lenslet array can be easily damaged upon release.

#### Mold materials

To maximize the chance of a successful release, a slippery plastic would be used for the mold surface. In first attempts, raw PTFE was used. Although this material is slippery and had a high probability of successful release, it was found that on a time scale of weeks to months, PTFE would absorb enough water to increase the maximum offset of AR coating given by the mold by more than 50 $\mu m$.

To fix this, a material called Rulon J was used. This material is a glass-fiber-infused PTFE, which retains the low-friction characteristics of raw PTFE with increased stability and machinability. To ensure a successful release, a thin layer of aerosolized mold-release was also applied to the mold. An aluminum substructure was added to the design in order to minimize the dimensional changes due to temperature and water absorption. Both pieces are keyed together via repeating interlocking features. A detailed design of the mold structure and the molding surface is shown in Figures 6.1 and 6.2, respectively.

#### Silicon lenslet seating wafer

An accompanying, 675 $\mu m$ thick silicon lenslet seating wafer was designed and incorporated features for mold alignment, lenslet gluing, and more. The features of the seating wafer are shown in Figure 6.3. The aluminum mold substructure, the Rulon mold, and the seating wafer are aligned together using three alignment pins around the outside edge of the wafer. The Rulon mold also contains ‘bosses’ between each grouping of three pixels that mate into etched pockets on the seating wafer, showing in ‘6’ in Figure 6.3 on the silicon, and ‘5’ on the mold face in Figure 6.2. This ensured that the parts would mate properly.

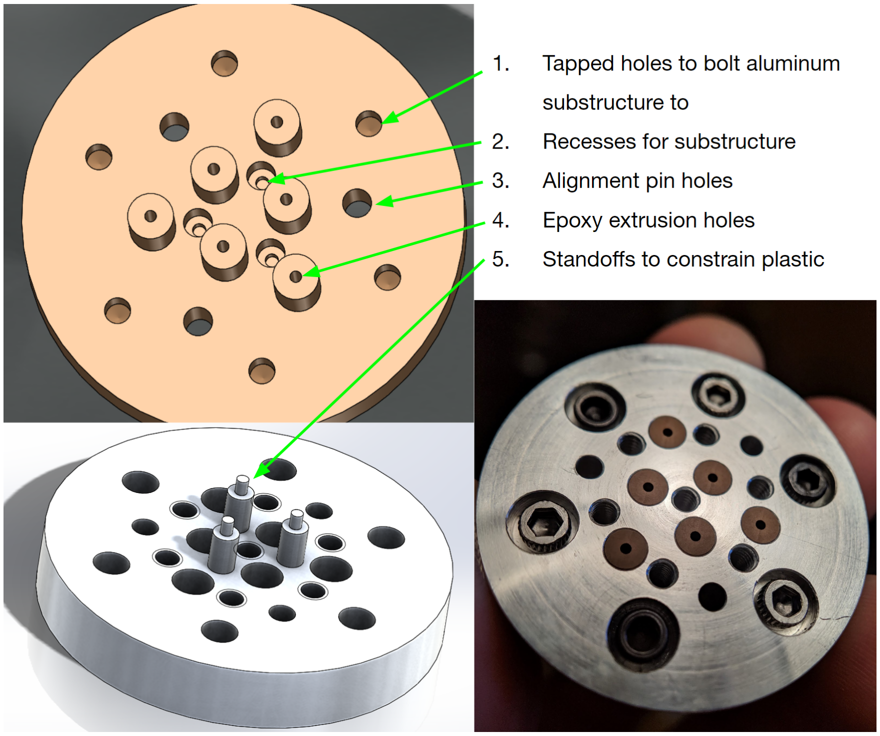

Figure 6.1: An overview of the features in a scaled down, 7-pixel version of the PB-2c lenslet mold structure.

### Releasing features

Releasing the arrays is done via ∼20, 000-120 screws. Threads were tapped into the aluminum stand-offs (‘5’ in Figure 6.1). The through holes were machined into these locations of the standoff pockets in the Rulon mold. These screws penetrate through the mold and press against the silicon seating wafer to release the molded array. A small space was left between the screw and the silicon surface during molding, so that a barrier of epoxy was created between the silicon and the screw. This was done to minimize the risk of the silicon cracking during release. These features can be seen in Figure 6.4.

## 6.1.2 Assembling and molding the arrays

The first step in assembly is to attach the alumina hemispheres to the fabricated silicon seating wafers. These hemispheres were purchased as 1/4 inch diameter ceramic ball bearings that were then ground in half to a height tolerance of 5 $\mu m$. To attach the hemispheres to the seating wafer, each of the 271 hemispheres were placed into their pockets on the seating wafer. A seating wafer press jig shown in Figure 6.5 was then used to hold the lenslets in place while being epoxied. This seating press was a critical step as the small hemispheres

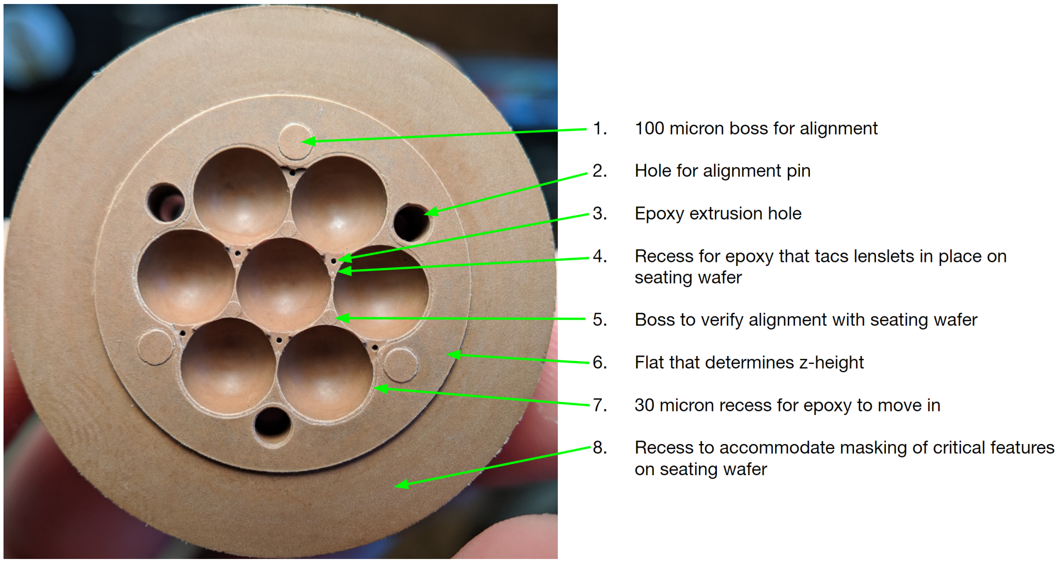

Figure 6.2: An overview of the features in a scaled down, 7-pixel version of the PB-2c lenslet mold's molding face.

could easily slip out of their pockets during epoxy application. The press was coated with silicone on the bottom side to make sure that the aluminum press did not directly contact the alumina hemispheres. After verifying that all 271 hemispheres were correctly seated, a pressurized fluid dispenser is used to extrude an exact amount of Stycast 2850 epoxy through a luer lock syringe for each epoxy point. After a 24 hour cure, the array is ready to be placed in the mold.

To prepare the mold, a thin layer of mold release is sprayed onto the Rulon. The 000-120 release screws are then inserted into the mold. Next, an approximate volume of Stycast 1266 is dispensed into each pocket of the mold using a syringe. Alignment pins are inserted into the mold, and the uncoated lenslet array is placed onto these pins, keyed in with its etched features. The array is pressed down into the mold, as the alignment pins are allowed to be pushed through the other side of the mold. A press is then used to apply an even force across the back of the array as the epoxy cures. The excess epoxy is extruded through the features shown in '4' in Figure 6.1, and the unetched silicon faces on the array are pressed against the flat part of the mold, shown in '6' in Figure 6.2 to define the z-height of the coating.

After the epoxy is allowed to cure for 24 hours, the mold and lenslet array are removed from the press. To release the array from the mold, 000-120 screws are progressively screwed into the aluminum substructure. They are turned 1/4 turn at a time in a specific order until the array can be removed by hand. This step takes time and is perhaps the most tedious step of the entire process but is critical to releasing the array intact.

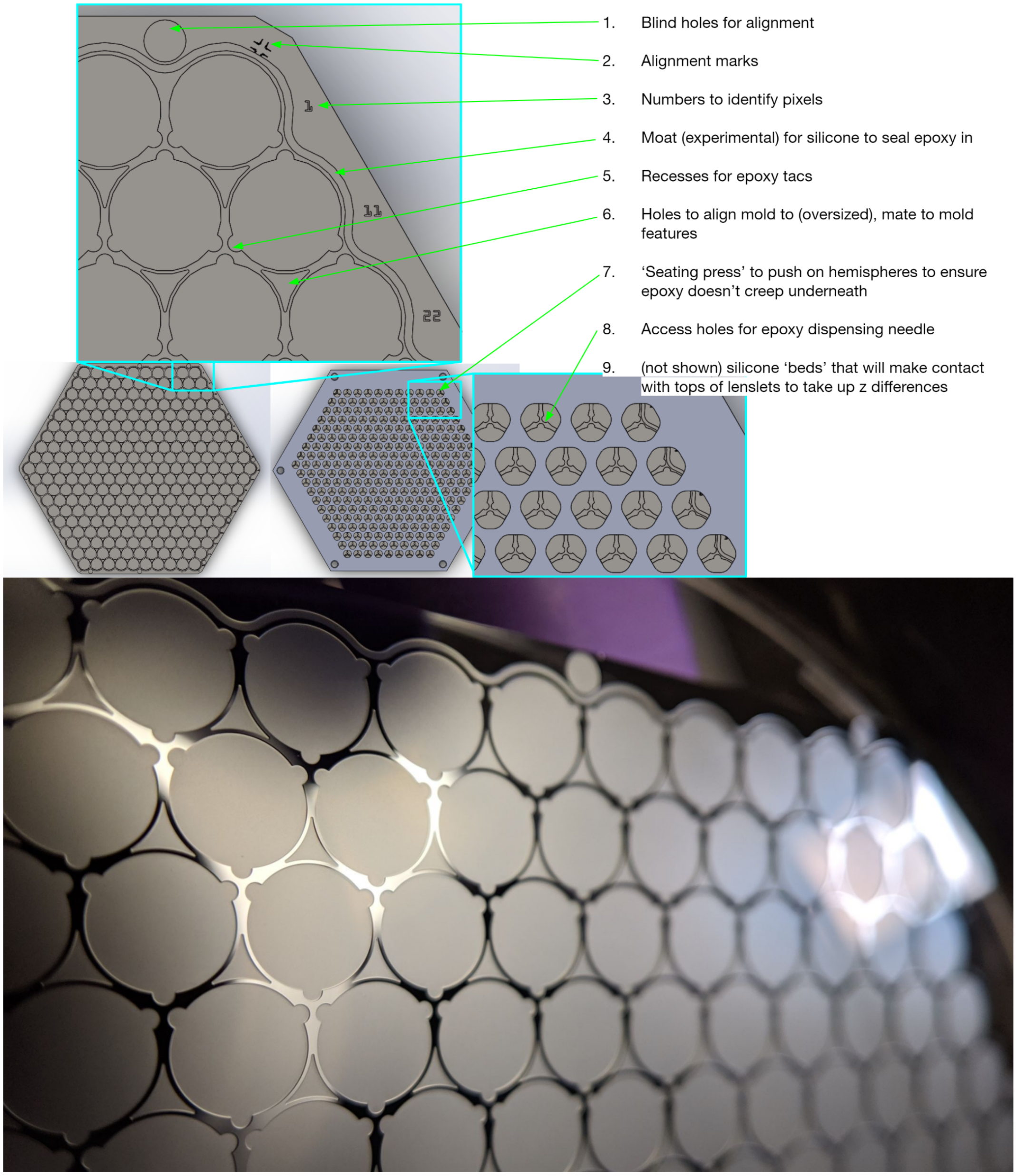

Figure 6.3: (Top) An overview of the PB-2c lenslet seating-wafer design. This also shows the ‘seating press’, used when hemispheres are glued into place onto the seating wafer. (Bottom) A picture of the fabricated seating wafer.

### 6.1.3 Mechanical evaluation

Once the array is molded, metrology is performed to ensure that tolerances for the AR coating were achieved. Although the z-height of the array can be measured before and after

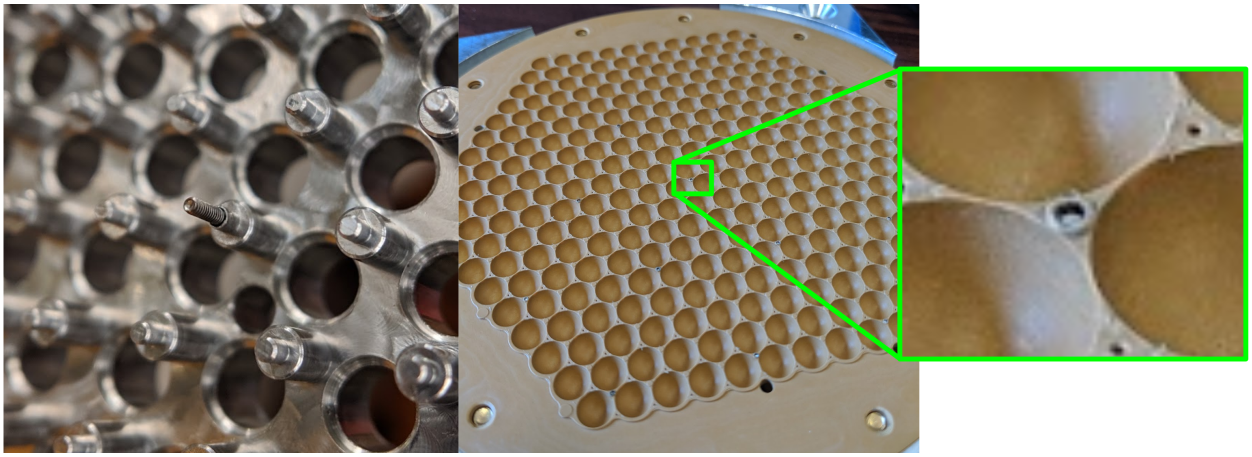

Figure 6.4: The aluminum sub-structure is show on the left with a 000-120 release screw showing protruding from its tapped hole. On the right, the Rulon mold is shown, indicating the location of a 000-120 release screw.

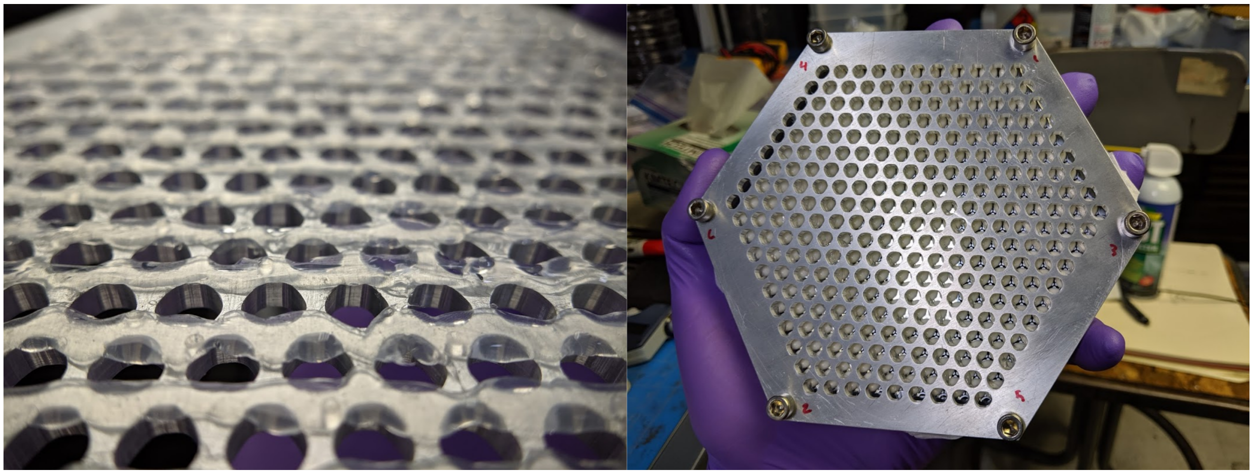

Figure 6.5: Picture of the lenslet-side of the seating wafer press (left) and the assembled seating wafer press jig (right).

molding, the x-y displacement in the plane of the array of the AR coating is difficult to evaluate. This was measured on an array that had failed the release process, because the bottom side of the molded lenslets could be observed in fractured parts of the silicon seating wafer. Lenslets were chosen from different locations throughout the array, and a 'smart scope' was used to evaluate concentricity. The useful feature of the smart scope is that it can define a coordinate system so that digital measurements can be made. It was found that an overall coating concentricity of $< 7\ \mu m$ was achieved in all the measured pixels.

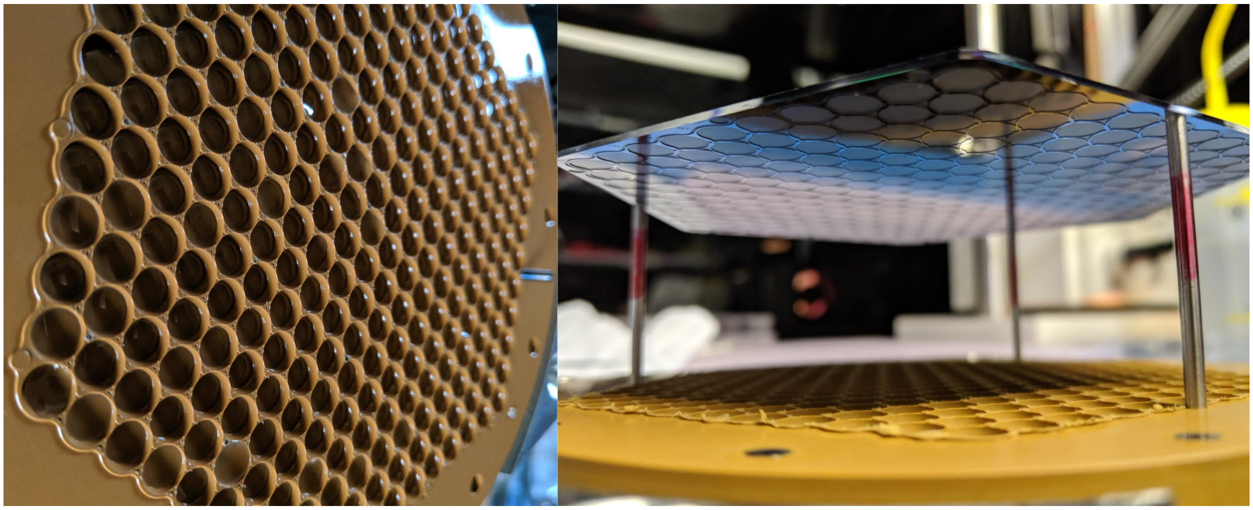

Figure 6.6: Picture of the prepped mold with epoxy applied (left), and a silicon seating wafer keyed into the alignment pins inserted into the mold (right).

This falls within the 10 $\mu m$ requirement and was considered successful. It is important to note that the temperature is monitored during every step of this process and was recorded to be within 5 degrees Fahrenheit of the temperature at which the mold was machined. A defect that occurred in the arrays was air pockets in $\sim$5% of pixels per array. Unfortunately, this issue was not addressed, as the 220-270 GHz program for PB-2c was canceled before troubleshooting could occur.

Credit should be given to the UC Berkeley Physics Machine shop for machining these parts to such incredible tolerances. The success of the mold would not have been possible without their efforts to ensure that each part was machined as close to the defined dimensions as possible.

### 6.1.4 Optical evaluation

To measure the effectiveness of the molded AR coatings, a mold with identical features was created for small test arrays of 7 pixels. These test arrays were aligned to prototype 220/270 GHz pixels using the 'smart-scope' to a $\pm 5 \mu m$ accuracy. Measurements were then taken using the 576 test stand. Measurements included beam maps and measurements of the power spectrum (shown in Figure 6.8, as well as measurements of polarization efficiency and optical efficiency (shown in Table 6.1.4.

The resulting beam maps showed low ellipticity, indicating a concentric AR coating and good lenslet-pixel alignment. For a reference point, measurements of the same pixel and detectors were taken using a 12.7 mm diameter, single-layer plastic coated alumina lenslet, with the coating centered at 245 GHz. When the spectra are peak normalized, reference

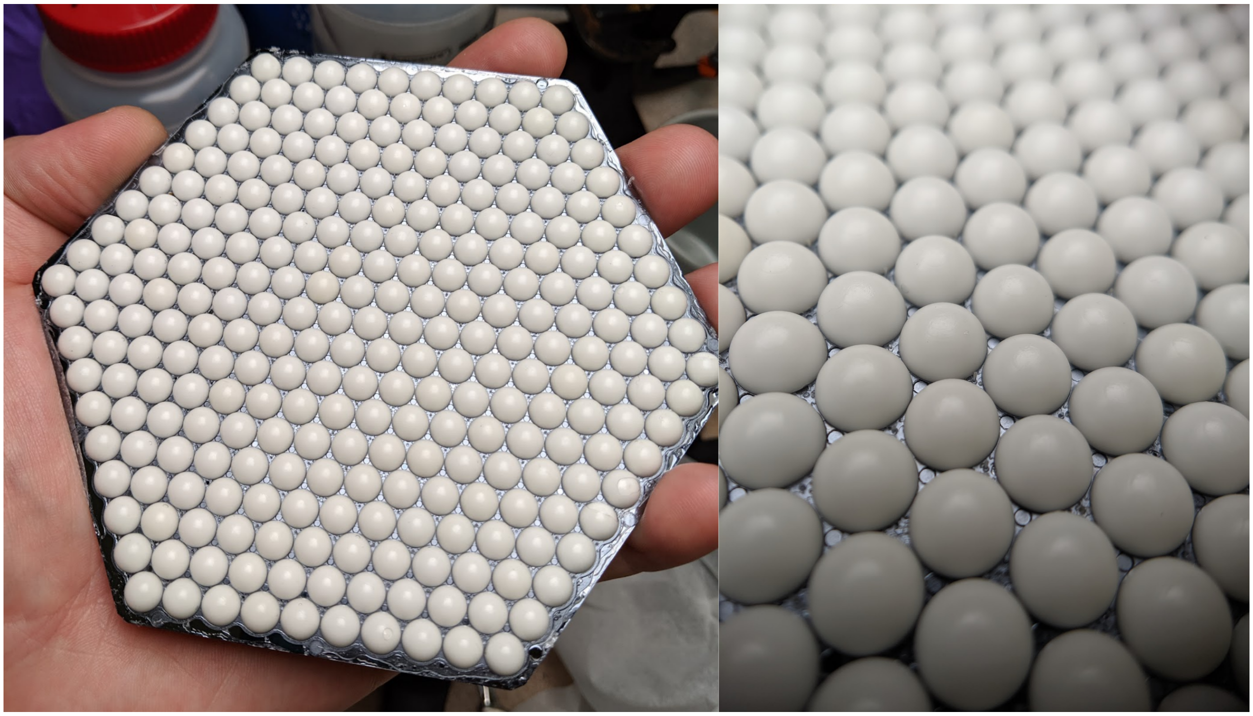

Figure 6.7: Pictures of a completed PB-2c, 220-270 GHz lenslet array.

Table 6.1: Molded epoxy AR and plastic AR, 220/270 GHz optical efficiency and crosspol measurements

| | Optical efficiency 220 GHz | Optical efficiency 270 GHz | Crosspol 220 GHz | Crosspol 270 GHz |
|---|---|---|---|---|
| Plastic AR (12.7 mm) | 35% | 43% | 3.7% | 4.2% |
| Epoxy AR (6.35 mm) | 34% | 27% | 2.9% | 3.6% |

The above measurements were made using the same on-chip pixel and detectors. The plastic AR lenslet is a 12.7 mm, alumina hemisphere with a 245 GHz centered, single-layer plastic AR coating. The molded epoxy AR lenslet is a 6.35 mm silicon hemisphere, molded with a single-layer Stycast 1266 AR coating, centered at 245 GHz. Optical efficiency calculations were done using simulated spectra and not the measured spectra. Dewar window and filter loss is estimated to be 75%. Note that the effect of the truncated spectra from Figure 6.8 results in relatively lower optical efficiency in the epoxy AR coated lenslet's 270 GHz channel.

spectra measurement shown in 6.8 reveal slightly more power going into the 220 GHz band when using the molded lenslet, but lack of sensitivity to frequencies ranging from ~250 - 275 GHz. When looking at optical efficiencies in 6.1.4, because the simulated spectra was used

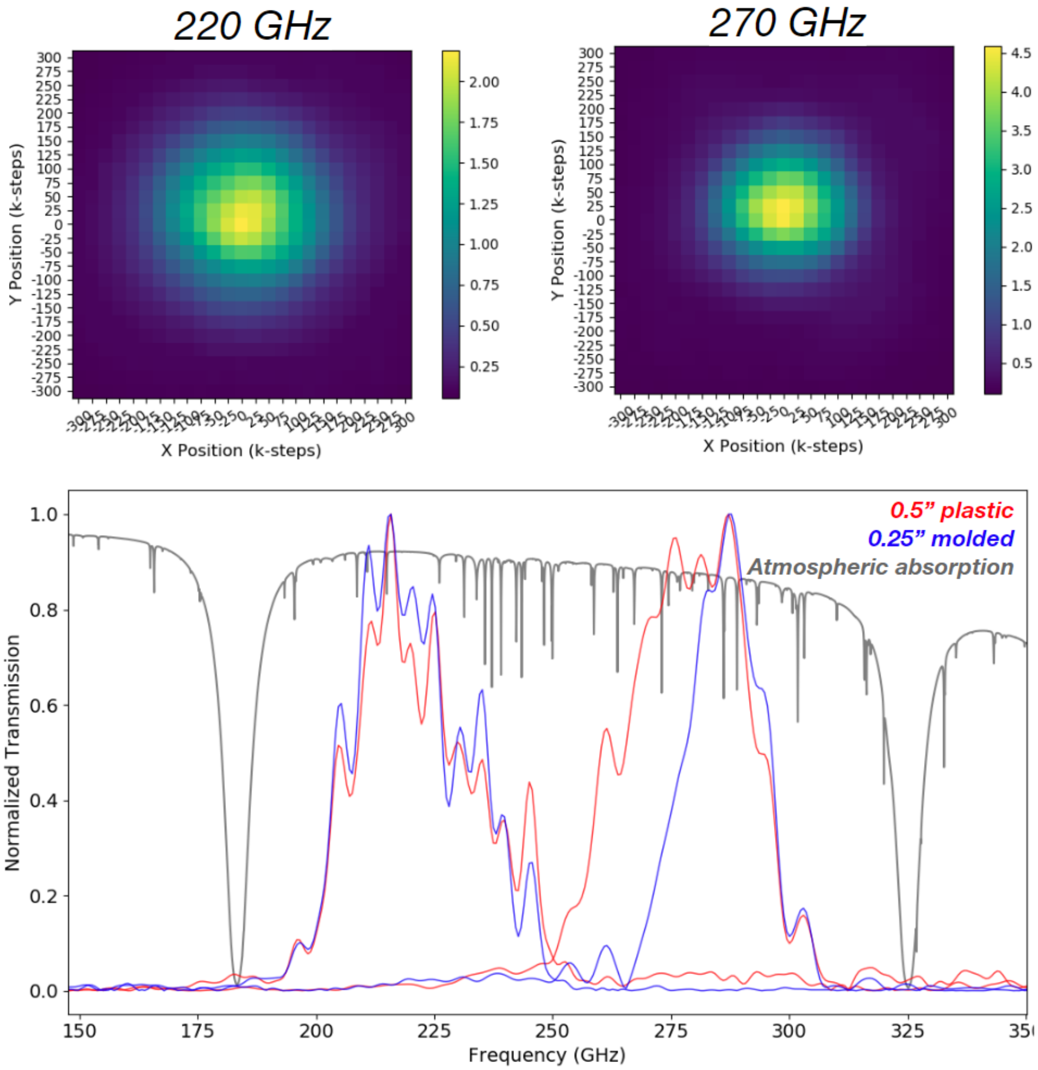

Figure 6.8: 220/270 GHz beam maps (top) and spectra (bottom). Beam maps are taken with a 6.35 mm molded-epoxy, seven-pixel lenslet array. Spectra shown include measurements from the same pixel, as well as a 12.7 mm alumina, single-layer plastic AR coated lenslet for comparison.

in the calculation, the lack of sensitivity in this region appears in the final 270 efficiency number as a 37% power deficit compared to the plastic AR coated lenslet. This feature proved difficult to explain and was not corrected before the cancellation of the program. One hypothesis is that either the epoxy used or the alumina used happened to be absorptive in this specific frequency band. Had the research continued, a warm measurement of the exact same epoxy coating on a flat sample would have been made to test this hypothesis.

The optical efficiency in the 220 GHz band for the epoxy-molded lenslet was on par with that of the plastic AR pixel, and the polarization efficiency was actually improved in both bands. The overall lower optical efficiency number is likely attributed to absorption of higher-frequency light by the filters in the dewar. These filters were not characterized for 220 and 270 GHz light and are suspected to have lower transmission at these frequencies. This hypothesis was confirmed after optical efficiency measurements of the molded lenslets were made in a separate cryostat in Colorado. These new measurements showed $\sim 2\times$ higher optical efficiency in the 220 GHz band (270 GHz was not measured). Transmission measurements of the 576 filter stack at 220 and 270 GHz would have been made for further verification had the program continued.

## 6.2 Monolithic lenslet arrays

Another method used to achieve an improved scalability of epoxy AR coated lenslets was monolithic machining. In this method, lenslets are machined from a bulk piece of silicon, and then epoxy is applied and machined back without removing the array from the CNC mill. In this configuration, the lenslets and lenslet extension piece exist in the same monolithic piece of silicon, eliminating the need for fabrication of a silicon seating wafer. This R&D was done in collaboration with the company ColdQuanta in Boulder, CO.

ColdQuanta utilized high-speed spindles to machine the bulk silicon and epoxy, although ultrasonic spindles have been theorized to be successful for this project because of their ability to machine brittle materials such as silicon. With a high-speed spindle, ColdQuanta was able to machine silicon effectively without excess chipping or fracturing of the bulk silicon. The high-speed spindle was also able to machine the epoxy AR coatings to within spec without damaging the epoxy.

Single-layer epoxy AR coated monolithic lenslets were machined in three different configurations: 6.35 mm diameter, 245 GHz centered AR for use in PB-2c, 5.6 mm diameter, 120 GHz centered AR for SO-MF, and 15.6 mm diameter, 35 GHz centered AR for SO-LF. It should be noted that during monolithic lenslet R&D, both PB-2c 220-270 GHz and SO-MF 90-150 GHz projects were canceled, with SO-MF switching from lenslet-coupled sinuous antennas to horn arrays coupled to ortho-mode transducers. SO-LF lenslets were baselined to have single-layer glass AR coatings after their monolithic R&D was completed, discussed in more detail in the sections below.

### 6.2.1 Mechanical implementation

To fabricate these lenslet arrays, bulk silicon was placed inside a CNC milling machine and machined to a specific diameter. A PTFE plastic barrier was then applied, shown in Figure 6.9, and epoxy was poured in. Without removing anything from the mill, this epoxy was machined back to the target thickness. For the full-size, 5.6 mm pitch SO-MF arrays, a special chuck was used that allowed the location of a fiducial feature to be within ± 10 $\mu m$. With this, laser-etched alignment marks could be made to align to a device wafer. However, this would be a large contribution to alignment error and would likely have been reduced had the project moved forward.

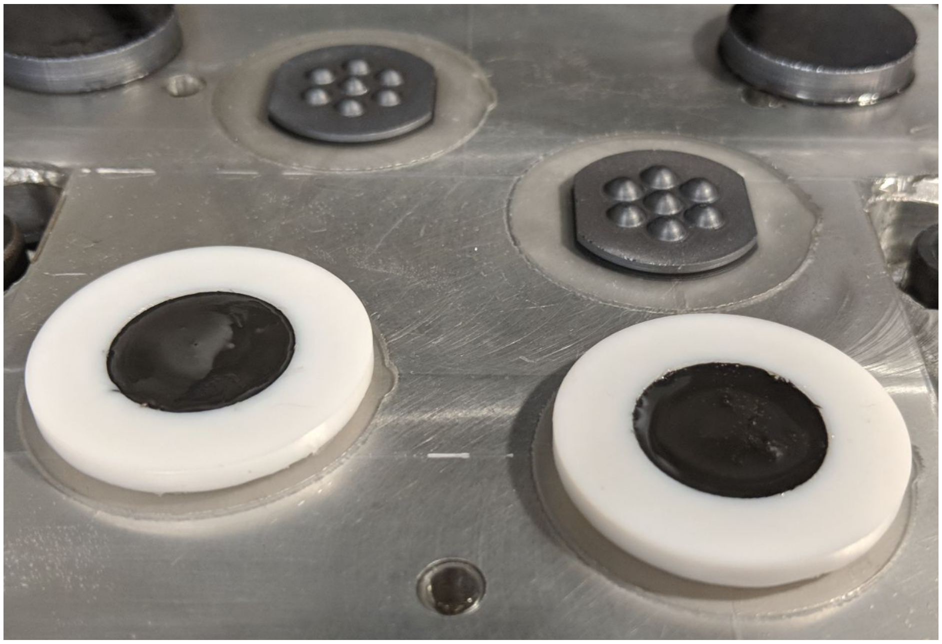

Figure 6.9: View inside a ColdQuanta CNC mill showing machined lenslets (top) and lenslets with epoxy applied in epoxy jig (bottom).

Given the nature of using an endmill to machine the epoxy coatings in-between the lenslets, some portion of the bottom of the lenslets would be machined outside of the thickness specification for the coating, creating a 'gap' in-between pixels. The corresponding effect was simulated by Aashrita Mangu. The realized gain for 90/150 GHz pixels with 5.6 mm pitch was shown to drop off when using an end mill $> 0.25$ mm in diameter was used at the coated frequency designed of 120 GHz. Moving to a 0.5 mm diameter tool was shown in simulation to decrease the realized gain by $\sim$10%. For all measurements shown in the following sections, a 0.5 mm diameter tool was used. ColdQuanta successfully performed machining tests using as small as a 0.2 mm diameter tool, which would likely have been used had the project continued. The downside of using a smaller tool was that it substantially increased machine time, effectively doubling the cost of each array when moving from a 0.75 mm diameter tool to a 0.25 mm diameter tool.

A full-sized prototype array for SO-MF pixels was successfully fabricated as a proof of concept before the end of R&D. This array can be seen in Figure 6.10.

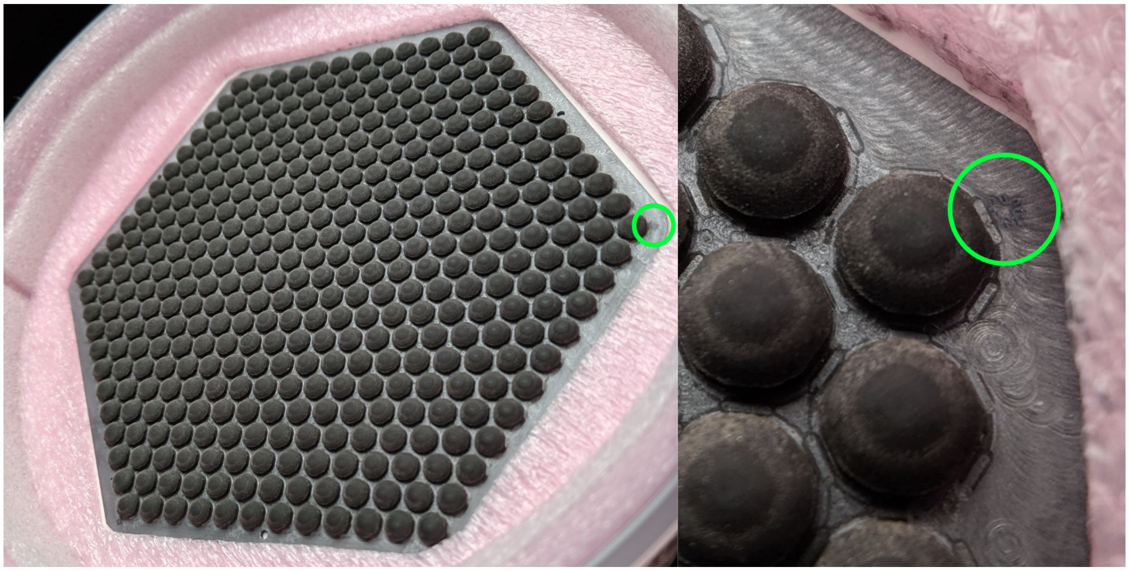

Figure 6.10: A monolithically machined lenslet array with a machined, single-layer epoxy AR coating for 5.6 mm 90/150 GHz pixels, with laser etched alignment markings (circled in green).

### 6.2.2 Mechanical evaluation

The precision of the CNC mill used was said to have given a ±5 $\mu m$ machining tolerance, and that was what the coatings were trusted to be within. Coating heights were measured to be within this spec, but total concentricity measurements in three dimensions were not performed. These measurements were planned to be made before the project was canceled, but were not made in time. These would have been done by sacrificing a machined lenslet array, cutting the lenslets in half to observe the coating uniformity.

During R&D, a number of cryo-mechanical failures were observed in different lenslet types. Both single-layer 220/270 GHz, 6.35 mm diameter pixels, and the 90/150 GHz 5.6 mm diameter pixels with Stycast 2850 epoxy coatings survived all cryomechanical testing. A 2-layer prototype coating was fabricated for SO-MF style pixels using Stycast 2850 as the bottom layer and Stycast 1090 as the top layer. These lenslet did not survive prototype testing, and cooling them down resulted in catastrophic failure, with entire silicon hemispheres detaching from their extension piece. This is thought to have happened for two potential reasons: The first hypothesis is that because the epoxy was thicker, the thermal contraction forces alone relative to the single-layer coatings increased beyond the tensile strength of the silicon, causing the silicon to fracture. The second hypothesis is that the bulk silicon was potentially damaged during machining, introducing microcracks. This, combined with an increased thermal contraction force from the epoxy, is likely what caused the arrays to fail. One prototype 7-pixel SO-LF array was also made. This array had much larger lenslets with a single-layer epoxy coating designed for 30/40 GHz bands, requiring a thicker epoxy coating.

The failure of this array, shown in Figure 6.11, was even more catastrophic than the aforementioned failure. Here, the significantly increased volume and surface area of the epoxy caused the entire array to fracture in many pieces. For these reasons, optical evaluation of only the single layer, 5.6 and 6.35 mm pixel pitch samples was performed.

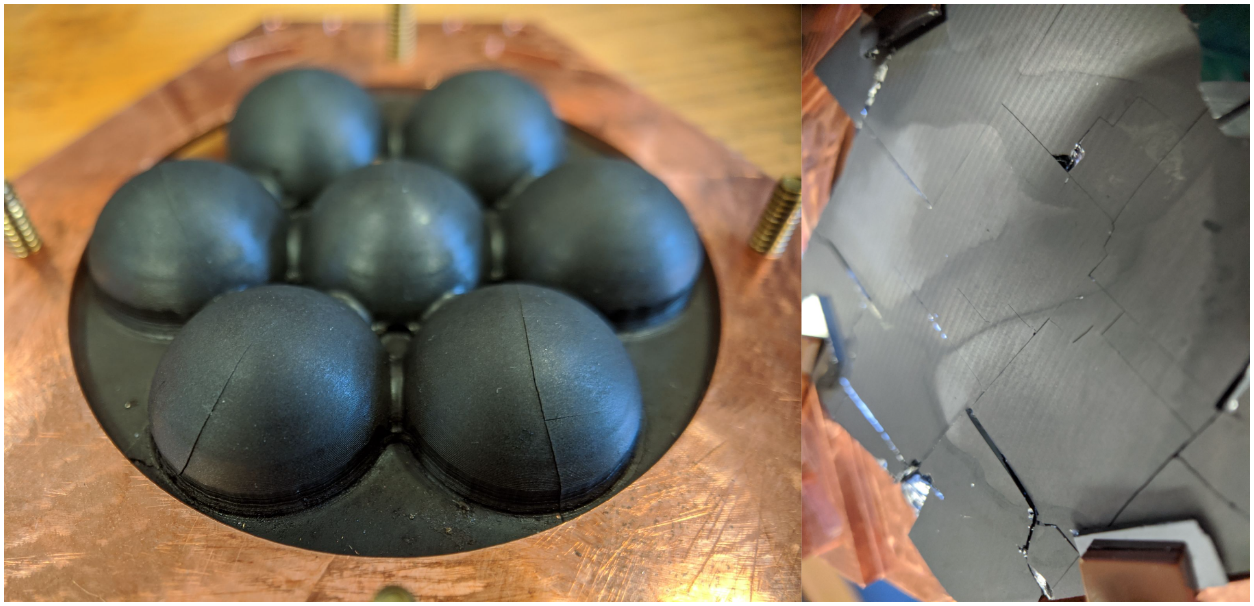

Figure 6.11: Cryomechanical failures of monolithically machined lenslet arrays, including 2-layer SO-MF lenslets (left), and single layer SO-LF lenslets. The center image shows the sky-side view of the SO-LF 7-pixel array post cryomechanical testing. The image on the right shows the same SO-LF 7-pixel array from the back.

### 6.2.3 Optical evaluation

As with the molded lenslet arrays, measurements in 576 were made using 7-pixel sample arrays, with prototype pixels aligned via the smart scope. The beam map and spectrum measurements of a prototype PB-2c lenslet can be seen in Figure 6.12, and the beam and spectrum measurements of the prototype SO-MF lenslets can be found in Figure 6.13. Optical and polarization efficiency measurements for each can be seen in Table 6.2.3.

Regarding the monolithic PB-2c pixel measurements, the spectra for the 220 and 270 pixel arrays looked much different from the epoxy-molded or plastic lenslet measurements shown in 6.8. The leading hypothesis was that microcracks produced by the milling machine in the silicon could have interacted with the light at these higher frequencies. For this to be true, the microcracks would have to be ∼1 mm structures in order for 220/270 GHz light to interact with them. The resulting decrease in optical efficiency can be seen in 6.2.3. The optical efficiency was ∼50% lower than for the molded alumina counterparts. The

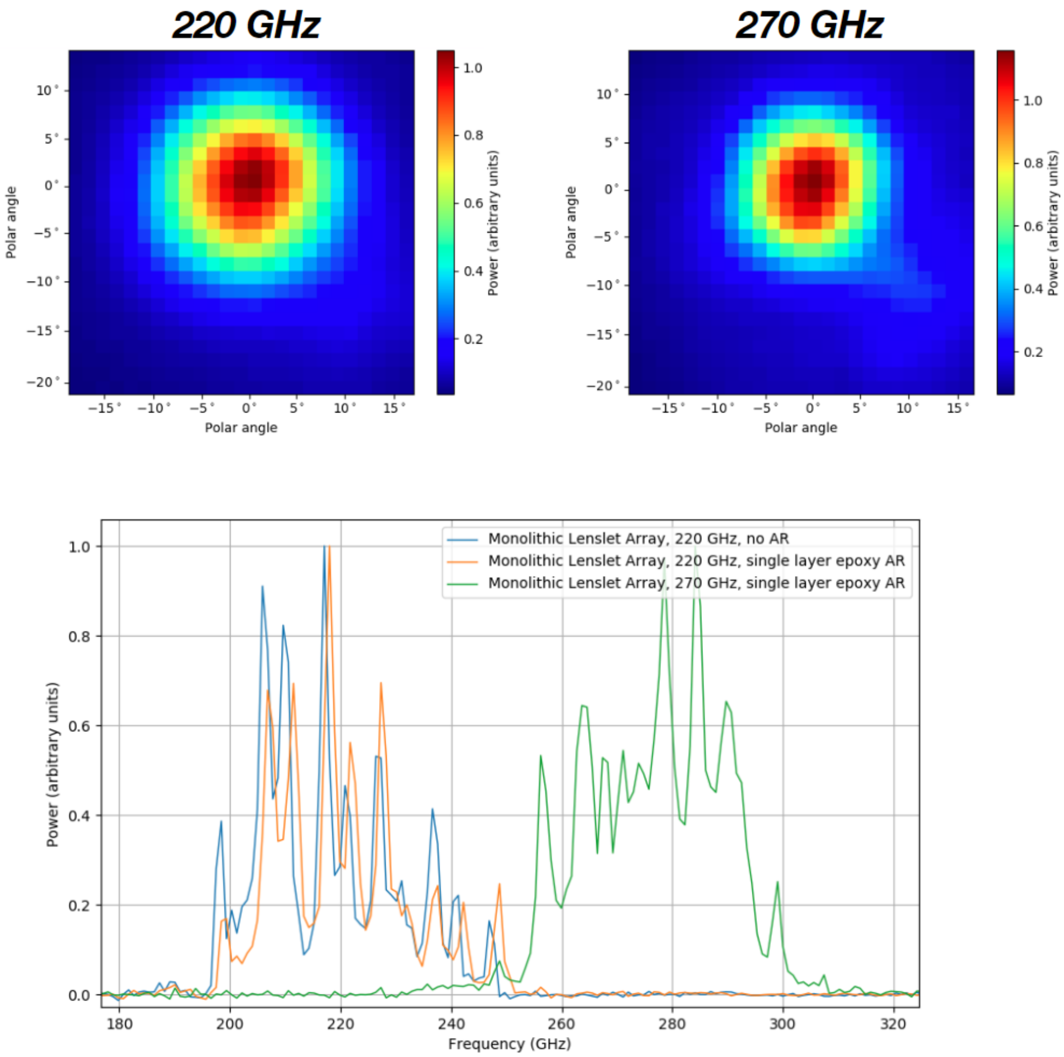

Figure 6.12: 220/270 GHz beam maps (top) and spectra (bottom) taken with a 6.35 mm monolithically machined, 7-pixel, silicon lenslet array with a single-layer, machined epoxy AR coating centered at 245 GHz. The plot of the spectra includes a measurement of an uncoated, monolithically machined silicon lenslet. Even though this spectrum looks similar to the AR coated sample, it is important to recognize that the plot is peak normalized, and the coated sample showed ∼15% increase in optical efficiency relative to its uncoated counterpart.

polarization efficiency in the 220 GHz band was comparable; however, it decreased by a factor of ∼2-3 in the 270 GHz band relative to the epoxy-molded lenslets. At this time, because epoxy-molded lenslet arrays for PB-2c pixels were tested to be more viable both optically and financially, R&D for monolithically machined, machined epoxy lenslets for

PB-2c was stopped.

Table 6.2: Machined epoxy AR with monolithically machined silicon lenslets vs. PB-2a/b pixel, optical efficiency and crosspol measurements

| | Optical efficiency 90 GHz | optical efficiency 150 GHz | crosspol 90 GHz | crosspol 150 GHz |
|---|---|---|---|---|
| Single layer epoxy AR (5.6 mm), 120 GHz band center | 67.5% | 58.8% | 3.6% | 1.5% |
| PB-2a/b deployment lenslet (6.35 mm) | n/a | 55.0% | 4.1% | 2.4% |
| | Optical efficiency 220 GHz | optical efficiency 270 GHz | crosspol 220 GHz | crosspol 270 GHz |
| Single layer epoxy AR (6.35 mm), 245 GHz band center | 19.6% | 18.4% | 2.9% | 8.5% |

All measurements were taken using Berkeley's 576 test stand. Optical efficiency calculations were done using simulated spectra. Dewar window + filter loss is estimated to be 75%. A measurement at 90 GHz for the deployment lenslet was not made as the detector was unable to transition at the dewar's base temperature of 250 mK.

Measurements of the SO-MF machined lenslets showed signs of fringing similar to their 220/270 GHz counterparts but maintained a much higher sensitivity on average across their bands. Table 6.2.3 compares these monolithic lenslet arrays with the deployment design, PB-2a/b lenslets. As a reminder these are 2-layer epoxy coated silicon lenslets with the same band center of 120 GHz as the monolithic lenslets. PB-2a/b lenslets were also measured in 576 for a direct comparison. Unfortunately, during the test, there was an issue with the 90 GHz channel saturating when observing the room-temperature blackbody source, and the 90 GHz optical efficiency could not be measured. However, the 150 GHz efficiency for both lenslet types is comparable, with the monolithic lenslets being slightly higher. It should be noted that these optical efficiency numbers are calculated using a simulated band. Any on-chip defects in the pixel's RF filters or other components could be contributors to a lower optical efficiency. As such, it is assumed that the true contribution to efficiency degradation from the lenslet is likely less than indicated in the recorded efficiency values. The crosspol numbers for the monolithic lenslets are lower as well, with the crosspol at 150 GHz being the lowest crosspol ever measured in the current iteration of the 576 test stand.

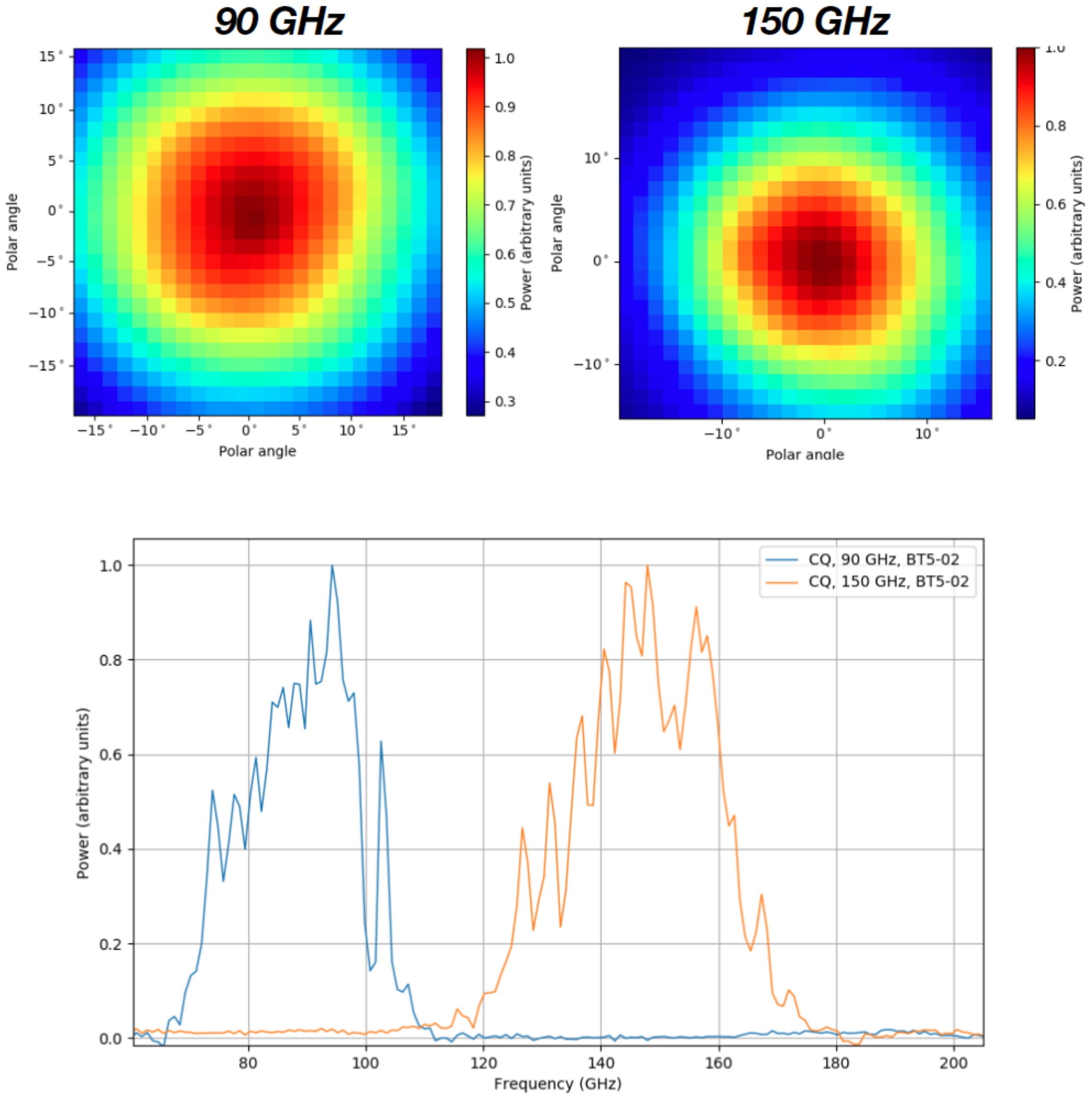

Figure 6.13: 90/150 GHz beam maps (top) and spectra (bottom) taken with a 5.6 mm monolithically machined, 7-pixel, silicon lenslet array with a single-layer machined epoxy AR coating centered at 120 GHz.

Measurements of the monolithically machined lenslets indicate potential viability for deployment in a CMB experiment. To further prove their efficacy, additional investigation into silicon microcracking needs to be done, as well as additional cryomechanical validation with higher statistics. Although Berkeley cryo-mechanical testing was successful, it was done on a relatively small sample size when compared to the number of pixels that a future CMB experiment may deploy. Additionally, costs of each array may need to be brought down, as the cost of machining each array may prove prohibitive.

## 6.3 Glass AR lenslets

As introduced in Section 5.2.4, the Simons Observatory low-frequency telescope will use a dichroic 30/40 GHz sinuous antenna design coupled to single-layer glass AR coated lenslets. These lenslets are designed around a center frequency of 35 GHz and are outsourced to the company Hyperion Optics for production.

### 6.3.1 Mechanical implementation

Hyperion Optics uses a borosilicate glass with a very thin glue layer to adhere the glass to the silicon lenslets. The silicon hemispheres are 15.6 mm in diameter, meaning a larger surface area between unlike materials has a higher risk of delaminations due to differential thermal contraction. In addition, a thicker single-layer coating designed for longer wavelengths means a higher volume of material in the AR coating, increasing the forces caused by differential thermal contractions. For these reasons, a material with a CTE nearly matching that of silicon is required.

Both borosilicate glass and quartz glass were selected as candidate materials. The boron doping in borosilicate glass provides an advantage here, making it less brittle than quartz glass. A small number of quartz glass coated lenslets were cooled down in a cryomechanical test, all of which ended with fractures in the quartz glass coatings. The failures here were not as catastrophic as the machined epoxy AR coating failures. The bulk silicon here stayed perfectly in-tact with glass still attached; however, the glass itself fractured in many places. The borosilicate lenslets have survived all cryomechanical tests so far, with five total lenslet arrays, each with 37 pixels having been created and cooled down in cryostats multiple times each for testing. Hyperion Optics also cryo-mechanically tests these lenslets before shipment using a liquid nitrogen bath.

Attaching the lenslets to an extension array is done similarly to the PB-2c epoxy molded lenslets, without the aid of a lenslet press jig to hold them in place. The epoxy dispenser can be used to attach the lenslets to their pockets without jig due to the added mass of the larger lenslets. This added mass means that the lenslets do not come out of their pockets as easily during array assembly, as did the smaller 6.35 mm diameter lenslets. Six dots of Sytcast 2850 epoxy per lenslet are used in the case of SO-LF, which has thus far resulted in zero mechanical failures.

### 6.3.2 Optical evaluation

Optical evaluation of the SO-LF lenslets is still in progress and has not yet been published. Initial tests using the 576 test stand yielded lower than desired optical efficiency, likely due again to the dewar's filter stack being optimized for 90/150 GHz testing. The installation of a new characterized low-frequency filter stack is in progress for the testing of the seven-pixel array in 576, while optical measurements on deployment arrays are in progress at the University of Chicago, Cornell University, and Princeton University.

## 6.4 Alternate lenslet technologies

Two other lenslet technologies were pursued without in-depth R&D programs that can be considered honorable mentions in this chapter: thermal sprayed lenslets and 3D printed lenslet arrays. The aim of these technologies was to improve lenslet array scalability in future experiments; however, both technologies produced confusing optical results and technical hurdles that led to the decisions to not pursue further R&D.

### 6.4.1 Thermal sprayed lenslets

Thermal spray is a plasma-sprayed coating that is sprayed onto pre-made lenslets or lenslet arrays as an AR coating. This technology has been successfully deployed for telescope receiver optics in both the PB-2b and SPT-3G telescopes [52]. The coating consists of silica and alumina-based powders that are doped with hollow alumina microspheres. The alumina microspheres are spherical shells of alumina that, when mixed with the thermal spray powder, lower the index of refraction of the mixture. These coatings are low-loss and CTE-matched to alumina, theoretically making them an ideal candidate for lenslet AR coating.

In practice, there were a few mechanical difficulties that hindered the R&D of thermal spray on hemispheres. First, although successfully applied to both 6.35 and 12.7 mm diameter alumina hemispheres, with the correct doping of alumina microspheres for a single layer coating at 90/150 GHz, the sphericity of the coatings was outside the specification defined for the concentricity of single-layer coatings given in Figure 4.9. A residual made from a confocal measurement of a 6.35 mm diameter thermal-sprayed alumina hemisphere is shown in (shown in Figure 6.14), revealing a $\sim$50 $\mu m$ RMS roughness, and an asymmetrical spray pattern, which deviates in the target thickness by $\sim \pm 150$ $\mu m$.

Adhesion of the plasma spray also became an issue, as certain samples saw delamination of the coatings. In addition, when the coatings were sprayed onto silicon, the silicon could not survive the process and would end up fracturing.

Although these problems were not inherently unsolvable for lenslets, they were initially less viable than their counterpart technologies at this stage in the research and thus were not pursued past this point.

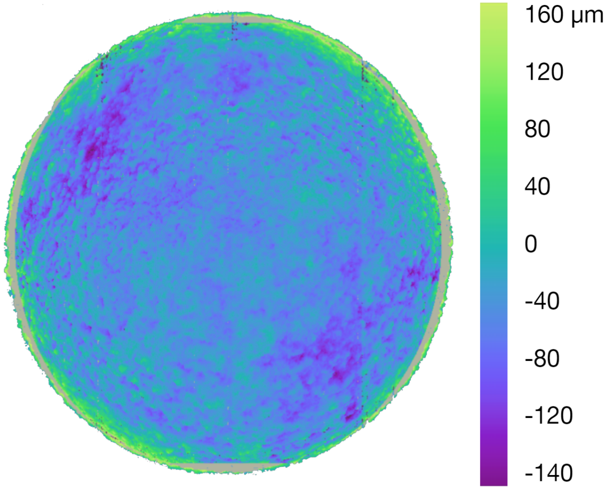

Figure 6.14: Confocal microscope measurement residual for a thermal sprayed lenslet.

### 6.4.2 3D printed lenslets

3D printed lenslet arrays were also briefly pursued, with the idea that they could reduce the manufacturing time relative to an array using individual hemispheres and silicon seating wafers. The company Cerhum was hired to manufacture seven-pixel 3D printed lenslet arrays with 6.35 mm diameter lenslets and did so successfully.

The main issue with the 3D printed lenslet arrays came from the fact that the resultant arrays were made of green alumina. This is a type of alumina produced from a ceramic slurry (used to 3D print parts) that needs to be heated to high temperature to harden and obtain the optical and mechanical characteristics of pure alumina. Without this heating process, the index of refraction of green alumina was too low to function as intended optically and produces asymmetric beams with low optical efficiency when compared to an uncoated silicon or alumina lenslet array at 90/150 GHz.

When green alumina is cured, the process changes the overall dimensions of the array, making it potentially difficult to achieve the target pitches for full-sized arrays that required no less than a 10 $\mu m$ deviation in the x-y plane to ensure alignment with the antennas.

Because of this, and because the arrays would still need to be AR coated after the printing and heating process, the decision was made to not pursue 3D printed lenslet technology further.

## 6.5 Metamaterial lenslets for LiteBIRD

The LiteBIRD space mission will use exclusively lenslet-coupled sinuous technology in its low and mid-frequency telescopes. Because these arrays will undergo launch vibrations and

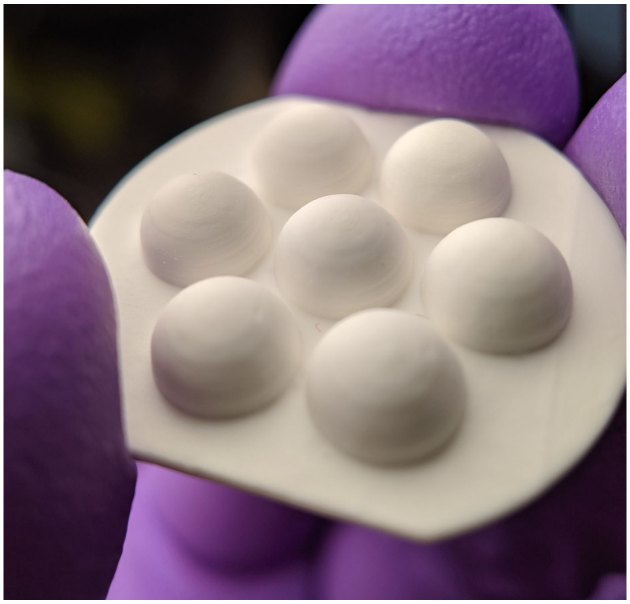

Figure 6.15: A 3D printed, ceramic, 7-pixel lenslet array.

because the pixel count is much lower than its ground-based counterparts, stricter criteria are put on the lenslets to ensure 100% yield. For LiteBIRD lenslets, the ease of mass producability is less of a concern than the lenslet survivability, and hence a new technology developed for LiteBIRD would have different requirements than the technologies outlined in the previous sections of this chapter.

To guarantee that an AR coating will not detach from the lenslet substrate during launch or cooling, the AR coating can be made part of that substrate. A sub-wavelength structure can be etched into the lenslet surface to produce an effective index of refraction. The etched geometry can be tweaked to vary the effective index of refraction as a function of depth in the lenslet to achieve high-transmission, wide-bandwidth structures. The resulting structure is known as a metamaterial, and its implementation to create an antireflection structure for LiteBIRD lenslets has been coined as a metamaterial anti-reflection structure (MARS).

It was determined that the most effective way of creating a MARS for LiteBIRD lenslets would be to etch holes using a laser; details of which will be discussed below.

### 6.5.1 Design overview and simulations

For LiteBIRD, a MARS must be as robust to launch vibrations as possible, while maintaining optimal transmission properties for each band. Because of this, a more robust bulk material is desired, indicating that an inverse moth-eye-style MARS may be preferable. The inverse moth-eye method has previously been proven successful in a stepped configuration from 32-38 GHz [53]. Separately, in a study of nanometer-scale metamaterial AR techniques, gradient moth-eye and inverse moth-eye structures were compared using geometries from 300-1000 nm [54]. It was found that the inverse moth-eye structures demonstrated higher transmittance and lower reflectance at all feature sizes compared to the non-inverse structures. For these reasons, an inverse moth-eye structure was selected for the LiteBIRD lenslet MARSs.

For this type of structure, the effective index of refraction of a MARS, $n_{eff}$ can be calculated as

$$n_{eff}(r) = \frac{N\pi a(r)^2 + (2\pi r^2 - N\pi a(r)^2)n_{Si}}{2\pi r^2}, \tag{6.1}$$

where $N$ is the number of evenly spaced holes in the lenslet, $R$ is the radius of the lenslet and $a(r)$ is the radius of the hole at a distance $r$ from the center of the lenslet ($0 \leq r \leq R$). To ensure that the holes do not collide, the diameter of the holes $2a(r)$ must be less than the distance between the centers of the holes on the surface of the lenslet $\sqrt{2\pi R^2/N}$, which gives a minimum effective index

$$n_{eff}(R) > n_{Si} - \pi(n_{Si} - 1)/4 \simeq 1.5. \tag{6.2}$$

To determine optimal hole geometries for given frequency bands, Nicole Farias and Alex Wang performed HFSS simulations using Floquet points to mimic an infinite array of holes with predefined geometries on a flat silicon surface [55].

To simplify the simulations, multilayered holes were simulated using three discrete geometries, each with their own effective index. Simulations with continuously tapered geometries are currently underway as well. Initial simulations show a strong dependence in the transmission to the fill fraction of the holes, or the ratio of empty space to silicon for each hole. This is expected because the fill fraction of the hole defines the effective index and at the top of the hole, it is desired to maximize the ratio of empty space to silicon to achieve an effective index as close to free space as possible. To do this, hexagonal holes are used for increased packing efficiency. To find a target geometry, simulations are performed of multi-layered, hexagonal holes on a flat silicon surface.

Etching a MARS onto a hemispherical surface raises the question: Will the geometries perform as well on a curved surface as they do on a flat surface? To help answer this question, Alex Wang at Berkeley has performed an angle-of-incidence study down to 45 degrees off incidence. The results show that an average transmission $>\sim 98\%$ can be maintained down to 45 degrees off incidence for bands ranging from 34 - 224 GHz using 3-layer hexagonal hole geometries in silicon. The simulations for the LiteBIRD LF-3 band (60-133 GHz) can be seen in Figure 6.16

Because in the reverse time-sense, a lenslet's beam is designed to exit as parallel light, additional simulations are required to show what percentage of a lenslet's forward gain this corresponds to, as well as simulations using steeper angles of incidence to characterize reflections at all angles from a lenslet's zenith. At the time of publication of this dissertation, these simulations have not been performed, but have been planned.

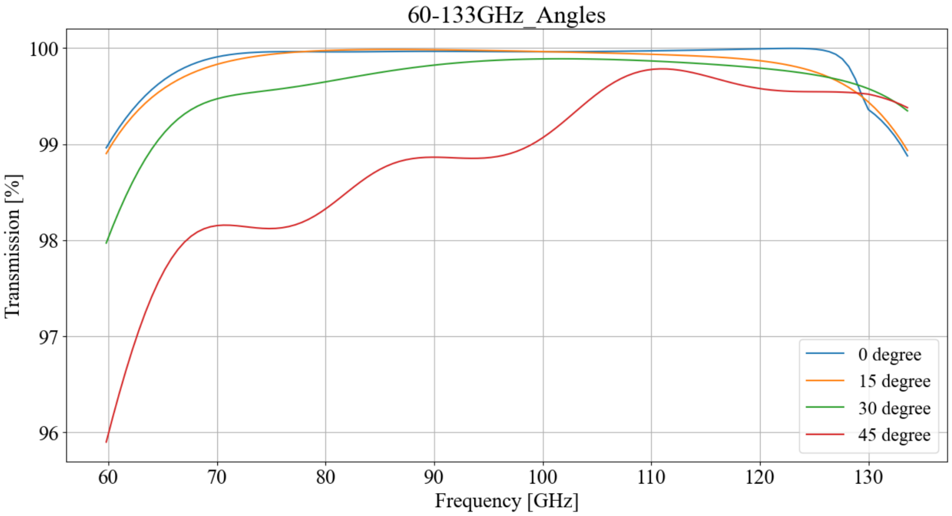

Figure 6.16: Simulations performed by Alex Wang showing transmission of a 3-layer hole geometry in silicon over a 60-133 GHz band (LiteBIRD's LF-3 band) at multiple angles of incidence.

If the off-incidence structure is shown to be a more critical problem than anticipated, it is possible to angle the holes themselves with respect to the normal at the lenslet's surface to compensate.

In practice, the produced laser-etched holes have some taper and hence do not have discrete layers as in the simulations. An AR coating with a gradually tapered index of refraction can provide several advantages over a stepped coating, namely, it removes reflections that occur at discrete layer surfaces, making it effective over a wider range of frequencies and incidence angles [46]. However, to maintain optimal refractive properties, the hole size and hole depth must be considered. A deeper hole allows for a more gradual taper, meaning that the optimal effective index of refraction in the MARS is maintained over a larger height, increasing sensitivity to longer wavelengths. In practice, the depth of an etched hole can be increased by varying the z-height of the silicon while lasing, changing the focus of the laser with respect to the silicon. The width of the hole controls the MARS's AR properties at shorter wavelengths, as the sub-wavelength structure must be much smaller than the wavelength of light in question in order to prevent refraction from the silicon alone. Therefore, transmission is limited at higher frequencies by the ability to maintain a given fill fraction in the silicon at smaller hole pitches. In silicon, the Berkeley laser is capable of producing edge widths between holes of ∼20 $\mu m$. In simulation, with this edge width, a three-layer ∼320 $\mu m$, edge-to-edge hexagonal hole has been shown to provide $> 99\%$ average in-band transmission in the LiteBIRD MF-2 band, which extends up to 224 GHz. Although sensitivity to frequencies higher than 224 GHz is not required for LiteBIRD, it is theorized that smaller holes with lower fill fractions could be created using the Berkeley test stand to achieve similar transmission figures for even higher frequencies. Ultimately, the hole size will be limited by the spot size of the laser, but the transmission would likely be low at that limit due to a low fill fraction.

To approximate this taper, 'lofted' holes were simulated that smooth the edges of the discrete, three-layer geometries. It was found that, in general, hole smoothing produced slightly lower average in band transmission (∼98% vs. >99%) for the simulated taper profiles, but much wider bandwidths, as shown in Figure 6.17.

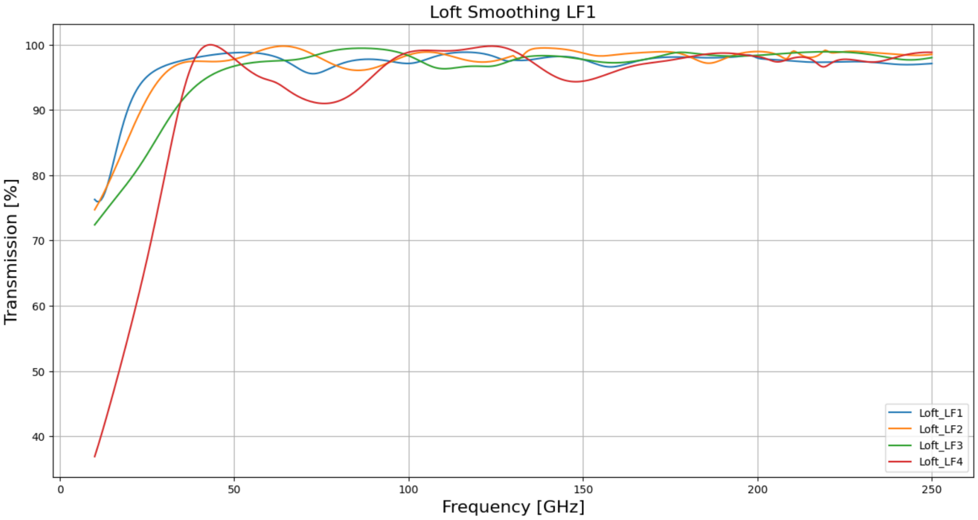

Figure 6.17: Simulations performed by Alex Wang showing transmission for each of LiteBIRD's LF frequency bands when converting their MARS optimized 3-layer geometries to lofted, tapered holes.

In future work, simulations of measured hole geometries will be performed, as well as more optimized taper profiles to achieve > 99% in-band transmission. Angle-of-incidence studies will then be performed to evaluate the expected transmission of etched, tapered hole geometries at various angles of incidence.

### 6.5.2 The laser

With LiteBIRD baselined to use silicon lenslets instead of alumina, a laser capable of efficiently etching silicon is required to produce an effective MARS. Typically, femto and picosecond lasers are used to etch silicon because their ultra-small pulse widths are capable of ablating silicon without melting and oxidization occurring. With the use of these lasers, high repetition rates (rep-rates) can be used to ablate the silicon at higher rates. Though ideal, these short-pulse-width lasers were outside of the allocated budget for LiteBIRD lenslets at the time R&D began. Longer pulse widths (micro& nanosecond) typically will deposit enough power into the silicon to cause melting. When tuning the laser's rep-rate then, a narrow threshold appears, below which the silicon does not ablate and above which ablating can occur, accompanied by melting and oxidization.

When the silicon melts, the surface becomes reflective, meaning that less power is then absorbed by the laser. Along with less power being absorbed, silicon oxides are produced that can then be melted by the laser. Kun Li's PhD thesis [56] however, provided an example where using a 1064 nm, nanosecond laser with the correct balance of laser power, pulse width, and rep-rate can produce silicon holes that can be etched at this threshold, avoiding excessive melting and oxide buildup.

Nanosecond lasers are typically ∼10× less expensive than femto or picosecond lasers, and with the knowledge of nanosecond etching from [56], as well as some new ideas, a nanosecond laser was purchased for LiteBIRD lenslet R&D. These new ideas would be: 1. To produce a nitrogen-rich environment, preventing the formation of oxides, 2. to clear the etched holes of any melted material in situ, and 3. use a built-in galvanometer so that the laser could be scanned over a surface, preventing localized heating and allowing hex shapes to be easily etched. All three of these ideas proved to be critical in achieving the desired hole dimensions and quality, as discussed later in 6.5.4.

The laser used is a 1064 nm, 2 ns pulse width, 100 W, 4 MHz rep-rate pulsed fiber laser with a built-in galvonometer. In searching for a laser to purchase, flexibility in parameters was prioritized, and as such, the laser in question is able to vary power, rep-rate, and pulse-width. The laser was purchased from a Chinese manufacturer and imported to the United States.

A word of warning: Anybody looking to purchase a laser overseas from a Chinese manufacturer should be cautioned to verify that the purchased product is certified with the FDA. The company the Berkeley laser was purchased from had forged FDA laser product documents, and the laser was held up in customs for almost a full year because of it. As a result, the entire Berkeley laser test stand, with the purchased laser, had to be certified as a laser product through the FDA to legally import and use the laser.

### 6.5.3 Laser enclosure

The enclosure for the laser, seen in Figure 6.18, is built over an optics bench and features aluminum walls, HEPA filter ventilation, and 1064 nm laser-safe plastic doors. To certify the test stand, the enclosure included, with the FDA, the enclosure was thoroughly checked for leaks at various angles of reflection inside the enclosure. To do this, a piece of silicon angled at 45 degrees was continuously lased as the silicon was spun around in circles. A laser power meter sensitive to 1064 nm light was used, along with IR-sensitive cameras, to search for light leaks around the enclosure, and none were found.

The enclosure also features four interlocks, two on each door, that are wired to the laser's power source. These, along with a software-controlled interlock, ensure that laser light cannot escape the enclosure under any circumstances.

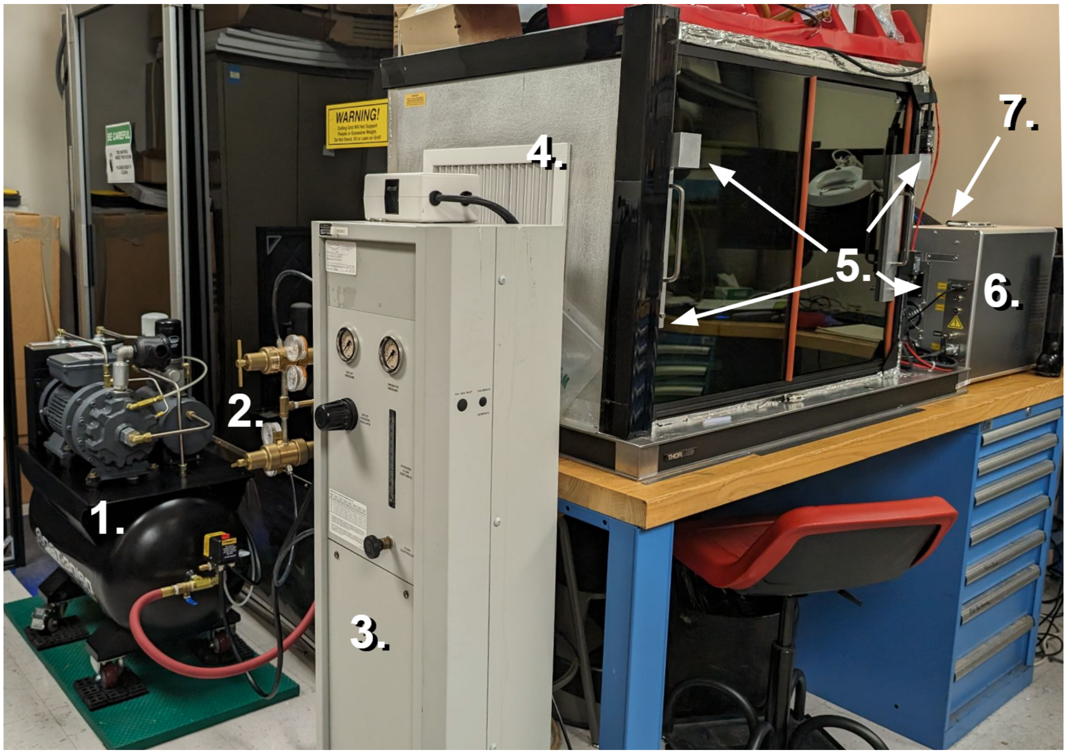

Figure 6.18: The outside of the laser test-stand. 1. The air compressor. 2. The dual regulator system that sends compressed air both the vacuum generators on the inside of the enclosure, and the nitrogen generator. 3. The nitrogen generator. 4. Laser light-safe intake vent for the HEPA filtration system. 5. The four door interlocks mounted to the laser enclosure. 6. The laser source. 7. (Not pictured) The HEPA filtration unit that attaches to the far side of the laser enclosure.

### 6.5.4 Silicon ablation accommodations

Once the laser was certified through the FDA and could be used for research, initial tests confirmed that with the correct parameters, silicon could be etched without substantial melting or oxidation, but when attempting to etch holes deep enough for MARS geometries, the melted silicon and the oxides produced were a limiting factor. A rudimentary system using luer-lock syringe tips and compressed nitrogen was used to remedy this issue. Initially, a compressed nitrogen cylinder was used, and the syringes were manually aligned to the laser spot for every etch. This alignment process took time and produced inconsistent results from etch-to-etch. In addition, it was found that excessive silicon dust was produced that would pile up on top of the etched sample. This dust is flammable and has been observed to ignite when small pieces of molten silicon land on a dust pile. It should be noted that some dust in the air was expected, hence the HEPA filtration system, but dust accumulation around the sample was not predicted. The HEPA filtration system is a required safety element, as inhaled silicon dust can cause severe respiratory problems.

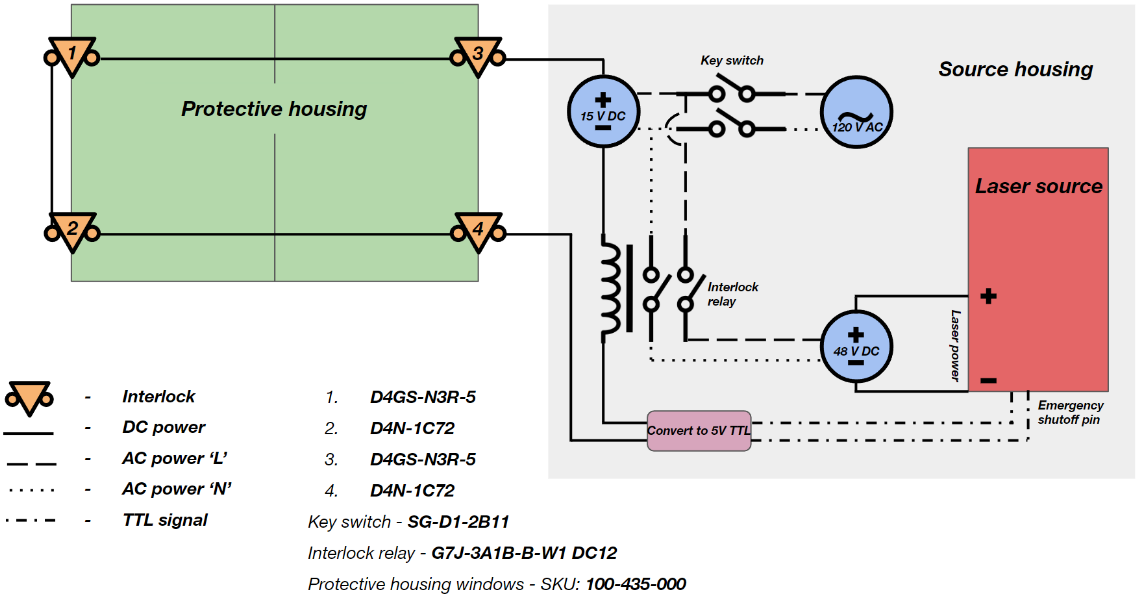

Figure 6.19: Block diagram showing the laser enclosure's interlock circuit.

To make alignment of the compressed nitrogen streams more consistent and to remove excess silicon dust, a continuous, compressed nitrogen, and vacuum system was developed. An industrial scroll compressor was purchased to flow compressed air to Venturi-effect vacuum generators inside the enclosure and to a nitrogen generator outside the enclosure to provide a continuous flow of nitrogen without the use of a cylinder. These systems can be seen in Figure 6.18.

Both the compressed nitrogen and vacuum lines connect to a specially designed nozzle as seen in Figure 6.20. This nozzle features a 3 mm wide opening for the laser to pass through and two large vacuum openings surrounding, along with a center vacuum connection (through the laser pathway) to remove silicon dust produced from etching. Once this dust is collected through the vacuum lines, it is removed via a water filter. Around the nozzle's laser opening is a small conical feature that connects to the compressed nitrogen inlet. This feature was designed to flow nitrogen over a small spot exactly at the lasers focus, modeling the flow in Solidworks Simulation software. It was machined using a 5-axis CNC machine by Gordon Long in the UC Berkeley Physics machine shop. Prior experience with the physics shop successfully machining extremely intricate parts motivated the design of this part. The nozzle proved challenging to machine, but was successfully machined to spec.

The nozzle works very effectively, eliminating melted silicon and oxide build-up when aligned correctly. For alignment, the nozzle is mounted onto its own locking x-y-z micrometer

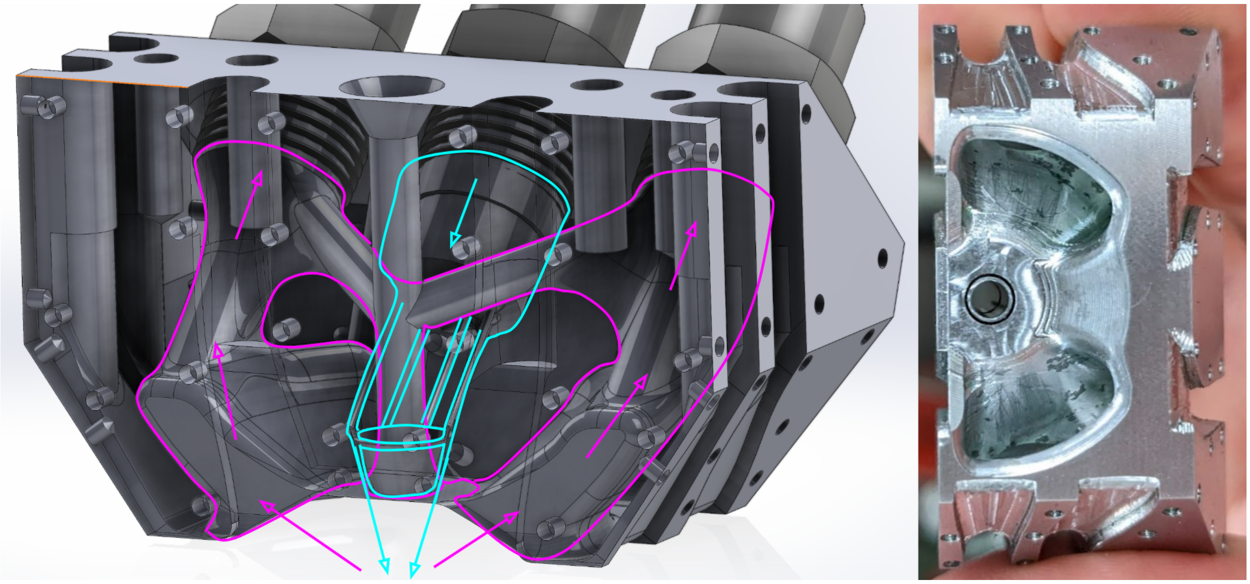

Figure 6.20: The bottom face of the completed nozzle (right) and a CAD diagram showing the nozzle's internal features (left). In the CAD drawing, the pink lines show which areas are under vacuum, and the cyan lines show the compressed nitrogen flow.

stage. The process involves multiple iterations to find the correct positioning.

The result of these efforts can be seen in Figure 6.21, which shows an identical hole pattern etched with and without the nozzle, nitrogen, and vacuum systems.

### 6.5.5 Six-axis system

A critical part of the laser test stand that allows MARSs to be etched onto both flat and hemispherical surfaces is a six-axis positioning system produced by the company Standa in Lithuania. Each stepper motor in the system is designed for sub-micron backlash, allowing for precise and repeatable hole placement. The six axes are x-y-z linear stages along with three rotation stages. The rotation stages are set up such that one controls the altitude angle on the hemisphere, and the last two are coaxial, controlling both the azimuthal location on the hemisphere and the angle of each hexagon on the hemisphere.

Aligning these positioning stages is a crucial step. If the x and y stages are not zeroed to within $\pm 5\ \mu m$ to where the laser spot is, or if the two coaxial rotational stages are not aligned to within $\pm 10\ \mu m$, artifacting is observed in the resultant hex pattern across a hemisphere. The x-y alignment is done by iteration, aligning the center of the sample holder to the laser roughly and then manually moving the stages until a resulting hemisphere etch at the zenith of a hemisphere is correctly placed. The difference in 5 microns can be seen in the hemispheres etched at zenith because of the azimuthal rotation rotating the hexagon location to a location displaced from true zero. The coaxial stages are aligned using dial

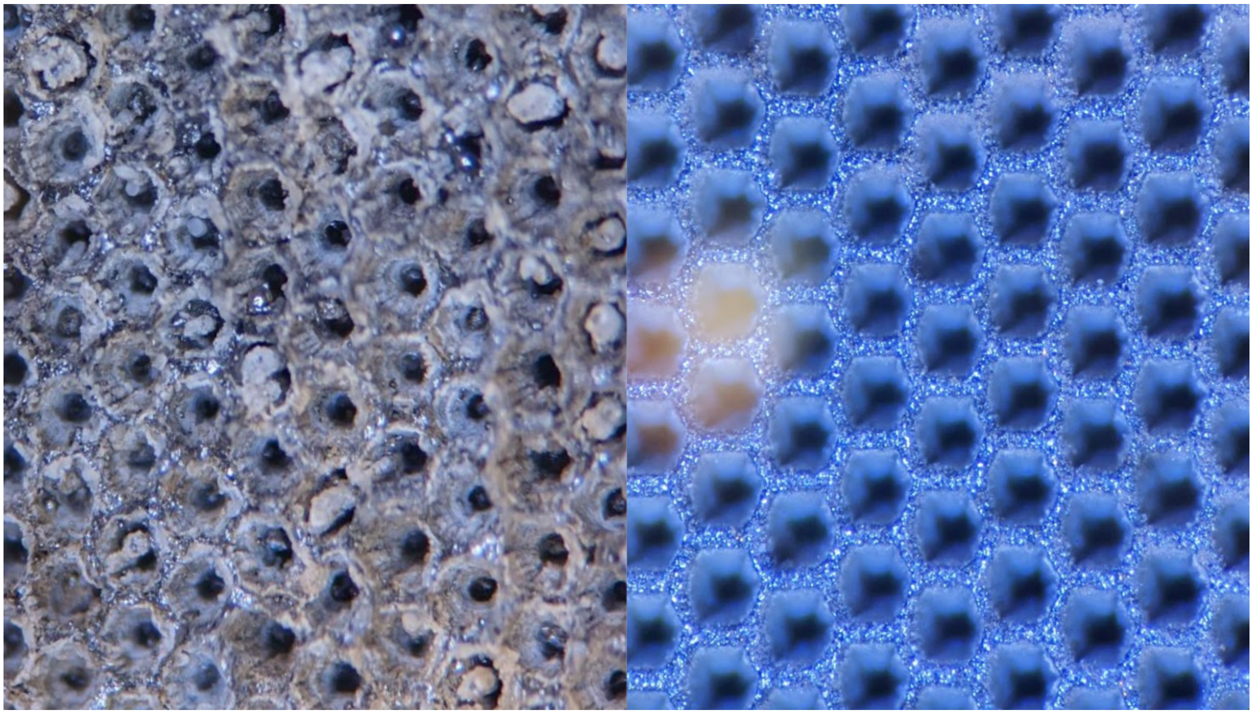

Figure 6.21: A comparison of holes lased in room air and no nozzle (left) vs. with nitrogen flowing through the nozzle (right).

indicators, rotating each individually with respect to the sample holder until they are within spec.

Mounted on the azimuthal rotation stage is the aluminum sample holder. This is a part designed to hold a specific-sized hemisphere or flat puck. A vacuum line is fed through the bottom of the sample holder, allowing it to function as a vacuum chuck for the samples. Both the six-axis system and the sample holder can be seen in Figure 6.22.

These drives and the laser are all controlled using a software package developed by undergraduate researcher Andrew Bogdan. The software takes into account the desired pitch of a MARS structure and the location of the hemisphere with respect to each of the positioning stages to define a coordinate system that keeps track of each hexagon's position and its rotation angle with respect to the hemisphere's surface. The 6-axis system can then be positioned such that the desired etch location on the hemisphere aligns to the in-focus laser spot at the correct orientation for each hexagon. The laser's own software is used to define laser etch geometries and parameters, meaning the pattern that is etched maintains a single orientation, and the lenslet must be correctly oriented underneath it to produce the desired pattern. The resulting etches are extremely consistent and can be reproduced with no observable differences between etches.

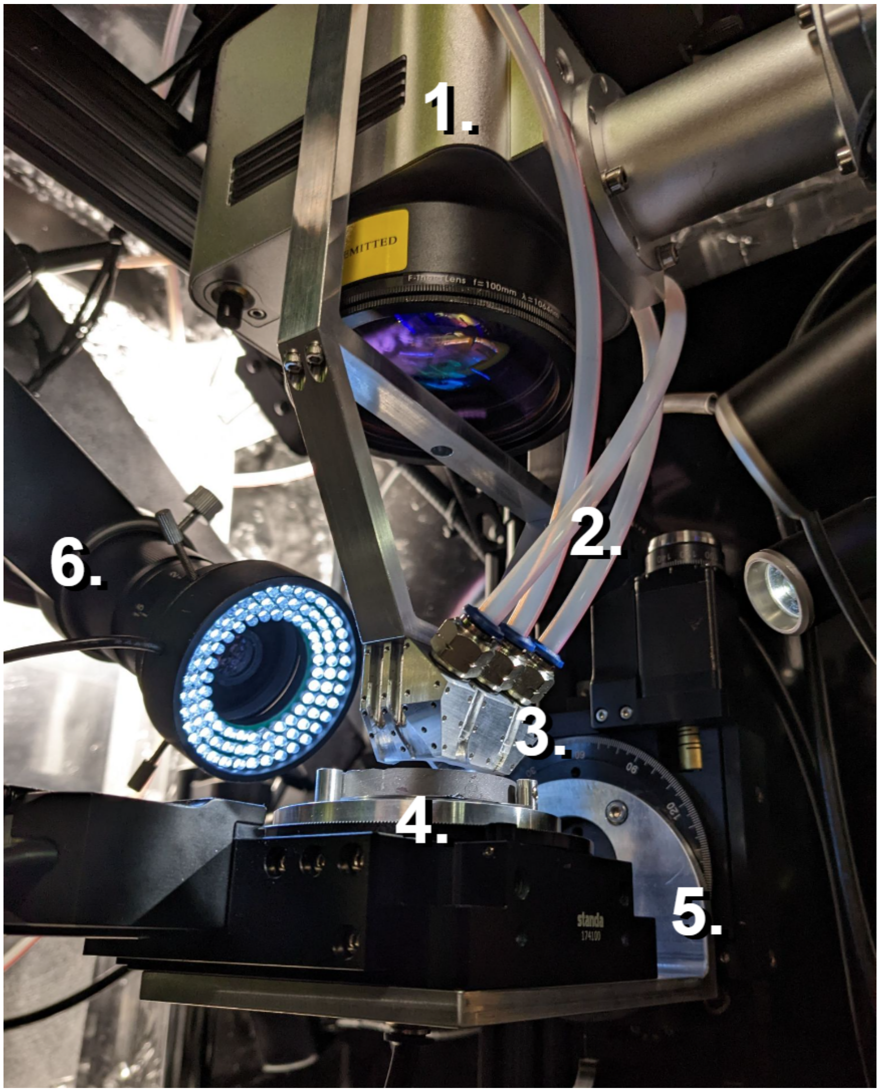

Figure 6.22: The inside of the laser enclosure. 1. The laser scan-head, with galvanometer enclosed and laser optics attached below. 2. The compressed nitrogen and vacuum lines connected to the nozzle, with the two outside lines being vacuum and the middle line being compressed nitrogen. 3. The laser nozzle. 4. The sample mount, set up for etching a flat sample as shown. Vacuum lines extends out the bottom of the sample mount so that it functions as a vacuum chuck. 5. The 6-axis stage. 7. A microscope to view the etch in real time.

### 6.5.6 Laser testing and results

To verify that the geometries of the etched holes closely match the geometries of the simulated holes, many laser parameters were iterated on and the resulting holes were evaluated using a confocal microscope and an optical microscope. The confocal microscope is used to verify the taper profile of the holes but is limiting in that it does not have enough power to illuminate all the way to the bottom of each hole. The optical microscope is used along with a micrometer stage that moves the lenslet height with respect to the microscope to measure hole depth.

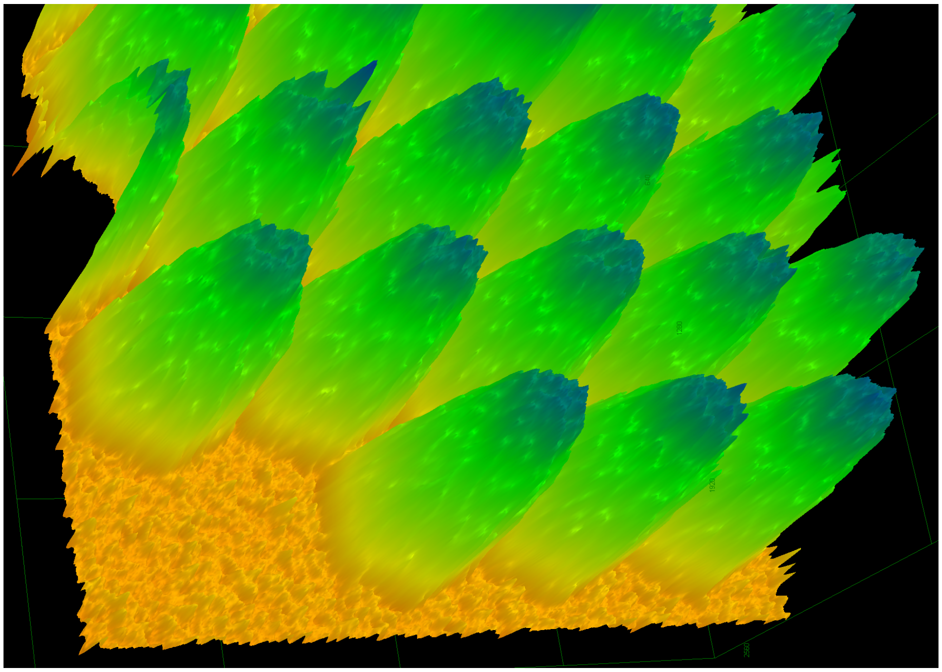

Figure 6.23: A confocal microscope measurement of a grid of 500 $\mu m$ wide hexagonal holes etched in silicon. Software can be used to make exact measurements for each 3D map produced by the microscope.

To achieve desired hole qualities, two etches are used. One etch creates the initial hexagonal hole, and a second scans the laser in a 2.5 mm circle around the hole to clean any dust away from the surface and purposely melt the edges around the hole. Melting the edges of each hole is an effective annealing process and removes any microcracks that could have been formed in the silicon that could compromise the structural integrity of the edge. For initial R&D, target geometries given from simulation for the LiteBIRD LF-3, 60-133 GHz band were used. To achieve these geometries, the following parameters were used:

Table 6.3: Laser parameters used to achieve a 60-133 GHz MARS geometry.

| laser power | pulse width | pulse energy | rep-rate | galvo scan speed |
|---|---|---|---|---|
| 70 W | 100 ns | 7 $\mu J$ | 50 kHz | 4000 mm/s |

Laser parameters used to achieve a 60-133 GHz MARS geometry. It is important to note that other parameters need to be adjusted as well, such as total number of marking loops made, galvonometer scan spacing, and galvonometer scan pattern.

At this repetition rate and galvanometer scan speed, a pulse with 7 $\mu J$ of energy is deposited into the silicon every 80 $\mu m$. The laser spot size with the current installed lens is $\sim$30 $\mu m$. With this spacing, the energy deposited into the silicon is distributed well enough so that excess melting does not occur. If the energy per pulse is too high or if the galvanometer scan speed is too slow, melting can occur beyond what the nozzle is capable of handling, and melted silicon buildup, along with some oxide production, can occur.

### Etching on a silicon flat

Using the above parameters to achieve the desired hole geometry, a two-dimensional grid of 550 $\mu$m wide hexagons was etched onto a flat silicon sample for measurement. The pattern was etched on both sides and took around three hours in total. The transmission, reflection, and absorption of this MARS was measured by Dick Plambeck using a heterodyne microwave source from 20-165 GHz.

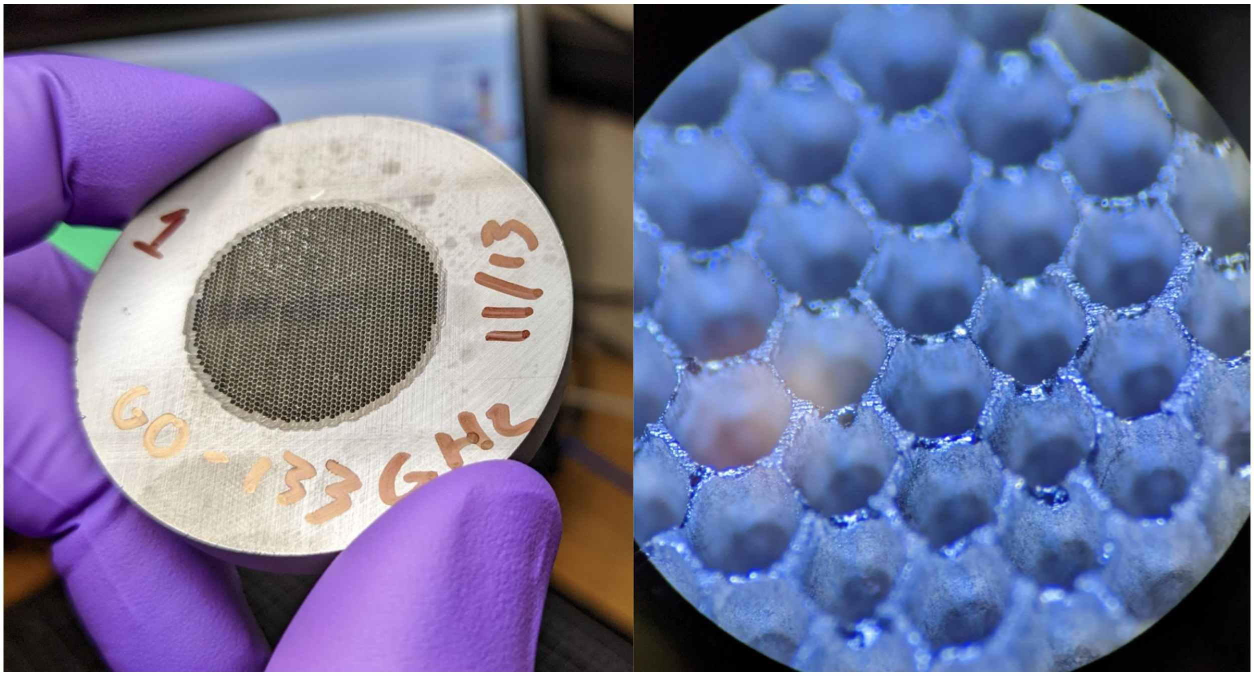

Figure 6.24: A silicon puck etched on two sides with a metamaterial AR designed for 60-133 GHz.

The measurement in Figure 6.25 shows a flat in-band average transmission from 60-133 GHz, which extends up to 165 GHz. Though not shown in this figure, transmission above 165 GHz began to drop off, due to refraction at the surface caused by smaller wavelengths interacting with the etched features. For higher frequency bands, smaller hexagons 320 $\mu m$ wide will be etched. With $\sim$10% absorption in silicon, the average in-band transmission per side of the measured sample is $\approx$97.5%. Although this is below the expected in-band transmission of $> 99\%$ for a discrete 3-layer coating, it is near identical to the simulated transmission in the LF-3 band for the geometry of a tapered hole shown in Figure 6.17.

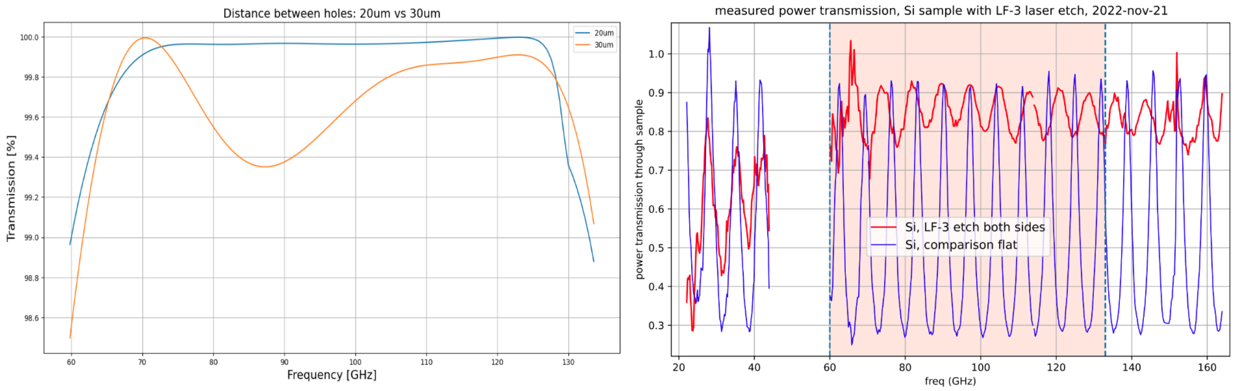

Figure 6.25: HFSS simulation (left) and measurement (right) of a MARS designed for the LiteBIRD LF-3 band, 60-133 GHz, on a silicon puck. Transmission is simulated for two different edge widths (the thickness of silicon between hexagons), using a '3-layer' hole to approximate the lased geometry. These simulations were performed by undergraduate student researcher Alex Wang. The measurement was made by Dick Plambeck with a heterodyne source, measuring the power transmitted through the silicon puck. The measurement results show $\sim$10% absorption due to dielectric loss in the bulk silicon, and an average loss of $\sim$5% due to reflection across the silicon puck. Both sides of the puck were etched with the MARS, so this measurement shows $\sim$2.5% reflection loss at each surface.

The current lenslet transmission requirement for LiteBIRD in all LF and MF bands is 80% average in-band transmission. However, with higher lenslet transmission, higher optical throughput can be had, meaning increased experimental sensitivity and mapping speed. To maximize the chances of a tensor-to-scalar ratio measurement in LiteBIRD, R&D will continue on hole geometries and taper profiles to improve the transmission of each MARS to $> 99\%$.

### Etching on a hemisphere

A mapping of a hexagonal grid onto a three-dimensional sphere is known as a geodesic polyhedron. These patterns, like a soccer ball, will always contain a certain number of pentagons interspersed with the hexagons. The hemisphere etching software is capable of creating all classes of geodesic polyhedra and picks one that is most closely matched to the hemisphere's diameter and pitch requirements. Because this mapping creates a slightly varied pitch across the hemisphere, pitch thresholds are created and slightly different sized hexagons are etched at each threshold, changing by $\sim$10 - 20 $\mu m$ in width at each threshold. The pentagons are also appropriately sized in the laser software and etched. These slight differences from a perfect two-dimensional hexagonal grid create tiny variations in the index of refraction across the hemisphere. Simulations are planned to see the effect of the etched fill fraction variations on transmission.

To test software iterations without having to sacrifice an expensive silicon hemisphere, dummy hemispheres made out of Delrin plastic are used. These are machined to the same dimensions as their silicon counterparts and marked with a marking ink. The marking ink is then lased away using an adjusted laser power. A silicon-ready etch pattern is shown on a Delrin hemisphere in Figure 6.26. The total etch time for this dummy hemisphere was ∼1 hour.

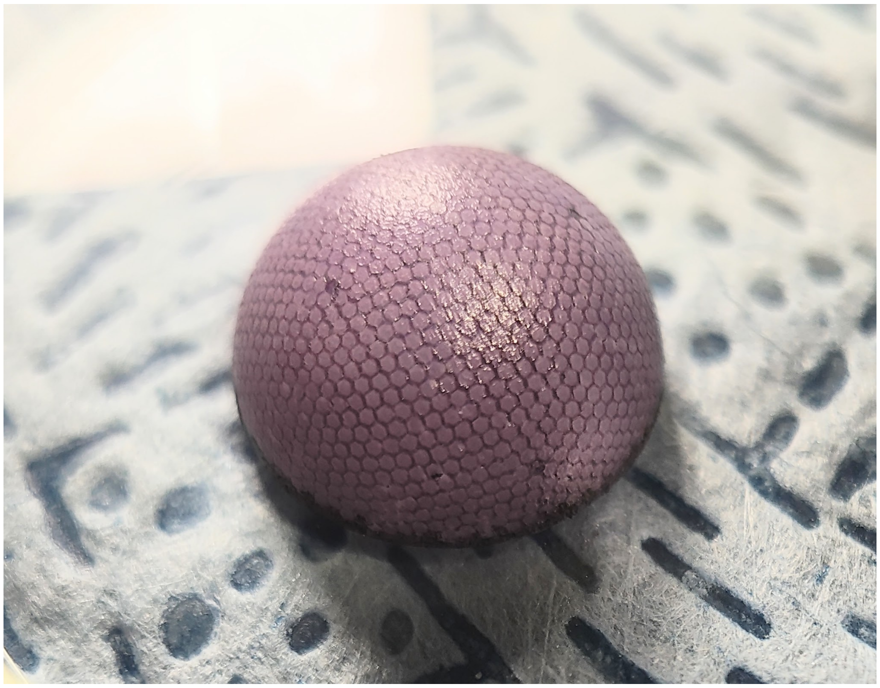

Figure 6.26: A 'dummy' hemisphere etched with a hex grid. Note that discoloration is due to inconsistencies in reference ink. Blank spots are where pentagons are yet to be etched.

Moving from Delrin to silicon requires some verification of etch dimensions, so the three-dimensional geodesic polyhedron is projected in two dimensions and etched onto a flat piece of silicon before moving to a hemisphere. As of the time of writing, a silicon hemisphere has yet to be etched, as the verification of the laser parameters for the projected geodesic polyhedron on a flat piece of silicon is in progress. It is expected to have an etched silicon hemisphere for LiteBIRD's LF-3 band by late 2023 - early 2024.

### 6.5.7 Future work

After a silicon hemisphere is etched, it will be optically tested in 576 and compared with a single-layer glass AR coated hemisphere with a 120 GHz-centered coating. Both measurements will use the same pixel and detectors for a direct comparison. Any iteration of this design can then occur after optical characterization has been performed. After this, geometries for the remaining LiteBIRD bands will be etched onto flat silicon pucks and measured, and then etched onto the hemispheres when ready.

New research must also be performed to determine the method of attaching the hemispheres to their extension arrays. Although the epoxy method used in SA and SO-LF may be viable, a more robust solution is preferred. The likely first step in this research is to try anodic bonding of the two silicon surfaces, but no R&D has been performed so far.

# Chapter 7

# Cosmic Ray Mitigation for LiteBIRD

One consideration for the LiteBIRD experiment that is unique when compared with its ground-based counterparts is its susceptibility to cosmic ray events. In orbit at L2, LiteBIRD will primarily be exposed to a mixture of high-energy galactic cosmic rays and charged particles from the sun. Without careful control over the systematic effects caused by these particles, LiteBIRD's ability to reach its sensitivity goal of $\delta r < 0.001$ may suffer.

LiteBIRD's predecessor, the Planck satellite, was primarily impacted by such cosmic rays in its HFI telescope. In the HFI, 95% of the data samples were contaminated by cosmic rays appearing in the time-ordered data as "glitches", and on average 16% of all data taken was lost due to glitch contamination [57]. LiteBIRD shares two features in common that contributed to the data loss in Planck: Observation at L2 and low-temperature bolometer detectors.

Because of these commonalities, extensive simulation and experimental work must take place to determine LiteBIRD's level of susceptibility to high-energy radiation, as well as the need for hardware mitigations.

## 7.1 Cosmic rays at L2

Because Planck observed during a solar minimum, the most significant cosmic ray contribution was from galactic cosmic rays (GCRs). These cosmic rays are primarily protons whose flux had a strong anticorrelation with solar activity at energies below ∼10 GeV. The energies of incoming protons observed by Planck typically ranged from 35 MeV to 10 GeV, with a peak around 200 GeV and a low-energy cutoff of 39 MeV as a result of shielding from Planck's focal plane unit box [58].

Solar particles typically have energies in the keV range; however, during a solar flare, these energies can reach up to 100 MeV and occasionally higher, and are detectable by Planck detectors. It was reported that during a solar flare the temperature of the satellite would increase enough to affect the working point of the bolometers. Other anomalous particles, such as photoionized interstellar hydrogen or other heavy elements, can be accelerated by the termination shock of the heliosphere, resulting in cosmic rays ranging from ∼100 keV - 100 MeV, which did not prove to be significant for Planck.

LiteBIRD is expected to launch and begin its campaign during a solar minimum, with observations being made as solar activity increases. The result of this is that a higher flux of GCRs is expected. This is important for simulation and modeling, which is typically done using Planck-era cosmic ray spectra, which also contained a high GCR flux [59].

## 7.2 Cosmic rays in Planck

In order to effectively design against cosmic ray impacts in LiteBIRD, it is important to understand their origins and mechanisms in the Planck satellite, along with mitigations in data analysis. This section will detail design differences between LiteBIRD and Planck, what Planck saw in its data, why these cosmic ray events impacted the data, and how their impact was mitigated in analysis.

### 7.2.1 The Planck bolometer

There are a few differences main differences between a LiteBIRD TES bolometer and Planck NTD germanium bolometers. Firstly, LiteBIRD bolometers are TES bolometers, utilizing a superconducting element to detect changes in heat at the absorber, whereas Planck used semiconducting bolometers to detect changes in heat on its absorber. The absorbers in Planck are a suspended silicon nitride membrane that is metalized. This structure is used as a cosmic ray mitigation, minimizing the total absorber cross-sectional area, while maintaining a high effective in-band surface area. Even though the cross-sectional area is minimized, it is still much larger than LiteBIRD's titanium load resistor absorber design.

Additionally, a key difference between the detector arrays in each experiment is the fact that the LiteBIRD arrays contain many more detectors, many of which share a common substrate. Because each TES has its own thermal conductance path to a common silicon bath, temperature changes in the bulk silicon substrate can affect multiple detectors simultaneously, resulting in coincidence events between detectors. The resulting coincidence events will appear as low-level thermal fluctuations common between multiple detectors, resulting in a common-mode white noise background due to cosmic ray impacts [59]. An increased white noise level will decrease the sensitivity of a pixel at all frequencies. Because of this, mitigating such a white noise spectrum will be a critical factor in achieving LiteBIRD's sensitivity goals.

### 7.2.2 Glitch types and their effects

In its HFI telescope, Planck saw three different populations of cosmic ray glitches: short, long, and slow [60]. Below, each of these glitch types will be outlined, and their origins considered.

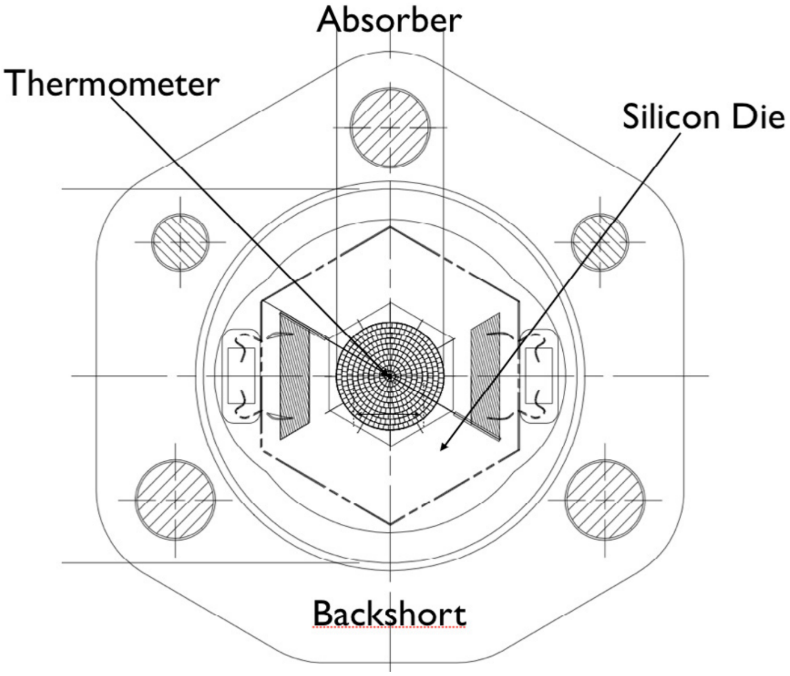

Figure 7.1: Drawing of a mounted Planck spider web bolometer and its constituent components in the HFI. Image credit: Catalano et al. (2014) [58]

### Short glitches

Short glitches are features seen in the data as sharp spikes, whose amplitude decays quickly on the order of 5-10 ms. [60]. They have intermediate and long time constant components as well which decay on the order of 10s and 100s of ms, respectively, with amplitudes around an order of magnitude lower than the fast time constant component. The origin of these short glitches was shown to have been the result of a particle impact directly on the absorber grid or NTD thermistor on the bolometer.

### Long glitches

Long glitches have the same fast time constant component of short glitches, but with intermediate and long time constant components whose amplitudes are around two orders of magnitude higher than those in the short glitches, resulting in an overall much longer decay time [60]. The long glitches were shown experimentally to most likely exist as a result of impacts on the silicon die, as the bolometers were shown to be sensitive to temperature changes in the silicon. It is important to note that the low signal energy cutoff given from long glitch modeling is close to the experimental noise level, potentially leading to a negative impact on Planck's HFI cosmological goals [60].

### Slow glitches

Slow glitches have the same decay characteristics as long glitches, but lack the initial fast decay component [60]. They were the rarest of the three glitch types and occurred only in one type of Planck's HFI detectors, the polarization sensitive PSBa bolometers. They were not replicated in ground-based testing, though they are thought to originate from impacts incident on the PSBa feedthroughs, causing heating in the silicon bath. The smaller size of the feedthroughs relative to the silicon bath is believed to explain their lower rate compared to long glitches [60].

### Energy deposition

The energies deposited from each type of glitch ranged from eVs up to GeVs. Low energy pulses (comparable signal amplitude to RMS noise) occurred with a frequency of around $10^4$ events per hour. Glitches with 1 keV of absorbed energy at the detector occurred ∼10-100 times per hour, and pulses with higher energy (>∼50 keV) ∼0.1 times per hour [57].

The short glitch energy spectrum extends all the way out to MeV energies, with the higher energy events thought to be caused by alpha particles or heavy elements impacting the absorber or thermistor. Long glitches have an upper limit energy cutoff ∼10-100 keV, and slow glitches have an upper limit energy cutoff ∼3 keV [57].

## 7.2.3 Mitigation work

To mitigate the impact of these glitches on the experiment noise levels, an extensive deglitching was performed on the raw data. With models of all three glitch types, glitches were identified and subtracted from the data. Residual glitch contamination was at the level of 5%, due to long glitches falling below the glitch finder threshold [57].

LiteBIRD will have a relatively low sample rate of ∼20 Hz, and coupled with a fast TES response time on the order of milliseconds, individual glitches will not be able to be resolved and removed. Because of LiteBIRD's continuously rotating HWP, additional intensity due to cosmic ray events in the demodulated signal will impact the determination of the Q and U Stokes parameters. A source of systematic error occurs when there is a differential temperature signal in orthogonal polarimeters. Regardless of the presence of a rotating HWP, a mismatch in temperature observed by orthogonal polarimeters will cause Q-to-U leakage [59]. Although the level of this leakage is not currently estimated, it is important to consider given the low-level primordial B-mode signal. These systematic effects, in tandem with the inability to remove individual glitches, highlight the importance of a hardware-side cosmic ray mitigation solution for LiteBIRD.

## 7.3 Phonons propagation and mitigation strategies

To successfully mitigate glitch events in LiteBIRD data using physical features on or near the detector wafers, it is important to understand the mechanisms for how these temperature changes are seen by the detector. This section will discuss how absorbed energy from an incident cosmic ray is propagated through the detector wafer to the detector to be measured as a spike in temperature. Mitigating the energy propagation will also be discussed.

### 7.3.1 Phonon propagation

Upon impact, a high-energy particle or high-energy radiation will deposit some energy into the incident substrate. The resulting ionization and excitation in the material create energy fluctuations that propagate as diffuse and ballistic phonons. For the short glitches seen in Planck, direct particle interaction between the incoming particle and incident absorber or thermistor material creates phonons which appear as a sharp power increase in the data, as the thermistor sees the increased phonon production from the impact. The majority of the high-energy impacts were seen as short glitches in Planck, consistent with fast energy absorption on the absorber or thermistor and little minimal thermal diffusion.

Depending on the energy of the phonon and the material properties, the phonons can scatter off of other phonons or electrons, scatter at material boundaries, or transmit through material boundaries. If a phonon is energetic enough such that its mean free path in a material is greater than the length scale of the material, it is considered ballistic. These phonons can down-convert to lower energy diffusive phonons when scattering off of conduction electrons or material impurities or can penetrate adjacent material layers. In the case of Planck's long glitch events resulting from events occurring in the detector's surrounding silicon substrate, ballistic phonons created from the impact have high enough energy to penetrate the silicon-silicon nitride boundary between the silicon and absorber, and hence can travel through the silicon nitride absorber legs to the germanium thermistor. The longer time constant is attributed to the non-ballistic thermal diffusion between the silicon and the detector [58]. It was found that this thermal diffusion time constant was consistent with the heat capacitance of the silicon and the thermal conduction of the silicon to the detector. As a direct test of this hypothesis, 75% of a detector's absorber legs were broken as a means of removing the path for ballistic phonons to propagate on. In testing, this method resulted in a decrease in the amplitude of the initial pulse caused by ballistic phonons, but maintained the same thermal diffusion time constant [58].

In a superconducting metal, phonons with energies above the superconducting gap energy will break Cooper pairs. A broken Cooper pair results in what is called a Bogoliubov quasiparticle - a coherent superposition of a negatively charged electron and a positively charged hole. This quasiparticle can travel through the superconductor, eventually recombining when interacting with another quasiparticle to create diffusive phonons in the metal. LiteBIRD detector wafers use a superconducting niobium ground plane, superconducting niobium microstrip lines, and bias lines, and of course a superconducting niobium-titanium

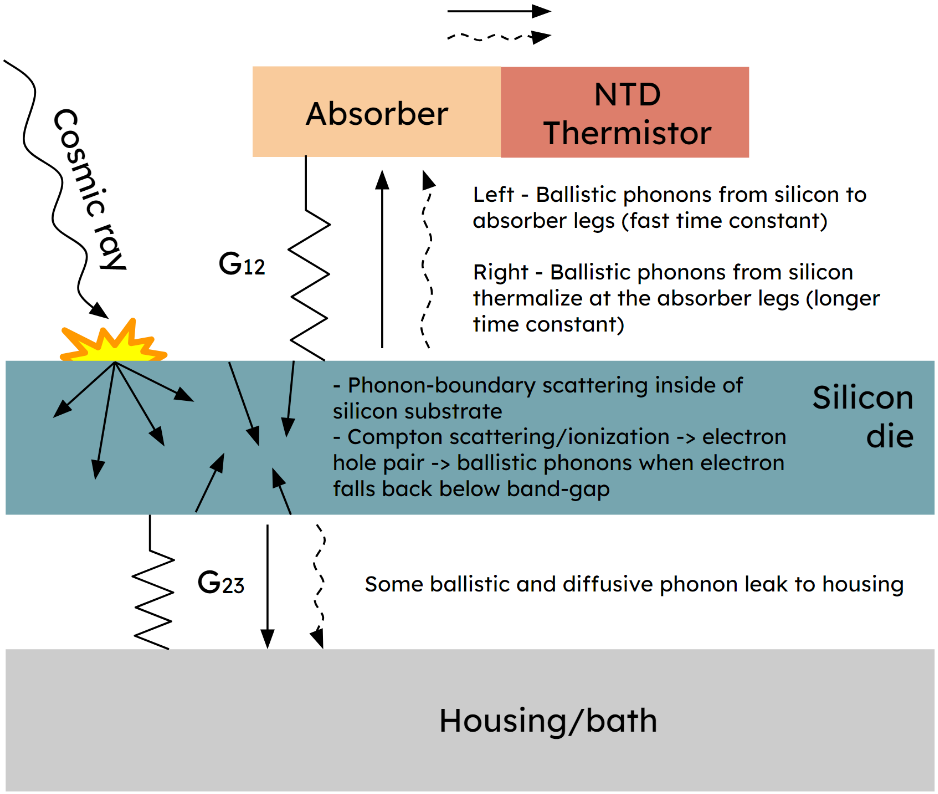

Figure 7.2: Block diagram of a Planck HFI detector with phonon propagation paths and mechanisms outlined.

TES. This means that high-energy phonons above the niobium superconducting gap energy can create quasiparticles that will recombine to create heat signals throughout the wafer. For LiteBIRD, high-energy ballistic phonons with a large enough mean free path can create cross-wafer quasiparticles and thermal diffusion, observed by multiple detectors at once. The common-mode noise created by this type of coincidence signal, along with differential temperatures measured in orthogonal polarimeters, result in a cosmic ray contribution to the measured power spectrum. Simulations predicting the scale of this contribution have been performed at the level of one to 32 detectors [59], but more expansive simulations are required using more detectors and frequency bands to obtain an accurate estimate of the cosmic ray contribution.

### 7.3.2 Mitigation strategy

To mitigate the effects of ballistic phonon propagation in detector wafers, a normal metal can be used to downconvert ballistic phonons to energies below the superconducting gap energy [61]. When a high-energy phonon enters the normal metal layer, it will scatter off conduction electrons, reducing its energy. Reducing the density of ballistic phonons in the wafer will reduce the generation of quasiparticles and the resultant diffusive signal seen by the detectors. Along with reducing quasiparticle generation, phonon downconversion will also reduce ballistic phonon transfer between the silicon substrate and detectors, as seen in Planck's suspended membrane detectors. To reduce the thermal diffusion signal seen in the tails of the long glitch types, diffusive phonons in the silicon and the film layers of the detector wafer must be reduced. This can be accomplished by increasing the thermal conductance between the detector wafer and the invar frame, increasing the heat flow out of the detector wafer.

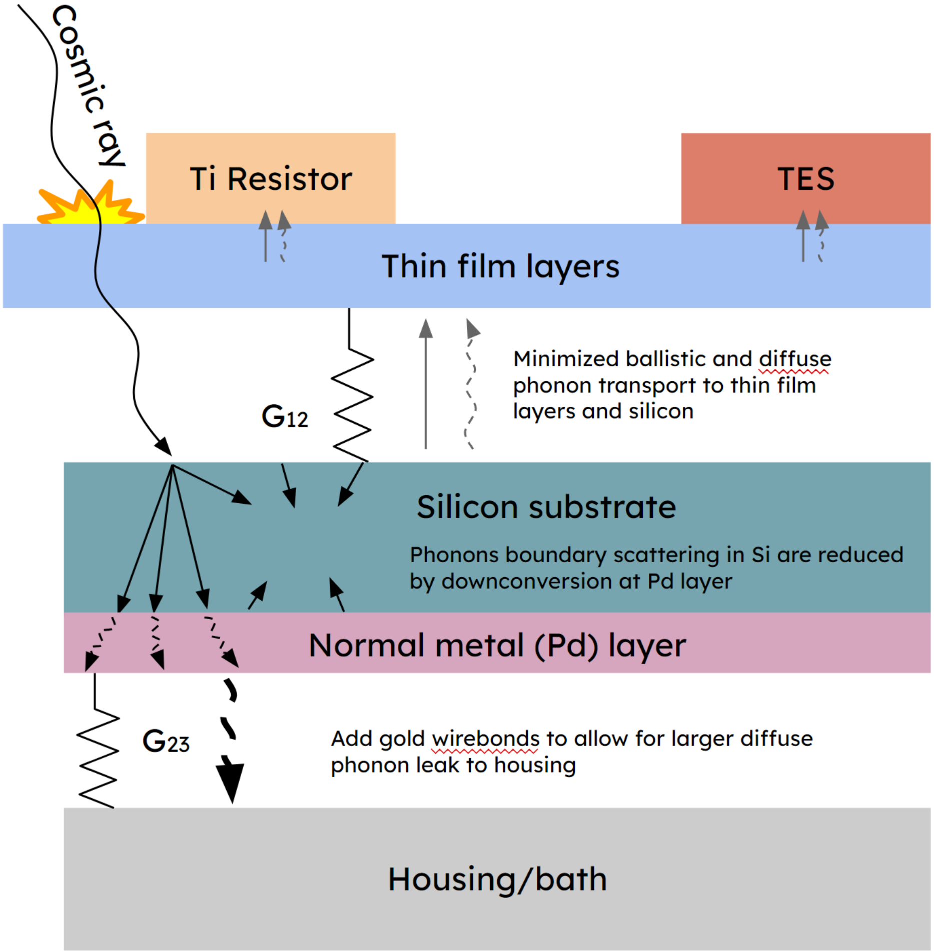

Figure 7.3: Block diagram of a LiteBIRD detector with phonon propagation paths and mechanisms outlined.

**Direct hits on the detector**

Direct hits in either the TES or the absorber will result in short glitch modes that unfortunately cannot be mitigated. However, fortunately, the total surface area of a LiteBIRD TES plus its absorber is 1424 $\mu m^2$, which is $\sim$100 times smaller than a Planck spiderweb bolometer. This means that the theoretical short glitch rate should be reduced by a factor of 100 as well, assuming that phonons generated by direct hits on the transmission and bias lines can be downcoverted with the use of a normal metal layer. In a worst-case scenario, where Planck would see 360 events per hour on the absorber and eight events per hour on the thermistor, based on the ratio of exposed surface area alone, at L2 LiteBIRD would be expected to see a maximum of $\sim$4 short glitch events per hour due to direct hits. With this in mind, an effective long glitch type mitigation is important for LiteBIRD.

### 7.3.3 Usage of palladium and simulation work

A high heat capacity at cryogenic temperatures [62] makes palladium an excellent candidate normal metal for cosmic ray mitigation in LiteBIRD, as a higher heat capacity provides a larger thermal bath for deposited cosmic ray energy to dissipate into, resulting in a smaller change in temperature at the detector for a given energy deposition. Currently, mitigation strategies are still being tested, but the use of a palladium layer on the backside of the detector wafer has been determined to be the best current strategy, as discussed in the following section. Additional palladium on the topside of the detector wafer is also being fabricated, penetrating through the wafer's thin-film layers and ground plane, making contact with the silicon substrate. Physical contact of the thin-film layers with the palladium will result in downconversion not only of ballistic phonons traveling through the silicon, but will allow for downconversion of quasiparticles in the superconducting groundplane, as well as a heat path to channel diffusive phonons in the thin-film layers away from the detectors. The current design that has yet to be tested includes gold wire bonds from these topside palladium layers to the backshort that is mounted above the device wafer, allowing for an efficient heat path away from the detectors. Gold wire bonds will similarly be used in the X-ray Integral Field Unit on the Athena mission to lower the thermal diffusion time constant from the silicon substrate to the experiment's TES detectors [63].

Samantha Stever at Okayama University has been simulating the effect of a normal metal layer on the back side of a detector chip, along with gold wire bonds on the back side of that chip (see Figure 7.4. The results indicate that an added gold layer will decrease the initial glitch amplitude seen at the TES, but will increase the intermediate tail amplitude. This is likely attributed to an increase in the effective heat capacity of the bath, increasing the thermal diffusion time constant from the bath to the detector ($\tau_{bath \to detector} = C_{bath}/G_{bath \to detector}$, where $G_{bath \to detector}$ does not change. The addition of gold wire bonds sees the diffusion tail fall to zero much faster than without, as the thermal conductance from the bath to the holder is increased.

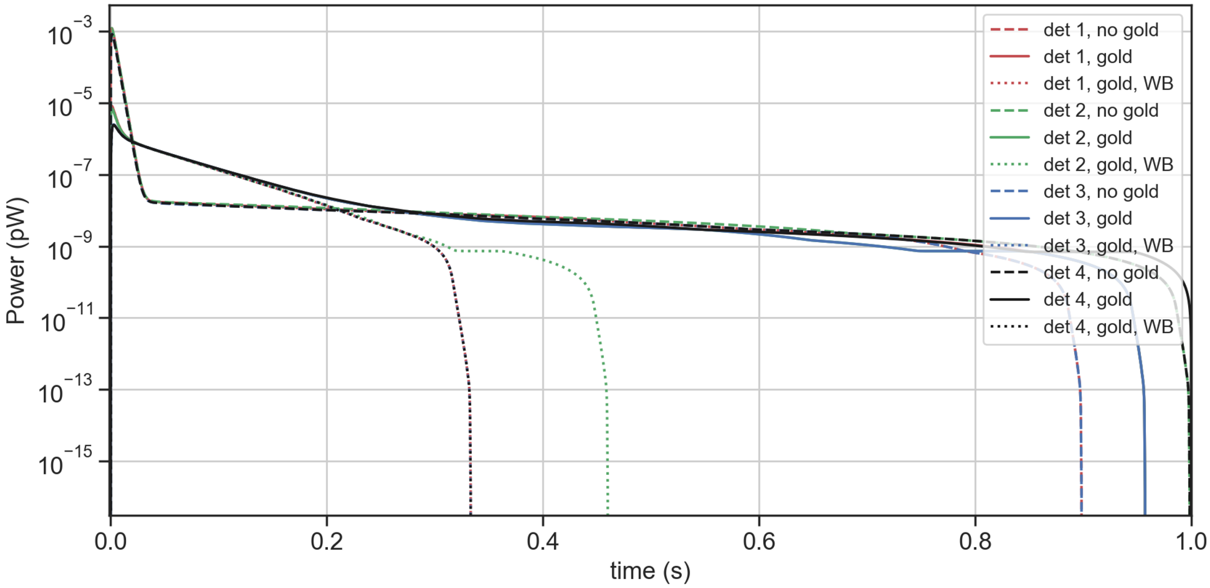

Figure 7.4: Simulated power seen at a bolometer via A 500 keV energy deposition in a silicon wafer with and without a 10 $\mu m$ gold layer and gold wirebonds. The energy here is deposited underneath detector 1. Other detectors are places throughout the chip. Focusing on detector 4 (black lines), features can be seen more clearly. These being the decreased amplitude but increased time constant in a gold only chip, as well as the fast drop off in the tail due to normal layer layers at ∼0.35 s, as opposed to without at 1.0 s. Credit: Samantha Stever

## 7.4 Mitigation testing at Berkeley

Using prototype mitigated chips fabricated at the Marvell Nanofabrication Laboratory, mitigation testing has been performed in both the 576 test dewar at 300 mK, as well as in a Bluefors LD-400 dilution refrigerator (DR). The tests have used a cryogenic Americium-241 source in 576, and an external Cobalt-60 source and background muons in the DR. Although testing is still underway, these initial tests indicate a direction for mitigation fabrication and simulation, and provide insight for moving to more comprehensive full-wafer testing in the future.

### 7.4.1 Glitch finding software

In order to analyze data from source and muon testing, a finding and fitting software package was developed to produce energy histograms and output coincidence information. A matched filter peak finder is used to convolve a template function with mean and tilt subtracted, 5 kHz sampled timestreams in order to isolate glitch events in the detectors, where

$$P(t) = \frac{1}{(1 + e^{-a(t-b)})}, \tag{7.1}$$

is the template function for the rising edge of a glitch, and

$$P(t) = 1 - e^{-ct}, \tag{7.2}$$

is the template function for the exponential decay in the tail, noting that both templates are applied to mean and tilt subtracted timestreams. A threshold energy is applied to this finder as well to exclude potential noise fluctuations from the event list.

Once the events are found, they are windowed. The lower limit of the window is found by averaging before the maximum amplitude value, and the upper limit is found by matching averaged values in the tail to the initial RMS noise value, ensuring that the full event decay is captured. Using this, measured energy values can be found either by integrating over the mean RMS noise-subtracted pulse window or by fitting each pulse and integrating over the fit function. Determining glitch energy absorption using a fit function excludes possible contamination due to noise fluctuations in low-energy events, however, can be inaccurate in some cases where the fit parameters do not perfectly define the decay characteristics of the tail.

The raw output from the DC SQUID controller measuring the current through a TES during electrothermal feedback can be converted to power units using the equation:

$$P = \epsilon_{SQ} V_{SQ} V_{bias}, \tag{7.3}$$

where $V_{SQ}$ is the raw output voltage from the SQ controller, and $\epsilon_{SQ}$ is the conversion factor for the SQUID controller output in A/V. $\epsilon_{SQ}$ is a value found using a calibration resistor in place of a TES.

To fit each individual pulse, a fit for each windowed event is found using a second-degree polynomial in log space, shown in Figure 7.5. This method tends to work well for the majority events; however, it is prone to error at very low and very high energies.

### 7.4.2 Americium-241 testing

Americium-241 is an isotope of americium that emits primarily 5.5 MeV alpha particles, as well as 50 keV gamma rays. Often used in smoke detectors, Am-241 was used for cosmic ray testing as a means of depositing large amounts of energy into a test chip at a high rate. Because Am-241 is an alpha source, it must be used inside a cryostat for TES testing, as alpha particles lack substantial penetration power. To be able to use an Am-241 source safely in a cryostat, extensive tests were performed to ensure that the source in question would not leak during cooling due to differential thermal expansion of the epoxy that seals the americium into its steel capsule. In this case, a smoke detector source was used and

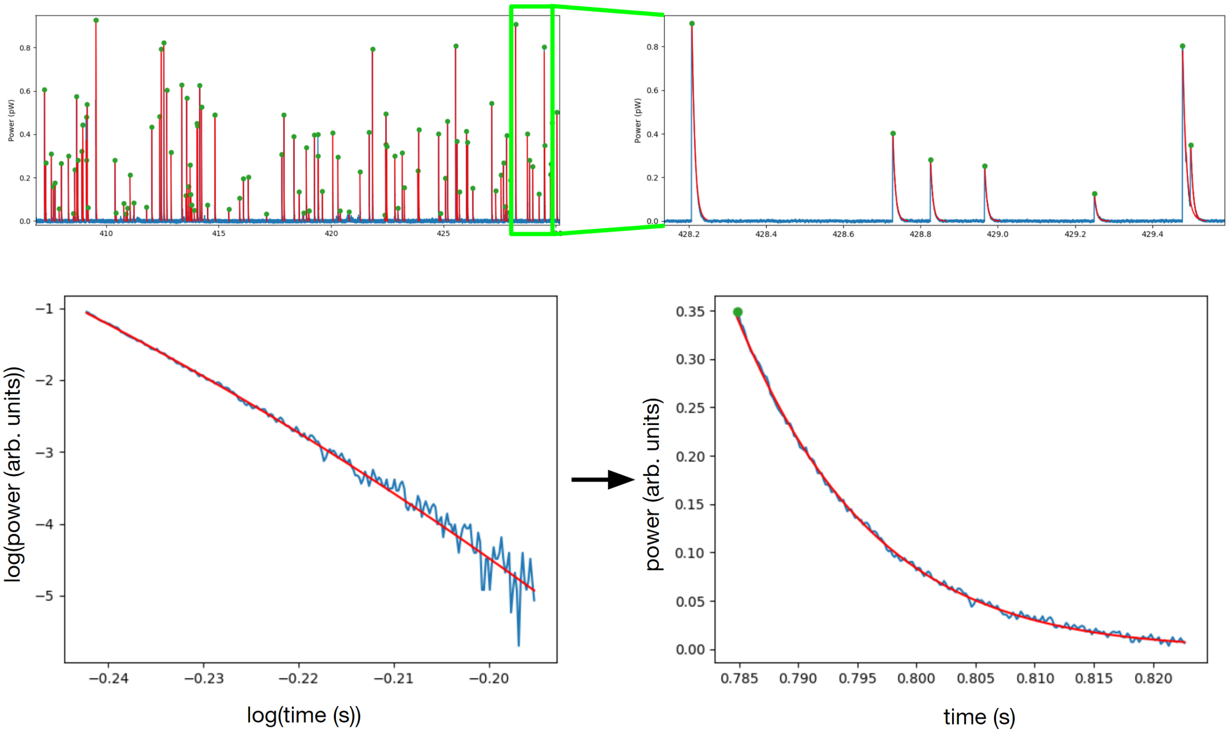

Figure 7.5: Fits from a TES timestream exposed to an Am-241 alpha source. (Top) example of peak finding and fitting a mean subtracted TES timestream. (Bottom) example of a glitch fit in log space.

liquid nitrogen dunk tests were performed followed by liquid scintillation tests of swabs from potentially contaminated surfaces. A special invar holder was designed to house both the test chip and position the Am-241 source in three dimensions (seen in Figure 7.6). An additional collimation piece was designed and drilled using a 100 $\mu m$ diameter micro drill bit with the intention of isolating where the alpha particle impacts would occur on the detector chip. Unfortunately, with the cryogenically tested source, the event rate using the collimator was too low to achieve adequate statistics and was not used.

One important thing to note is that because the large energy deposition from the alpha particle being stopped in the chip, the resulting rapid change in current $dI/dt$ caused by an event occurring while the TES is in transition resulted in the DC SQUIDS 'jumping flux'. This means that the SQUID would move into its next flux quanta, causing a step in the data that contaminated glitch events. Because of this, for Am-241 testing, the TES were overbiased, held slightly above their transition points. Because the electrothermal feedback loop outside of the transition no longer satisfies $P = P_{opt} + P_{elec}$, the bolometer will act non-linearly, and the resultant energy histograms of in a data set are no longer calibrated. Though calibrated values for deposited energies could not be recorded, glitches could still be measured, and energy histograms could be compared with simulated results.

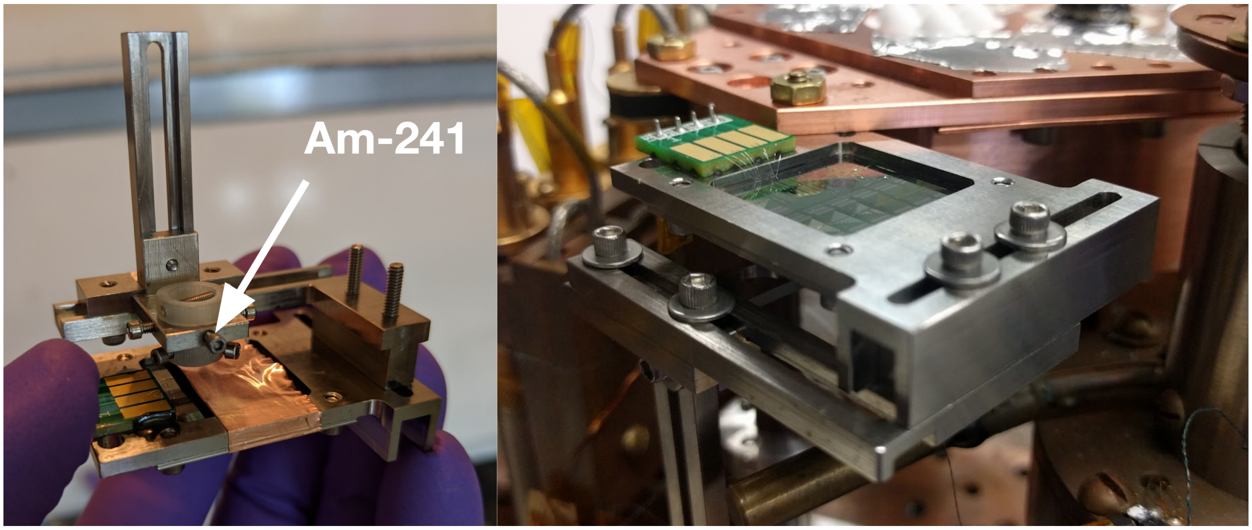

Figure 7.6: Invar detector chip and Am-241 holder designed to be mounted in the 576 cryostat.

With the Am-241 source placed directly over a TES test chip, an event rate of 3.2 Hz was measured when illuminating the detector side of the chip, and 0.1 Hz when illuminating the backside of the chip. The only events that remained in the backside illumination test were the lowest-energy events, indicating that the 60 keV gamma events were likely being measured. This also indicates that the alpha particles stopped fully in the top, thin-film layers of the chips, causing ballistic phonon and quasiparticle propagation through the silicon nitride and niobium ground-plane layers, respectively.

An interesting result came when comparing a control bolometer (no mitigation) with a simulation from Yuto Minami. This simulation (shown in Figure 7.8) models Am-241 events with a source illuminating an area close to a TES on silicon, also modeling the thin film layers on the chip. Front side and back side simulations were performed and distinct peaks for the gamma ray penetration, the alpha stopping in the niobium ground plane, and thin film penetration (alpha stopping at silicon) were observed. Qualitatively, experimental data shows a few differences. These differences are a population of high-energy events, a slight hump in the thin-film penetration distribution, and mismatched amplitudes of features compared with the simulation results. The high-energy population is hypothesized to be from direct hits to the TES or absorber; however, the thin film hump is not well explained. This feature as well as the mismatched amplitudes could potentially be explained by the nonlinearities in the detector due to suboptimal biasing.

These results and comparison with simulation indicate that in a TES, phonons propagate through thin film layers and can be seen at the TES, and that the effect from quasiparticles generated in the superconducting niobium groundplane can also be seen.

One additional notable result was found when placing the source directly in-between two detectors spaced closely together, and covering one detector with copper tape, shield-

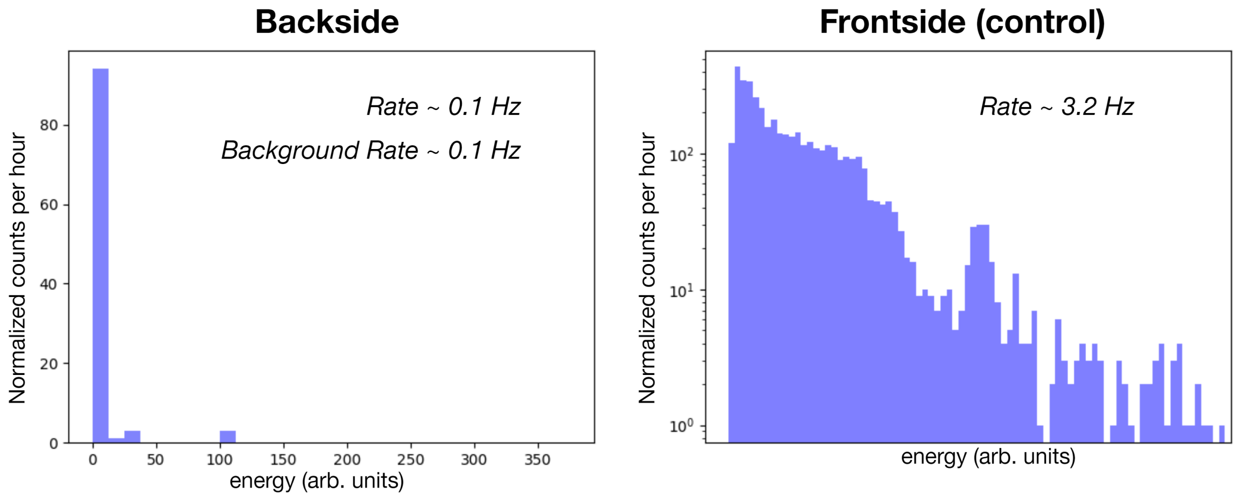

Figure 7.7: Binned pulse energies from fit in Am-241 testing, comparing front side vs. back side chip illumination, using a control bolometer (no mitigation).

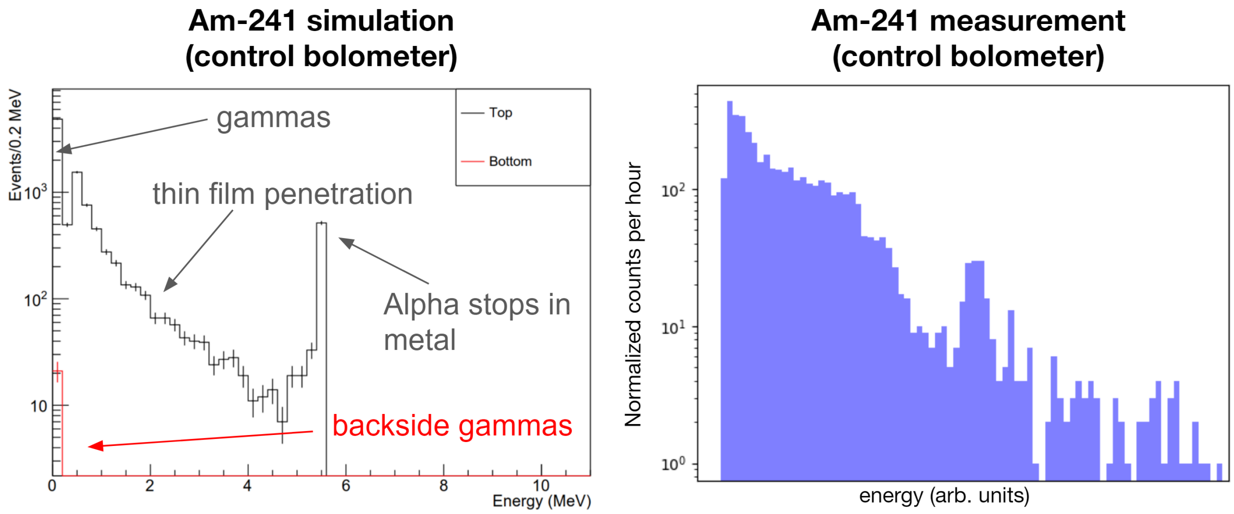

Figure 7.8: (Left) simulation results from Yuto Minami showing an energy spectrum from a test chip illuminated with an Am-241, and data from a matching test with similar features (right).

ing it from the alpha particles. A suppression in the thin-film feature and the ground-plane stopping feature was observed in the energy spectrum, as well as a suppression in the highest-energy events. As a result, the overall event rate was lower by around an order of magnitude in the covered detector. This test indicated that a large fraction of the observed events occurred near the bolometer. Quantitatively, the covered bolometer saw only events occurring

$> 1$ mm from the TES and absorber, meaning that 90% of the observed events occurred within 1 mm of the TES and absorber.

Am-241 tests were also performed using bolometers with various mitigations. The most promising results came from a mitigation using palladium on the silicon nitride thin-film layer, braking the niobium ground plane and silicon oxide layers that are typically on top of the nitride, shown in Figure 7.9.

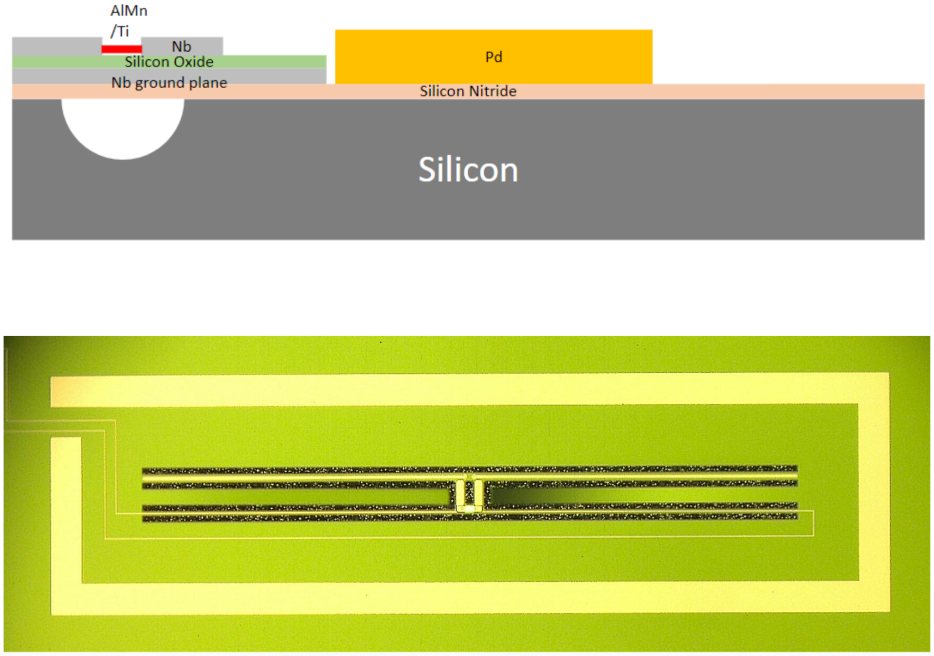

Figure 7.9: (Top) Block diagram of the tested TES palladium mitigation from Aritoki Suzuki, and an image of the fabricated TES with mitigation (bottom).

In this test, a suppression of events in the lower energy, thin-film penetration portion of the energy spectrum was observed. This suppression is evidence for the palladium downconverting ballistic phonons, as well as for thermal diffusion mitigation by creating a gap in the thin film layers. With this gap, phonons from events outside of the mitigation boundary would not be able to reach the TES. Note that the mitigation surrounding the bolometer begins only ∼0.4 mm away from the TES and absorber. As such, a large fraction of events will occur within the mitigation and will remain unaffected. However, the events that do occur outside of mitigation appear to be affected. Because the thin film portion of the spectrum is suppressed, it is reasonable to assume that downconverted phonons through the palladium are not easily thermally diffused through the silicon to the TES, rather, are allowed to escape due to high thermal conduction from the silicon to the invar holder.

The lack of suppression in the high-energy peak indicates that nearly all events in which an alpha stops in the niobium groundplane are seen within the mitigation, or within ∼0.4

mm of the TES or absorber. This indicates that quasiparticle generation in the groundplane acts on a relatively short distance scale and thermally diffuses into the thin film layers at distances <∼0.4 mm.

Though these results provide good agreement with expectations for how a normal metal layer will affect phonon transport, they only probe energy deposition into a chip's surface, and not through the chip's bulk. Because of this, further testing using high-energy gamma sources and background muons was performed in the Bluefors DR.

### 7.4.3 Testing in the Bluefors LD-400 DR

In 2020, cosmic ray testing transitioned from the 576 test dewar to the Bluefors DR. This was done for two reasons: First, the DR requires less work and resources to keep cold for longer compared to a wet dewar. This means that low-statistics background testing is more feasible over long periods of time. The next reason is to be able to test more sensitive, next generation detectors with lower $T_c$s at a 100 mK base temperature vs. 576's 300 mK base temperature. At a lower temperature, with the same bolometer geometry, a lower $P_{sat}$ can be achieved. This is because the thermal conductance in the bolometer will have an exponential dependence on temperature [37], so during electrothermal feedback at $T_{bolo} = T_c$

$$P_{opt} + P_{elec} = \int_{T_{base}}^{T_c} G(T)dT, \tag{7.4}$$

a lower $T_c$ can be used to achieve a lower $P_{sat}$ with the same $\Delta T = T_c - T_{base}$.

The majority of the 100 mK tests have been performed using 6 mm by 6 mm test chips that are simply blank silicon dies, with one TES bolometer at each edge of the chip (four in total), and $T_c$s around 170 mK. These chips are held in a gold-plated copper holder, clamped at each of the corners, with each corner making $0.125mm^2$ of contact at each corner. The contact area was minimized for these holders in order to achieve a lower thermal conductance between the silicon and the copper holder, extending thermal diffusion tails and allowing for testing of new thermal diffusion minimization techniques.

### 7.4.4 Cobalt-60 testing

In order to deposit energy through the entire depth of a silicon chip rather than just the surface, a source with radiation capable of penetrating the silicon is required. A Cobalt-60 source was acquired for this purpose. Co-60 emits primarily gamma rays at 1.17 and 1.33 MeV. To penetrate the silicon chips, the gamma rays must first penetrate the shells of the cryostat made out of aluminum and copper. For ∼1-1.5 MeV gammas, Compton scattering is the dominant means of energy deposition [64], and with the scattering cross sections for aluminum and copper, estimates can be made for energy deposition in each of the shells and silicon. The energy deposited in each layer can be estimated using

$$E = E_0 e^{-x\rho\frac{\mu}{\rho}}, \tag{7.5}$$

and the deposited energy is

$$E_0 - E = E_0(1 - e^{-x\rho\frac{\mu}{\rho}}), \tag{7.6}$$

where $\mu/\rho$ is the x-ray mass attenuation coefficient given for a given energy in a given material, $\rho$ is the density of the material x is the material thickness, E is the final energy of the exiting photon and $E_0$ is the incident energy of the photons.

Using approximate cryostat shell thicknesses at a silicon thickness of 675 $\mu m$, the energy deposited in each layer can be calculated, with $E_0^{shell_{n-1}} = E^{shell_n}$ starting with $E_0 = 1.25$ MeV. The resulting estimated energy deposited in the silicon substrate is ≈10 keV. These are rough calculations, but should give a ballpark estimate for how much total energy is absorbed by the silicon in a given event.

For the test setup, two identical chips in two identical copper holders were tested, one control chip and one chip with 2 $\mu m$ of palladium deposited on the back. Each chip was clamped in place with the same torque spec on all clamping screws. Measurements were taken to ensure that on the outside of the cyrostat, the Co-60 source was placed exactly in-between both chips on the inside of the cryostat. On each chip, two bolometers were tested in mirrored configurations, each separated by ∼5 mm on a given chip.

The resulting energy spectra of this test are shown in Figure 7.10. Normalized in counts per hour, it is evident that lower energy events ∼1 keV are suppressed in the mitigated chip, as well as higher energy events from ∼1.5 - 10 keV. The range of energies at the bolometers shows a cutoff ∼9.5 keV, which supports the ballpark estimate of around 10 keV of deposited energy. A suppression throughout the energy spectrum is consistent with simulation results that predict lower amplitudes and thermal diffusion time constants as a result of ballistic phonon downconversion at the normal metal layers. Relative to the total event count, the coincidence events in the mitigated chip did not change. This is likely because even though phonons were downconverted at the palladium layer, there were still many that were not affected by the mitigation and hence were still able to ballistically travel in the chip, affecting multiple detectors at once. In these tests, the palladium is deposited only on the back side of the chips, only downconverting phonons that otherwise would have boundary scattered off of the uncoated silicon surface. Because ballistic phonon creation occurs in $4\pi$ steradians at each point the incident gamma ray deposits energy through the entire length of the chip, roughly half of generated phonons will be directed towards the mitigation and half will be directed towards the thin-film layers and detectors. With a palladium mitigation on both sides of the chip and around the bolometer, a trap is created between the thin film layers and the bolometer. This configuration would have the potential for substantially more downconversion to occur, reducing the event count and absorbed energies further, along with coincidence rates.

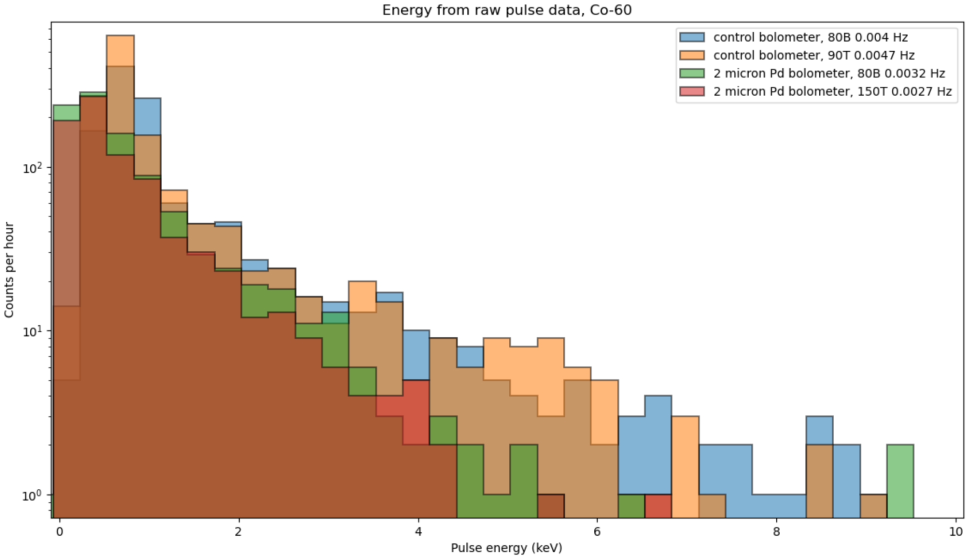

Figure 7.10: Energy spectra of four different detectors exposed to Co-60 gamma rays. Orange and blue detectors are control detectors, while red and green detectors have $2\mu m$ of palladium deposited on the backside of their chips.

Although Planck did measure slow glitch events and long glitch events with absorbed energies ranging from 1 - 10 keV, the majority of long glitch events occurred above 10 keV [57]. Although the Co-60 tests proved to be illuminating, ultimately higher energy absorption tests are needed to produce events that match more closely with what the detectors will see at L2.

### 7.4.5 Muon testing

The simplest way to see higher energy depositions in our sample chips is the muon background. At sea level, the background muon rate is ≈1 muon per square centimeter per minute. The chips were mounted vertically for all muon tests so far, and as a result we can expect ≈2 muons per hour. Of course, incident muons are not only deposited normal on the tops of the chips. Using compiled data in the article "High-energy cosmic ray muons in the Earth's atmosphere" by Kochanov et al. [65], as few as one muon every two days can be expected at angles ∼30 degrees off normal from the chip's face, and as few as three muons every two days at angles ∼75 degrees off normal. Taking into account that the majority of muons will come at near vertical angles, two per hour is a reasonable upper estimate for the number of muons entering the chip. Two events per hour means that to gather significant statistics to be able to resolve features in an energy histogram, data needs to be taken for up to a week. The minimum ionization energy in silicon from a muon ($dE/dx|_{min} = 1.664\ MeV g^{-1} cm^2$

[66]), which, depending on the orientation of the chip relative to the incident muon, can result in energy depositions in the silicon ranging from 260 keV to 2.3 MeV.

Data from muon tests in the 6 mm chips reveals slightly confusing results. The background muon rate in the control samples was 2.5 events per hour, roughly in agreement with the estimate of 2 events per hour. However, the rate in the palladium samples was 35 times lower than this, much higher than the decrease in the gamma ray tests of $\sim$50% in the palladium sample. Given that the four measured detectors were the same detectors as in the gamma tests, biased at the same bias voltage, the reason for the discrepancy is not obvious. Most likely, something happened in-between cooldowns to change or damage the palladium-backed sample or its readout, causing the detectors or readout to not function properly. Unfortunately, an exact reason has not yet been determined, and a more nuanced explanation is required. That being said, mitigation testing is ongoing and the test is planned to be replicated to help determine the source of the issue.

# Bibliography

[1] Edwin Hubble. “A Relation between Distance and Radial Velocity among Extra-Galactic Nebulae”. In: *Proceedings of the National Academy of Sciences* 15 (1929), pp. 168–173.

[2] Alexander Friedmann. “Über die Krümmung des Raumes”. In: *Zeitschrift für Physik* 10 (1922), pp. 377–386.

[3] N. Aghanim et al. “Planck2018 results: VI. Cosmological parameters”. In: *Astronomy amp; Astrophysics* 641 (Sept. 2020), A6. ISSN: 1432-0746. DOI: `10.1051/0004-6361/201833910`. URL: `http://dx.doi.org/10.1051/0004-6361/201833910`.

[4] L. Pogosian et al. “Primordial Plasma Fluctuations. I. Magnetization of the Early Universe by Dark Aperiodic Fluctuations in the Past Myon and Prior Electron–Positron Annihilation Epoch”. In: 856 (2018), p. 158. DOI: `10.3847/1538-4357/aab3dd`.

[5] Sara Seager, Dimitar D. Sasselov, and Douglas Scott. “How Exactly Did the Universe Become Neutral?” In: *The Astrophysical Journal Supplement Series* 128.2 (June 2000), 407–430. ISSN: 1538-4365. DOI: `10.1086/313388`. URL: `http://dx.doi.org/10.1086/313388`.

[6] A. A. Penzias and R. W. Wilson. “A Measurement of Excess Antenna Temperature at 4080 Mc/s”. In: *Astrophysical Journal* 142 (1965), p. 419. DOI: `10.1086/148307`.

[7] D. J. Fixsen. “THE TEMPERATURE OF THE COSMIC MICROWAVE BACKGROUND”. In: *The Astrophysical Journal* 707.2 (Nov. 2009), 916–920. ISSN: 1538-4357. DOI: `10.1088/0004-637x/707/2/916`. URL: `http://dx.doi.org/10.1088/0004-637X/707/2/916`.

[8] G. F. Smoot et al. “Structure in the COBE differential microwave radiometer first-year maps”. In: 396 (1992), p. L1. DOI: `10.1086/186504`.

[9] R. Adam et al. “Planck2015 results: I. Overview of products and scientific results”. In: *Astronomy amp; Astrophysics* 594 (Sept. 2016), A1. ISSN: 1432-0746. DOI: `10.1051/0004-6361/201527101`. URL: `http://dx.doi.org/10.1051/0004-6361/201527101`.

[10] Wayne Hu and Martin White. “A CMB polarization primer”. In: *New Astronomy* 2.4 (Oct. 1997), 323–344. ISSN: 1384-1076. DOI: `10.1016/s1384-1076(97)00022-5`. URL: `http://dx.doi.org/10.1016/S1384-1076(97)00022-5`.

[11] Uros ˘ Seljak and Matias Zaldarriaga. "Signature of Gravity Waves in the Polarization of the Microwave Background". In: *Phys. Rev. Lett.* 78 (11 1997), pp. 2054–2057. DOI: `10.1103/PhysRevLett.78.2054`. URL: `https://link.aps.org/doi/10.1103/PhysRevLett.78.2054`.

[12] Planck Collaboration et al. "Planck 2018 results - I. Overview and the cosmological legacy of Planck". In: *AA* 641 (2020), A1. DOI: `10.1051/0004-6361/201833880`. URL: `https://doi.org/10.1051/0004-6361/201833880`.

[13] R. K. Sachs et al. "Republication of: Perturbations of a cosmological model and angular variations of the microwave background (By R.K. Sachs and A.M. Wolfe)". In: *General Relativity and Gravitation* 39.11 (2007), pp. 1929–1961. ISSN: 1572-9532. DOI: `10.1007/s10714-007-0448-9`. URL: `https://doi.org/10.1007/s10714-007-0448-9`.

[14] Wayne Hu, Naoshi Sugiyama, and Joseph Silk. "The physics of microwave background anisotropies". In: *Nature* 386.6620 (Mar. 1997), 37–43. ISSN: 1476-4687. DOI: `10.1038/386037a0`. URL: `http://dx.doi.org/10.1038/386037a0`.

[15] Joseph Silk. "Cosmic black body radiation and galaxy formation". In: *Astrophys. J.* 151 (1968), pp. 459–471. DOI: `10.1086/149449`.

[16] Daniela Paoletti et al. "Planck and BICEP/Keck Array 2018 constraints on primordial gravitational waves and perspectives for future $B$-mode polarization measurements". In: *Phys. Rev. D* 106 (8 2022), p. 083528. DOI: `10.1103/PhysRevD.106.083528`. URL: `https://link.aps.org/doi/10.1103/PhysRevD.106.083528`.

[17] A. Manzotti et al. "CMB Polarization B-mode Delensing with SPTpol and Herschel". In: *The Astrophysical Journal* 846.1 (2017), p. 45. DOI: `10.3847/1538-4357/aa82bb`. URL: `https://dx.doi.org/10.3847/1538-4357/aa82bb`.

[18] Kevork N. Abazajian et al. *CMB-S4 Science Book, First Edition.* 2016. arXiv: `1610.02743 [astro-ph.CO]`.

[19] Peter Ade et al. "The Simons Observatory: science goals and forecasts". In: *Journal of Cosmology and Astroparticle Physics* 2019.02 (Feb. 2019), 056–056. ISSN: 1475-7516. DOI: `10.1088/1475-7516/2019/02/056`. URL: `http://dx.doi.org/10.1088/1475-7516/2019/02/056`.

[20] Nicholas Galitzki et al. "The Simons Observatory: instrument overview". In: *Millimeter, Submillimeter, and Far-Infrared Detectors and Instrumentation for Astronomy IX.* Ed. by Jonas Zmuidzinas and Jian-Rong Gao. SPIE, July 2018. DOI: `10.1117/12.2312985`. URL: `http://dx.doi.org/10.1117/12.2312985`.

[21] J.M Lamarre et al. "The Planck High Frequency Instrument, a third generation CMB experiment, and a full sky submillimeter survey". In: *New Astronomy Reviews* 47.11–12 (Dec. 2003), 1017–1024. ISSN: 1387-6473. DOI: `10.1016/j.newar.2003.09.006`. URL: `http://dx.doi.org/10.1016/j.newar.2003.09.006`.

[22] M. Bersanelli et al. “Planckpre-launch status: Design and description of the Low Frequency Instrument”. In: *Astronomy and Astrophysics* 520 (Sept. 2010), A4. ISSN: 1432-0746. DOI: `10.1051/0004-6361/200912853`. URL: `http://dx.doi.org/10.1051/0004-6361/200912853`.

[23] E Allys et al. “Probing cosmic inflation with theLiteBIRDcosmic microwave background polarization survey”. In: *Progress of Theoretical and Experimental Physics* 2023.4 (Nov. 2022). ISSN: 2050-3911. DOI: `10.1093/ptep/ptac150`. URL: `http://dx.doi.org/10.1093/ptep/ptac150`.

[24] H. Sugai et al. “Updated Design of the CMB Polarization Experiment Satellite LiteBIRD”. In: *J Low Temp Phys* 199 (2020), pp. 1107–1117. DOI: `10.1007/s10909-019-02329-w`. URL: `https://doi.org/10.1007/s10909-019-02329-w`.

[25] Benjamin Westbrook et al. “Development of the low frequency telescope focal plane detector modules for LiteBIRD”. In: *Millimeter, Submillimeter, and Far-Infrared Detectors and Instrumentation for Astronomy XI*. Ed. by Jonas Zmuidzinas and Jian-Rong Gao. SPIE, Aug. 2022. DOI: `10.1117/12.2630574`. URL: `http://dx.doi.org/10.1117/12.2630574`.

[26] Ludovic Montier et al. “Overview of the medium and high frequency telescopes of the LiteBIRD space mission”. In: *Space Telescopes and Instrumentation 2020: Optical, Infrared, and Millimeter Wave*. Ed. by Makenzie Lystrup et al. SPIE, Dec. 2020. DOI: `10.1117/12.2562243`. URL: `http://dx.doi.org/10.1117/12.2562243`.

[27] Giampaolo Pisano et al. “Achromatic half-wave plate for submillimeter instruments in cosmic microwave background astronomy: experimental characterization”. In: *Appl. Opt.* 45.27 (2006), pp. 6982–6989. DOI: `10.1364/AO.45.006982`. URL: `https://opg.optica.org/ao/abstract.cfm?URI=ao-45-27-6982`.

[28] Charles A. Hill et al. “Design and development of an ambient-temperature continuously-rotating achromatic half-wave plate for CMB polarization modulation on the POLARBEAR-2 experiment”. In: *SPIE Proceedings*. Ed. by Wayne S. Holland and Jonas Zmuidzinas. SPIE, 2016. DOI: `10.1117/12.2232280`. URL: `https://doi.org/10.1117%2F12.2232280`.

[29] The Polarbear Collaboration: P. A. R. Ade et al. “A MEASUREMENT OF THE COSMIC MICROWAVE BACKGROUNDiB/i-MODE POLARIZATION POWER SPECTRUM AT SUB-DEGREE SCALES WITH POLARBEAR”. In: *The Astrophysical Journal* 794.2 (2014), p. 171. DOI: `10.1088/0004-637x/794/2/171`. URL: `https://doi.org/10.1088%2F0004-637x%2F794%2F2%2F171`.

[30] Satoru Takakura et al. “Performance of a continuously rotating half-wave plate on the POLARBEAR telescope”. In: *Journal of Cosmology and Astroparticle Physics* 2017.05 (2017), pp. 008–008. DOI: `10.1088/1475-7516/2017/05/008`. URL: `https://doi.org/10.1088%2F1475-7516%2F2017%2F05%2F008`.

[31] Hill C. A. “Sensitivity Simulations and Half-wave Plate Polarization Modulators for Cosmic Microwave Background Observatories”. PhD thesis. UC Berkeley, 2020.

[32] S. Adachi et al. “A Measurement of the CMB E-mode Angular Power Spectrum at Subdegree Scales from 670 Square Degrees of POLARBEAR Data”. In: *The Astrophysical Journal* 904.1 (2020), p. 65. DOI: `10.3847/1538-4357/abbacd`. URL: `https://dx.doi.org/10.3847/1538-4357/abbacd`.

[33] D. Rutledge and M. Muha. “Imaging antenna arrays”. In: *IEEE Transactions on Antennas and Propagation* 30.4 (1982), pp. 535–540. DOI: `10.1109/TAP.1982.1142856`.

[34] Jennifer M. Edwards et al. “Dual-Polarized Sinuous Antennas on Extended Hemispherical Silicon Lenses”. In: *IEEE Transactions on Antennas and Propagation* 60.9 (2012), pp. 4082–4091. DOI: `10.1109/TAP.2012.2207048`.

[35] Roger O’Brient. “A Log-Periodic Focal-Plane Architecture for Cosmic Microwave Background Polarimetry”. PhD thesis. UC Berkeley, 2010.

[36] Benjamin Westbrook et al. *Detector fabrication development for the LiteBIRD satellite mission.* 2021. arXiv: `2101.05306 [astro-ph.IM]`.

[37] K.D. Irwin and G.C. Hilton. “Transition-Edge Sensors”. In: *Cryogenic Particle Detection.* Ed. by Christian Enss. Berlin, Heidelberg: Springer Berlin Heidelberg, 2005, pp. 63–150. ISBN: 978-3-540-31478-3. DOI: `10.1007/10933596_3`. URL: `https://doi.org/10.1007/10933596_3`.

[38] S. Takamura and T. Kato. “Effect of low temperature irradiation on the mechanical strength of organic insulators for superconducting magnets”. In: *Cryogenics* 20.8 (1980), pp. 441–444. ISSN: 0011-2275. DOI: `https://doi.org/10.1016/0011-2275(80)90074-0`. URL: `https://www.sciencedirect.com/science/article/pii/0011227580900740`.

[39] Zigmund D. Kermish et al. “The POLARBEAR experiment”. In: *SPIE Proceedings.* Ed. by Wayne S. Holland. SPIE, 2012. DOI: `10.1117/12.926354`. URL: `https://doi.org/10.1117%2F12.926354`.

[40] Ariel Cukierman. “Multiscale multichroic focal planes for measurements of the cosmic microwave background”. PhD thesis. UC Berkeley, 2018.

[41] Andrew Nadolski et al. “Broadband anti-reflective coatings for cosmic microwave background experiments”. In: *Millimeter, Submillimeter, and Far-Infrared Detectors and Instrumentation for Astronomy IX.* Ed. by Jonas Zmuidzinas and Jian-Rong Gao. SPIE, 2018. DOI: `10.1117/12.2315674`. URL: `https://doi.org/10.1117%2F12.2315674`.

[42] Aritoki Suzuki. “Multichroic Bolometric Detector Architecture for Cosmic Microwave Background Polarimetry Experiments”. PhD thesis. UC Berkeley, 2013.

[43] Ngoc Tinh Nguyen, Ronan Sauleau, and Cecilio JosÉ Martinez Perez. “Very Broadband Extended Hemispherical Lenses: Role of Matching Layers for Bandwidth Enlargement”. In: *IEEE Transactions on Antennas and Propagation* 57.7 (2009), pp. 1907–1913. DOI: `10.1109/TAP.2009.2021884`.

[44] R. Datta et al. “Large-aperture wide-bandwidth antireflection-coated silicon lenses for millimeter wavelengths”. In: *Applied Optics* 52.36 (2013), p. 8747. DOI: `10.1364/ao.52.008747`. URL: `https://doi.org/10.1364%2Fao.52.008747`.

[45] Yuting W. Chen and Xi-Cheng Zhang. “Anti-reflection implementations for terahertz waves”. In: *Frontiers of Optoelectronics* 7.2 (2014), pp. 243–262. ISSN: 2095-2767. DOI: `10.1007/s12200-013-0377-z`. URL: `https://doi.org/10.1007/s12200-013-0377-z`.

[46] Brandon L. Good, Shaun Simmons, and Mark Mirotznik. “General optimization of tapered anti-reflective coatings”. In: *Opt. Express* 24.15 (2016), pp. 16618–16629. DOI: `10.1364/OE.24.016618`. URL: `https://opg.optica.org/oe/abstract.cfm?URI=oe-24-15-16618`.

[47] K. P. Coughlin et al. “Pushing the Limits of Broadband and High-Frequency Metamaterial Silicon Antireflection Coatings”. In: *Journal of Low Temperature Physics* 193.5-6 (2018), pp. 876–885. DOI: `10.1007/s10909-018-1955-7`. URL: `https://doi.org/10.1007%2Fs10909-018-1955-7`.

[48] Haruyuki Sakurai et al. “Terahertz broadband anti-reflection moth-eye structures fabricated by femtosecond laser processing”. In: *OSA Continuum* 2.9 (2019), pp. 2764–2772. DOI: `10.1364/OSAC.2.002764`. URL: `https://opg.optica.org/osac/abstract.cfm?URI=osac-2-9-2764`.

[49] Thomas Gascard et al. “Experimental characterization of a planar phase-engineered metamaterial lenslet for millimeter astronomy”. In: *Appl. Opt.* 62.11 (2023), pp. 2906–2916. DOI: `10.1364/AO.480933`. URL: `https://opg.optica.org/ao/abstract.cfm?URI=ao-62-11-2906`.

[50] Erin Quealy. “The Polarbear Cosmic Microwave Background Polarization Experiment and Anti-Reflection Coatings for Millimeter Wave Observations”. PhD thesis. UC Berkeley, 2012.

[51] J. A. Sobrin et al. “The Design and Integrated Performance of SPT-3G”. In: *The Astrophysical Journal Supplement Series* 258.2 (2022), p. 42. DOI: `10.3847/1538-4365/ac374f`. URL: `https://doi.org/10.3847%2F1538-4365%2Fac374f`.

[52] Oliver Jeong et al. “Broadband plasma spray anti-reflection coating technology for millimeter-wave astrophysics”. In: *Appl. Opt.* 62.6 (2023), pp. 1628–1634. DOI: `10.1364/AO.478048`. URL: `https://opg.optica.org/ao/abstract.cfm?URI=ao-62-6-1628`.

[53] Mark S Mirotznik et al. "Broadband antireflective properties of inverse motheye surfaces". In: *IEEE transactions on antennas and propagation* 58.9 (2010), pp. 2969–2980.

[54] Ji Seong Choi et al. "Optimization of Shapes and Sizes of Moth-Eye-Inspired Structures for the Enhancement of Their Antireflective Properties". In: *Polymers* 12.2 (2020), p. 296.

[55] Nicole Farias et al. "Simulated Performance of Laser-Machined Metamaterial Antireflection Coatings". In: *Journal of Low Temperature Physics* 209 (June 2022), pp. 1–10. DOI: `10.1007/s10909-022-02751-7`.

[56] Kun Li. PhD thesis. University of Cambridge, Dec. 2011.

[57] P. A. R. Ade et al. "Planck2013 results. I. Overview of products and scientific results". In: *Astronomy amp; Astrophysics* 571 (Oct. 2014), A1. ISSN: 1432-0746. DOI: `10.1051/0004-6361/201321529`. URL: `http://dx.doi.org/10.1051/0004-6361/201321529`.

[58] A. Catalano et al. "Impact of particles on thePlanckHFI detectors: Ground-based measurements and physical interpretation". In: *Astronomy amp; Astrophysics* 569 (Sept. 2014), A88. ISSN: 1432-0746. DOI: `10.1051/0004-6361/201423868`. URL: `http://dx.doi.org/10.1051/0004-6361/201423868`.

[59] S.L. Stever et al. "Simulations of systematic effects arising from cosmic rays in the LiteBIRD space telescope, and effects on the measurements of CMB B-modes". In: *Journal of Cosmology and Astroparticle Physics* 2021.09 (Sept. 2021), p. 013. ISSN: 1475-7516. DOI: `10.1088/1475-7516/2021/09/013`. URL: `http://dx.doi.org/10.1088/1475-7516/2021/09/013`.

[60] A. Catalano et al. "Characterization and Physical Explanation of Energetic Particles on Planck HFI Instrument". In: *Journal of Low Temperature Physics* 176.5–6 (Feb. 2014), 773–786. ISSN: 1573-7357. DOI: `10.1007/s10909-014-1116-6`. URL: `http://dx.doi.org/10.1007/s10909-014-1116-6`.

[61] V. Iaia et al. "Phonon downconversion to suppress correlated errors in superconducting qubits". In: *Nature Communications* 13.1 (Oct. 2022). ISSN: 2041-1723. DOI: `10.1038/s41467-022-33997-0`. URL: `http://dx.doi.org/10.1038/s41467-022-33997-0`.

[62] B.M. Boerstoel, J.J. Zwart, and J. Hansen. "The specific heat of palladium, platinum, gold and copper below 30 K". In: *Physica* 54.3 (1971), pp. 442–458. ISSN: 0031-8914. DOI: `https://doi.org/10.1016/0031-8914(71)90189-3`. URL: `https://www.sciencedirect.com/science/article/pii/0031891471901893`.

[63] Antoine Miniussi et al. "Thermal Impact of Cosmic Ray Interaction with an X-Ray Microcalorimeter Array". In: *Journal of Low Temperature Physics* 199 (Apr. 2020), pp. 45–55. DOI: `10.1007/s10909-020-02337-1`.

[64] Hans Bichsel and Heinrich Schindler. "The Interaction of Radiation with Matter". In: Sept. 2020, pp. 5–44. ISBN: 978-3-030-35317-9. DOI: `10.1007/978-3-030-35318-6_2`.

[65] A. Kochanov, T. Sinegovskaya, and S. Sinegovsky. “High-energy cosmic ray muons in the Earth’s atmosphere”. In: *Journal of Experimental and Theoretical Physics* 116 (Mar. 2013). DOI: `10.1134/S1063776113020143`.

[66] J. Beringer et al. “Review of Particle Physics”. In: *Phys. Rev. D* 86 (1 2012), p. 010001. DOI: `10.1103/PhysRevD.86.010001`. URL: `https://link.aps.org/doi/10.1103/PhysRevD.86.010001`.